University of California

Santa Barbara

Probing Nanoscale Carrier Transport for Renewable Energy Applications

A dissertation submitted in partial satisfaction

of the requirements for the degree

Doctor of Philosophy

in

Mechanical Engineering

by

Wenkai Ouyang

Committee in charge:

Professor Bolin Liao, Chair
Professor Susanne Stemmer
Professor Yangying Zhu
Professor Carl Meinhart

September 2023

The Dissertation of Wenkai Ouyang is approved.

Professor Susanne Stemmer

Professor Yangying Zhu

Professor Carl Meinhart

Professor Bolin Liao, Committee Chair

July 2023

Probing Nanoscale Carrier Transport for Renewable Energy Applications

by

Wenkai Ouyang

Acknowledgements

I would like to express my heartfelt gratitude to my advisor, Bolin Liao, for the invaluable guidance and support provided throughout the past five years of my PhD journey. Your mentorship, especially during my early days in the program when I was unsure of my path, has been instrumental in shaping my academic and personal growth. I am truly thankful for the numerous opportunities you have given me and the unwavering support you offered both academically and personally. Your encouragement and patience have been a constant source of motivation during my time in the lab. Your humble, curious, and optimistic nature has been a profound inspiration to me and will continue to have a lasting impact on my future endeavors. I sincerely express my deep appreciation to my esteemed committee members, whose invaluable contributions have been essential to my PhD. I am grateful to Susanne Stemmer for her invaluable mentorship and the generous provision of samples. Additionally, I would also like to express my gratitude to Yangying Zhu for her invaluable assistance in nanofabrications and to Carl Meinhart for his expert guidance in COMSOL simulations.

I'd also like to thank Professor Joseph Heremans from the Ohio State University for his generous help in establishing the customized steady-state thermal transport measurement systems. Your knowledge sharing and guidance during my visit to OSU were truly invaluable. The insightful discussions we had and your approach as a researcher have inspired me greatly. I learned a tremendous amount during those few months and felt warmly welcomed by you and your group members, Dung Vu, Brandi Wooten, and Minyue Zhu, who also enriched my learning experience.

My appreciation extends to my labmates, who have been a source of support and joy throughout this journey. I thank Usama Choudhry for helping me adjust to life in

the USA and a new environment, Shengying Yue for your assistance and the uplifting moments in the lab, and Taeyong Kim for setting an example of what it means to be a dedicated researcher. In addition, thanks to Yubi Chen for your invaluable help with computational work, and to Xiangying Zuo and Fanghao Zhang for your contributions in developing the entire measurement systems. I am also grateful for the collaborations and assistance received from Alexander Lygo, who provided precious samples, and Kuang-hua Chou, who helped me nanofabrication and became a dear friend. I appreciate the funding support from the Sony Faculty Innovation Award, Air Force Office of Scientific Research, U.S. Department of Energy (DOE), National Science Foundation (NSF) via the DMREF program, and UCSB MRL.

I am deeply thankful for the support and encouragement from my friends at UCSB and Columbus, who stood by me during these challenging years. The diverse environment and cultural backgrounds have left a profound mark on my life. To my family, especially my Mom, I owe a debt of gratitude for your unwavering support and belief in me. Your love and encouragement have been my anchor during the darkest times of my PhD journey.

Curriculum Vitæ

Wenkai Ouyang

Education

2023	Ph.D. in Mechanical Engineering (Expected), University of California, Santa Barbara, USA.
2018	B.E. in Materials Science and Engineering, Southern University of Science and Technology (SUSTech), Shenzhen, China.

Publications

Wenkai Ouyang, A. C. Lygo, Y. Chen, H. Zheng, D. Vu, B. L. Wooten, X. Liang, W. Yao, J. P. Heremans, S. Stemmer, B. Liao, *"Extraordinary Thermoelectric Properties of Topological Surface States in Quantum-Confined* Cd_3As_2 *Thin Films"*, (In preparation, 2023).

F. Zhang, L. Patra, Y. Chen, **Wenkai Ouyang**, P. Sarte, S. Adajian, X. Zuo, B. Liao, *"Suppressing Phonon-Magnon Scattering Increases Thermal Conductivity Significantly in Gadolinium"*, (In preparation, 2023).

Wenkai Ouyang, X. Zuo, B. Liao, *"Impact of Photoexcitation on Secondary Electron Emission: a Monte Carlo Study"*, J. Appl. Phys., 133, 064301 (2023). (Editor's Pick)

Wenkai Ouyang, Y. Li, B. Yurash, N. Schopp, A. V. Flick, V. Brus, T.-Q. Nguyen, B. Liao, *"Simultaneous Characterization of Thermal Transport and Photocarrier Dynamics in Organic Semiconductor"*, Appl. Phys. Lett.,117, 253302 (2020).

Fields of Study

Mechanical Engineering (Advisor: Bolin Liao)

Abstract

Probing Nanoscale Carrier Transport for Renewable Energy Applications

by

Wenkai Ouyang

The utilization of sustainable energy sources, such as solar energy and thermoelectric energy, has gained significant attention in addressing the global energy challenge. Despite their potential, the efficiency of the energy devices still requires improvement. A comprehensive understanding of the underlying mechanisms is essential for rationalizing efficient energy conversion systems. However, the conventional characterization techniques limited by their resolutions are insufficient for the mechanism study. To overcome this limitation, it is imperative to develop new characterization techniques to probe carrier and energy transport in the energy devices. This thesis employs theoretical and experimental approaches to investigate carrier and energy transport using three distinct novel techniques: a theoretical study of photo-carrier dynamics through Monte Carlo simulations in scanning ultrafast electron microscopy (SUEM), transient grating spectroscopy for simultaneous characterization of thermal transport and photocarrier dynamics in organic semicondutors, and customized cryogenic steady-state transport measurements to explore thermoelectric transport in topological materials.

Understanding the transport of photogenerated charge carriers in semiconductors is crucial for improving the performance of photovoltaics. While recent experimental studies using SUEM have demonstrated that the local change in the secondary electron emission induced by photoexcitation enables direct visualization of the photocarrier dynamics in

space and time, the origin of the corresponding image contrast still remains unclear. Here, we investigate the impact of photoexcitation on secondary electron emissions from semiconductors using a Monte Carlo simulation aided by time-dependent density functional theory. Particularly, we examine two photoinduced effects: the generation of photocarriers in the sample bulk and the surface photovoltage (SPV) effect. Using doped silicon as a model system and focusing on primary electron energies below 1 keV, we found that both the hot photocarrier effect immediately after photoexcitation and the SPV effect play dominant roles in changing the secondary electron yield (SEY), while the distribution of photocarriers in the bulk leads to a negligible change in SEY. Our work provides insights into electron–matter interaction under photo-illumination and paves the way toward a quantitative interpretation of the SUEM contrasts.

In addition, the thermal management as well as carrier dynamics are both keys to the operational efficiency and stability for energy devices. Experimental techniques that can simultaneously characterize both properties are still lacking. We manage to characterize thin films of the archetypal organic semiconductor regioregular poly(3-hexylthiophene) and its blends with the electron acceptor [6,6]-phenyl-C61-butyric acid methyl ester on glass substrate. While the thermal responses from the thin film and the substrate cannot be distinguished due to their similar thermal diffusivities, we show that the recombination dynamics of photocarriers in the organic semiconductor thin films occur on a similar timescale and can be separated from the thermal response. Our measurements indicate that the photocarrier dynamics are determined by multiple recombination processes and our extracted recombination rates are in good agreement with previous reports using other techniques. We further apply TG spectroscopy to characterize another conjugated polymer and a molecular fluorescent material to demonstrate its general applicability. Our study indicates the potential of transient grating spectroscopy to simultaneously

characterize thermal transport and photocarrier dynamics in organic optoelectronic devices.

In addition to semiconductors, topological semimetals have been shown to possess intriguing thermoelectric properties promising for energy harvesting and cooling applications. However, thermoelectric transport in heterostructures formed by topological and conventional materials remains less explored. Here, we systematically examine thermoelectric transport in a series of topological Dirac semimetal (Cd_3As_2)/ semiconductor(GaSb) heterostructures by employing a customized cryogenic steady-state transport measurement. Surprisingly, we found a significantly enhanced Seebeck coefficient at cryogenic temperatures when the Cd_3As_2 layer was thin. Combining angle-dependent quantum oscillation analysis, magneto-thermoelectric measurement, transport modeling and first-principles simulation, we reveal the contribution from multiple conducting channels in the heterostructure, including bulk and topological surface states. Our analysis showcases the rich transport physics in a topological Dirac semimetal/semiconductor heterostructure and suggests new routes to achieving unusual thermoelectric performance at cryogenic temperatures.

Contents

Chapter 1

Introduction

The increasing global energy demand has placed immense pressure on finite energy resources, necessitating a shift towards more sustainable and renewable energy solutions. The over-reliance on traditional fossil fuels results in energy shortages and unstable energy prices on a global scale. This further exacerbates the challenges we face in meeting global energy needs. Moreover, this heavy dependence on fossil fuels contributes to climate change and air pollution significantly, manifesting in extreme weather events and environmental crises. The urgency of transitioning to renewable energy solutions is underscored by the need to mitigate greenhouse gas emissions, which are primarily responsible for global warming and its associated consequences. Embracing sustainable energy technologies is a crucial step towards reducing carbon emissions and fostering a more environmentally responsible and stable future.

While addressing a variety of global energy challenges, the utilization of sustainable energy sources such as solar, wind, and thermoelectric energy, has garnered substantial attention. These energy devices are capable of transforming various forms of energy into

valuable electricity. Solar cells convert the sun's solar energy while wind turbines convert wind energy, and thermoelectric devices convert heat energy into usable electricity. Despite their immense potential, the efficiency of these energy devices are still lacking and require enhancement. For this reason a comprehensive understanding of the underlying mechanisms governing efficient energy conversion systems is indispensable. In order to address this problem, it becomes imperative to pioneer novel characterization techniques designed explicitly to probe carrier and energy transport within these energy devices. This thesis employs both theoretical and experimental approaches to explore the dynamics of carrier and energy transport.

Within this paper, we embark on a comprehensive exploration of three distinct, cutting-edge techniques. First, we delve into the theoretical realm, conducting an intricate study of photo-carrier dynamics in SUEM through the Monte Carlo simulations and TDDFT. Next, we develop an optical characterization technique, transient grating spectroscopy, which permits the simultaneous characterization of thermal transport and photocarrier dynamics on organic semiconductors. Lastly, we focus on cryogenic steady-state transport measurements, meticulously customized for the specific purpose of unraveling the thermoelectric transport in topological materials. Through these approaches, we aim to shed light on the intricacies of carrier and energy transport, ultimately contributing to the development of more efficient energy conversion systems for a sustainable future.

1.1 SUEM and Photocarrier Dynamics

There has been a concerted effort to explore and discover sustainable energy resources. Among the most promising of these resources is solar energy, and the utilization of solar energy has emerged as one of the most widely recognized renewable resources. Solar cells,

being the key technology behind solar energy, efficiently capture sunlight and convert it into usable electricity. However, to optimize the performance of solar cells, a profound insight of the charge carriers dynamics within these devices is indispensable.

Understanding photocarrier dynamics accurately is critical for improving the performance and ensuring the stability of high-efficiency photovoltaic (PV) cells, light-emitting diodes, and other optoelectronic devices. For example, the performance of PV cells critically depends on the minority carrier diffusion process [1, 2, 3], and efficient hot photocarrier collection provides a possible means to boost the PV efficiency above the Shockley-Queisser limit [4]. These processes can only be probed and better understood by experimental tools that can detect light-induced carrier behaviors with combined high spatial and temporal resolutions.

In order to study photocarrier dynamics behind the solar cells and opto-electronic devices, a characterization tool is needed that can achieve both high spatial and temporal resolution. Typically, the length scale of photocarrier dynamics is within the nanometer range. For example, the mean free path of electrons in silicon is approximately 10 nm [5, 6]. In general, electron microscopy can provide nanometer spatial resolution while its temporal resolution is limited due to a minimum time interval between consecutive images, which hinders its ability to capture fast dynamic processes. Carrier dynamics in solar cells occur over timescales spanning from femtoseconds to nanoseconds [7]. For example, the cooling time of photo carriers is approximately 100 fs [8]. While ultrafast optical spectroscopy can capture information within this timescale range [9], it encounters challenges in achieving nanometer spatial resolution due to the optical diffraction limit. The integration of these two techniques reveals the capability to achieve simultaneous spatial and temporal resolutions for studying photocarrier transport.

In recent studies, researchers combined the high-energy pulsed electron beam generated by illuminating a photocathode with a pulsed laser source [10], with electron microscopy to achieve a high temporal and spatial resolution simultaneously. These short electron pulses, with durations down to sub-picoseconds, can be accelerated to high energy, and thus, finely focused to sub-nanometer spatial resolution. Techniques based on the pulsed electron beam, such as ultrafast electron diffraction (UED) and ultrafast transmission electron microscopy (UTEM) have been used to visualize photocarrier dynamics with great success [11, 12, 13, 14]. In 2010, Zewail and coworkers invented scanning ultrafast electron microscopy (SUEM) by combining the temporal resolution of short electron pulses with the spatial resolution of scanning electron microscopy (SEM) [15, 16, 17]. Compared to UED and UTEM, SUEM excels in surface sensitivity and is particularly suitable to study surface photocarrier transport [18, 19, 20, 21], surface acoustic waves [22, 23] and surface defect-carrier interactions [24].

In SUEM, a femtosecond infrared laser source is split and converted into a pump beam (typically 515 nm) and an ultraviolet probe beam (typically 343 nm or 257 nm). Figure 1.1(a) depicts the working principle of SUEM. The pump pulse directly hits the sample surface and causes structural, electronic, or thermal changes, such as photocarrier excitation, surface photovoltages [25, 21], topographical distortions and temperature rise [26]. In the meantime, the ultraviolet probe beam is focused onto the electron gun inside an SEM column to generate short electron pulses, which are accelerated and focused onto the sample surface. The time delay between the optical pump pulses and electronic probe pulses is controlled by a mechanical delay stage. The probe electron pulses, or the "primary electrons" (PEs), excite secondary electrons (SEs) from the sample surface, which are collected by an Everhart-Thornley detector (ETD), and the number of SEs emitted from each location on the sample surface is used to form an image.

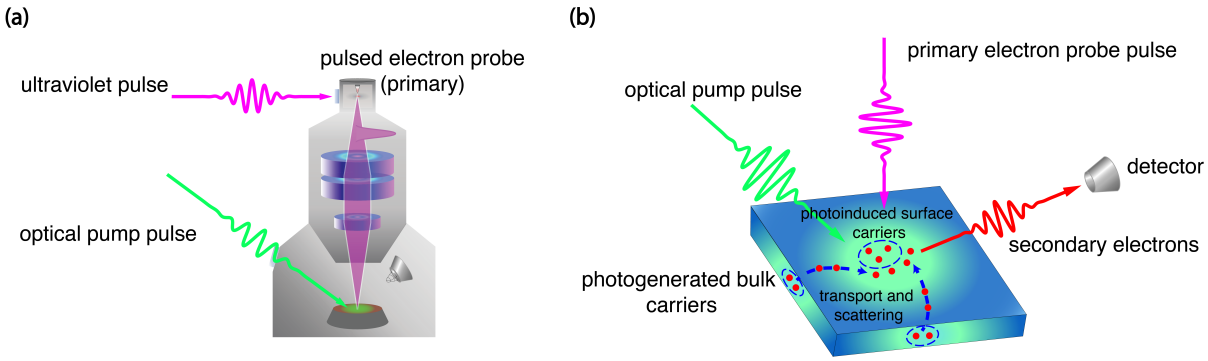

Figure 1.1: **Schematic of SUEM experiment and image formation.** (a) A schematic showing a typical setup of the SUEM instrumentation. The green line denotes the optical pump beam while the purple line denotes the optical beam to generate the probe electron pulses. The electron pulses travel down the SEM column and are focused onto the sample through the electron optics. (b) Image formation mechanism in an SUEM. The primary electrons excite secondary electrons from the sample, which are collected by an ETD. The optical pump pulse generates photocarriers in the bulk and near the surface, which modulate the secondary electron yield. The changes in the local secondary electron yield as a result of photoexcitation are used to form SUEM contrast images.

SUEM contrast images are then generated by comparing the change in the SE images as a result of photoexcitation. By controlling the time delay between the optical pump pulses and the electronic probe pulses, SUEM contrast images depicting the change of the sample at a given time after the photoexcitation can be recorded. For example, Najafi *et al.* observed the interfacial carrier dynamics at a silicon p-n junction with SUEM and reported ballistic carrier transport that cannot be explained by conventional drift-diffusion models [27]. Liao *et al.* measured the hot carrier transport in amorphous silicon using SUEM and observed the spatial separation of electrons and holes [19]. In these studies, the high spatial-temporal resolution of SUEM enables the investigation of photo-induced local microscopic physical processes on a wide range of materials. However, in order to quantitatively interpret these photophysical processes, it is critical to fully understand the underlying mechanisms for the SUEM image contrasts.

Researchers have made efforts to elucidate the mechanism behind image contrast. Najafi

et al. [27] proposed that image contrast arises from local changes in carrier concentrations induced by the optical pump pulse. Additionally, Li *et al.* [28] suggested that photo-illumination leads to surface band bending, resulting in the surface photovoltage (SPV) effect. The surface band bending alters the electron transmission probability, which in turn influences the secondary electron yield (SEY). However, these explanations remain qualitative, and there is a lack of quantitative study regarding the image mechanisms. In the Chapter 3, we apply Monte Carlo simulation aided by time-dependent density functional theory (TDDFT) to quantitatively study the SUEM image contrast.

1.2 TG for Photocarrier and Thermal Dynamics

Organic solar cells, being an alternative to their inorganic counterparts, offer a wide array of attractive features. These include their lightweight nature, low cost, utilization of earth-abundant elements, processability, and mechanical flexibility, which have garnered significant interest from both academic and industrial communities [29]. In particular, polymer-based bulk heterojunction organic photovoltaics (OPVs) stand out as promising alternatives, particularly in contrast to inorganic solar cells, which involve considerably higher fabrication costs. The heterojunctions are typically comprised of a blend of organic semiconductors: a conjugated polymer and a derivatized fullerene, acting as the donor and the acceptor, respectively. Ever since its invention, the bulk or mixed heterojunction has been widely used as the foundation for all efficient OPVs to overcome the short exciton diffusion lengths on the order of a few to ten nanometers in most organic semiconductors [30].

Till now, one of the most studied heterojunctions is a blend of regioregular poly(3-hexylthiophene) (P3HT) and the electron acceptor [6,6]-phenyl-C61-butyric acid methyl

ester (PCBM). The charge transport in this system has been widely studied to improve the device efficiency [31, 32, 33, 34]. Specifically, several experimental techniques have been developed to probe the photocarrier dynamics in semiconducting polymers, targeting different time windows after photoexcitation. For example, ultrafast optical spectroscopy [35, 36] typically examines the sub-nanosecond dynamics, where photogenerated excitons play a significant role. Time-resolved microwave conductivity (TRMC) measurements can resolve the dynamics of free charge carriers in longer time scales, from hundreds of nanoseconds to microseconds [31, 32]. Transport and recombination of dissociated free charge carriers (polarons) in these longer time scales directly influence OPV devices' performance. Also, device-level current–voltage (I–V) characterization [37] can provide indirect information about the photocarrier dynamics at the macroscopic scale.

In contrast to the photocarrier dynamics, a limited amount of work has been directed towards understanding the thermal properties. Feng *et al.* [38] measured density-dependent thermal diffusivities (0.5 $\text{mm}^2/\text{s} \sim 1$ mm^2/s) of P3HT thin film by a transient electro-thermal technique, and observed that the thermal conductivity increases with the density while the thermal diffusivity decreases. By engineering inter-molecular and intra-molecular interactions, Xu *et al.* [39] obtained a high thermal conductivity of 2.2 W/m-K for P3HT thin films deposited by organic chemical vapor deposition. Rojo *et al.* [40] measured the thermal conductivity of P3HT nanowires with a value of 2.29 W/m-K. P3HT in the form of nanofibers was found to share a similar thermal diffusivity with the thin films ($\sim 10^{-1}$ mm^2/s), but have a lower thermal conductivity because of the low-density structure [41]. An ultra-low thermal conductivity for PCBM (~ 0.03 W/m-K) was found by Duda *et al.* [42] using time domain thermoreflectance (TDTR) measurement, and a simple linear dependence of thermal conductivity on the blend ratio of P3HT: PCBM was observed.

The efficiency of OPVs is directly influenced by the charge transport properties in organic semiconductors. In addition, deficiencies in heat dissipation can lead to inefficiencies and instabilities in realistic devices [43]. The scarcity of work on these two types dynamics in the organic system urges research efforts on investigating dynamics from charge carriers and heat-conducting carriers simultaneously to promote energy-efficient applications [44]. Therefore, developing a characterization tool which can be used for studying the dynamics of the photogenerated charge carriers and heat carriers in semiconducting polymers is critical for improving the efficiency and performance of OPVs and optoelectronics [45].

Given the complexity of photocarrier dynamics in semiconducting polymers spanning wide space and time scales, it is desirable to have a time-resolved technique that can examine both transport and recombination of photocarriers with conveniently adjustable length scales. Moreover, as effective heat dissipation becomes increasingly important for device efficiency [46], simultaneous characterization of photocarrier dynamics and thermal transport properties of semiconducting polymers becomes an attractive feature. So far, several experimental techniques have been demonstrated to probe thermal conduction in organic materials, including time-domain thermoreflectance (TDTR) [47] and using suspended micro-devices [48]. Though these transient and steady-state methods have been employed for measurements of thermal properties in bulk and thin film materials [49], they are not capable of monitoring charge carrier dynamics. It is known that the properties of polymeric materials are subjected to variations due to processing and environmental conditions, further strengthening the demand to characterize both carrier dynamics and thermal transport in a single measurement.

Laser-induced transient grating (TG) spectroscopy is an optical technique successfully used in a wide range of applications [50], including quasiparticle dynamics, thermal transport, and mass diffusion. Recently, it has been demonstrated for studying heat transfer

in suspended polyethylene thin films [51]. This versatile pump–probe type method is based on two interfering pulsed laser beams derived from the same laser source, which create a spatially periodic excitation profile, resulting in a transient "grating" due to a rise of local photocarrier population and/or temperature after photogenerated carriers transfer energy to the lattice and cool down [50, 52, 53, 54]. The increased excited carrier population and temperature rise induce changes in the complex optical constants, which subsequently decay in time due to carrier/ thermal diffusion and carrier recombination, leading to time-dependent diffraction of a probe beam. Accordingly, it is sensitive to both carrier dynamics and thermal transport in the time domain from nanoseconds to microseconds over micrometer distances that can be conveniently adjusted by changing the grating period. In addition to this advantage, TG spectroscopy can conveniently separate the contributions from transport and local recombination and dissipation by continuously controlling the transport length scale set by the grating period.

In Chapter 4, we apply the TG technique to measure the grating decays in the model system regioregular poly(3-hexylthiophene) (P3HT) and its blend with the electron acceptor [6,6]-phenyl-C61- butyric acid methyl ester (PCBM). In our study, we examine neat P3HT films and associated blends containing PCBM with a weight ratio of 1.8 % and 50 %, hereafter, 1.8 % and 50 % blend, respectively. By varying the excitation grating period, we are able to resolve both the excited state and heat relaxation processes with the application of an appropriate model containing the two processes. It was found that the carrier dynamics are determined by multiple recombination mechanisms, while heat transfer was dominated by the response of the substrate. Our study suggests the TG technique can be a potentially versatile platform to characterize both photocarrier dynamics and thermal transport properties of semiconducting polymers.

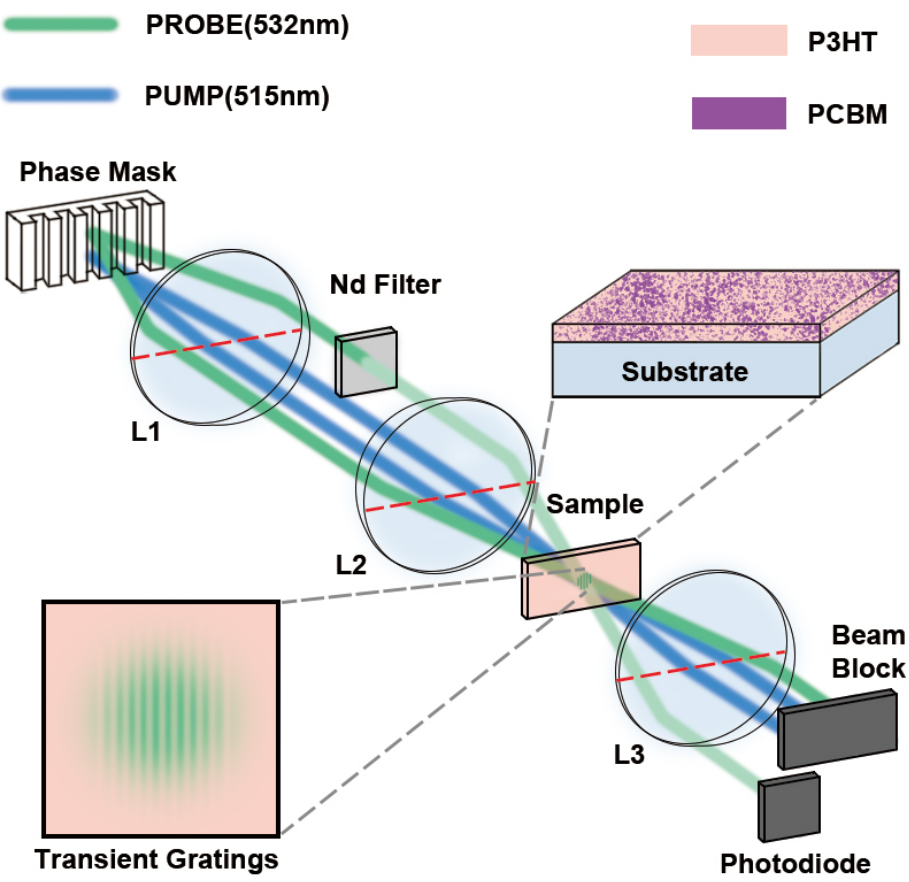

Figure 1.2: **Schematics of TG measurements of P3HT:PCBM thin films on glass substrates.** The phase mask splits the pump and probe beams. A pair of lenses (L1 and L2) collimate the beams and focus them onto the sample. The two pump beams generate grating pattern on sample surface, and the probe beams are used to detect the material response based on optical heterodyne detection, in which one beam is attenuated with a neutral density filter and the other is diffracted and directed back into a photodiode detector.

1.3 Thermoelectrics and Topological Materials

Apart from solar energy mentioned above, there exists another valuable yet underexplored resource in the form of waste heat. Various industrial processes and power generation plants produce substantial amounts of waste heat that often goes unused. This waste heat represents a significant opportunity to harness thermoelectric energy, where ther-

moelectric devices can convert heat directly into electricity, offering a promising avenue for sustainable energy generation. When a temperature gradient is applied to thermoelectric materials, the electrons and holes within the material diffuse from the hot end to the cold end. Consequently, the accumulation at the cold end, result in the generation of a voltage difference. The fundamental property that characterizes a material's ability to generate an electric voltage in response to a temperature gradient is known as the Seebeck coefficient. It is defined as the voltage increase per unit degree of temperature difference, where $S = -\frac{\Delta V}{\Delta T}$.

The efficiency of a thermoelectric (TE) device is determined by the non-dimensional figure of merit zT, expressed as $zT = S^2\sigma T/\kappa$. Here, σ denotes the electrical conductivity, T represents the absolute temperature, and κ is the thermal conductivity. Achieving a high ZT value is contingent on the presence of a thermoelectric material that encompasses both a high Seebeck coefficient and electrical conductivity, coupled with low thermal conductivity.

The topological insulator and Dirac semimetal Cd_3As_2 is a potential thermoelectric material due to its high electron mobility and low lattice thermal conductivity. The exotic bulk transport properties exhibited by these materials, such as the chiral anomaly and topologically protected surface states [55, 56], endow them with significant potential for electrical applications. Additionally, their unusual thermal and thermoelectric transport properties have also offered opportunities for potential thermoelectric energy conversion applications [57, 58]. For example, topological insulators and topological semimetals typically feature linear or close-to-linear electronic bands near the Fermi level, leading to a high charge carrier mobility [59] that is beneficial for thermoelectrics.

It has been experimentally shown that the thermoelectric performance of lead selenide

(PbSe) can be enhanced by a pressure-driven topological phase transition, where the formation of linear Dirac bands improves the electrical conductivity [60]. Furthermore, both theory [61] and experiments [62, 63] have established that the Seebeck coefficient of topological semimetals can increase with the magnetic field in the quantized regime without saturation. On the thermal transport side, first-principles simulations and inelastic neutron and x-ray scattering measurements have suggested significant phonon softening in topological semimetals due to the Kohn anomaly, leading to reduced thermal conductivity [64, 65, 66]. These properties are all promising features for improving thermoelectric energy conversion efficiency.

So far, however, the explored thermoelectric properties of topological insulators and semimetals are mostly limited to those in intrinsic bulk crystals, while epitaxial thin films remain less examined. Compared with bulk crystals, epitaxial thin films offer more degrees of control, such as strain and quantum confinement, which can be further tuned to optimize their thermoelectric properties. In addition, topological surface states also contribute more prominently in thin films.

In Chapter 5, we conduct an in-depth study of characterization of the thermoelectric properties of epitaxial thin films of the topological Dirac semimetal Cd_3As_2 with three different thicknesses. Our main focus is to investigate and quantify the influences of surface states and quantum confinement. The primary objective is to isolate and analyze the impacts of surface states and quantum confinement. To achieve this, we employ a steady-state transport measurement system, enabling us to precisely measure the electrical and thermoelectric properties of the thin films. Additionally, we carry out angle-dependent electrical and thermal transport measurements to differentiate between the bulk states and the topological surface states. Figure 1.3 illustrates the experimental setup, featuring a rotation sample stage. The comprehensive understanding of our experimental methods

can be refer to Chapter 2.

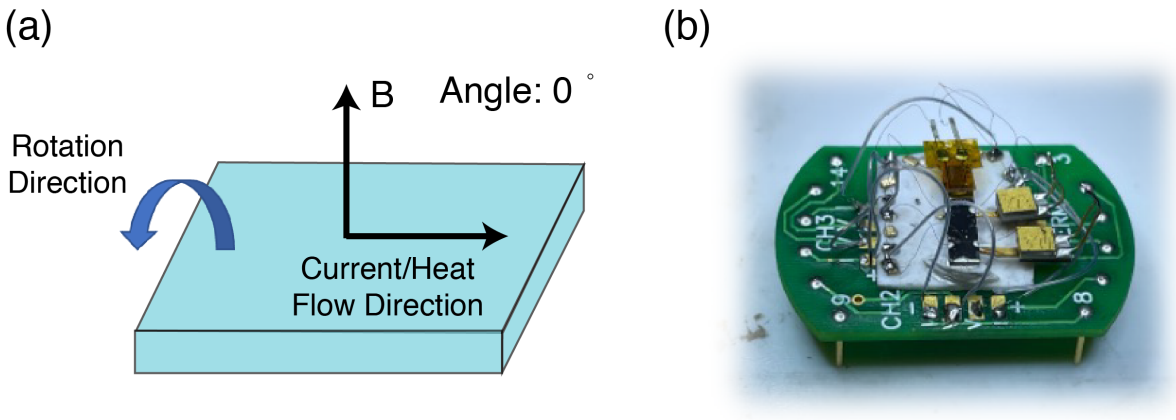

Figure 1.3: **Rotation thermoelectric measurement setup.** (a) Schematics of the rotation setup. At a rotation angle of 0 degree, the heat flow or current flow was applied along the sample, while the magnetic field was perpendicular to the sample.(b) Measurement device.

1.4 Scope and Organization of Thesis

The main focus of this thesis revolves around the investigation of transport phenomena, specifically carrier transport and thermal transport, within topological materials and organic semiconducting polymers. Both theoretical and experimental approaches are employed to achieve this goal, and novel characterization techniques are developed to support our research.

The thesis is structured into three main chapters, each delving into distinct topics. In Chapter 3, we utilize Monte Carlo simulation to explore photo-carrier dynamics and electron-matter interactions within the advanced characterization technique SUEM. Chapter 4 introduces the development of an optical spectroscopy technique TG, enabling us to characterize carrier dynamics and heat transfer processes simultaneously within organic semiconductor heterojunctions. Furthermore, Chapter 5 provides a comprehen-

sive analysis of thermoelectric transport within confined thin films of topological Dirac semimetals, using a self-developed steady-state thermal transport system. To complement these chapters, Chapter 2 outlines the methodologies utilized in each project, including computational details, the development of TG, and the establishment of steady-state thermal transport measurement systems.

Chapter 2

Methods

2.1 Computational Methods

2.1.1 Monte Carlo Simulation

Monte Carlo simulation is a well-established statistical technique for simulating the generation and interaction of SEs, backscattered electrons, and X-rays in electron microscopy and monitoring the trajectories and the properties of these particles, including the energy loss, mean free path, and escape probability [67, 68, 69, 70, 71]. Generally, Monte Carlo method is a step-wise simulation of electron trajectory by generating random numbers and predicting the scattering events based on the probability distribution from quantum mechanics. The simulated processes include tracing the trajectories of PEs, determining the position and results of scattering events, deciding the generation of SEs in the event of inelastic scattering and calculating the transmission probability of SEs at the sample surface. In the simulation, each simulated electron, either a PE or an SE, had a unique trajectory and experienced a separate sequence of scattering processes. By simulating a

large number of trajectories, Monte Carlo simulation results can accurately match the experimental results and enable the analysis of the influence of multiple factors on the SEY. Our Monte Carlo simulation followed common procedures as detailed in [72] and [73] and briefly summarized in the following paragraphs in this section.

The main principle of the Monte Carlo method is to simulate electron scattering events by generating random numbers following particular distributions. All random numbers mentioned in this section followed a uniform distribution between 0 and 1. The path length traveled by one electron between two consecutive scatterings followed a Poisson distribution and was calculated by $\Delta s = -\lambda_{\text{tot}} \ln r_1$, where Δs denoted the path length, λ_{tot} was the total mean free path, and r_1 represented the assigned random number [73]. The total mean free path was calculated through

$$\lambda_{\text{tot}} = \frac{1}{\frac{1}{\lambda_{\text{el}}} + \frac{1}{\lambda_{\text{in}}}}, \tag{2.1}$$

where λ_{el} was the mean free path for elastic scatterings and λ_{in} was the mean free path for inelastic scatterings.

The elastic mean free path was related to the elastic scattering cross section through

$$\lambda_{\text{el}} = \frac{1}{\sigma_{\text{el}} n_{\text{tot}}}, \tag{2.2}$$

where σ_{el} was the elastic scattering cross section and n_{tot} was the total number density of the atomic nuclei in the sample. The electronic elastic differential cross section in silicon as a function of the polar angle $\frac{d\sigma}{d\theta}$ was obtained through the NIST Electron Elastic-Scattering Cross-Section Database [74], which was based on the Mott theory of relativistic elastic scattering in a central field [75]. Since the elastic scatterings occur

between electrons and the atomic nuclei, we assumed that the elastic scattering cross sections are not affected by photoexcitation, given the quantum states of the atomic nuclei are insensitive to low-energy visible photons.

Electrons can also undergo inelastic scatterings with other electrons inside the sample. During an inelastic scattering event, both the momentum and the energy of the participating electrons are altered. Since the inelastic scattering happens between electrons, the inelastic scattering mean free path λ_{in} should depend on both the local number density and the energy distribution of the electrons in the sample, which can be significantly changed by photoexcitation. Therefore, in order to evaluate how photoexcitation affects the SEY, it is necessary to quantitatively examine the impact of photoexcitation on the inelastic scattering mean free path. The inelastic scattering reflects the collective response of the "electron sea" inside the sample to an incident electron, and thus, can be described by the dielectric function $\varepsilon(\mathbf{q}, \omega)$, where $\mathbf{q}$ is the momentum transfer during the scattering, and $\hbar\omega$ equals the energy loss ΔE of the incident electron due to the scattering [76]. Within the linear response theory, the differential inelastic scattering mean free path can be connected to the dielectric function through [77]

$$\frac{d^2\lambda_{\text{in}}^{-1}}{d(\hbar\omega)dq} = \frac{1}{\pi a_0 E}\text{Im}\left[\frac{-1}{\varepsilon(q,\omega)}\right]\frac{1}{q}, \tag{2.3}$$

where a_0 is the Bohr radius and E is the kinetic energy of the electron experiencing the inelastic scattering. Therefore, the probability for an inelastic scattering event, the energy loss, and the angular distribution after the inelastic scattering event are entirely encoded in the function $\text{Im}[\frac{-1}{\varepsilon(q,\omega)}]$, which is termed the energy loss function (ELF). So our central task in this work is to evaluate how ELF is affected by photoexcitation, which we will detail in 2.1.2. After the differential inelastic mean free path is evaluated from

Eqn. 2.3, the total inelastic scattering mean free path can be obtained by integrating Eqn. 2.3 over all possible energy losses and scattering angles. In a semiconductor, the minimum energy loss ΔE_{min} is the band gap E_G, while the maximum energy loss ΔE_{max}, by convention, is half the kinetic energy of the incident electron.

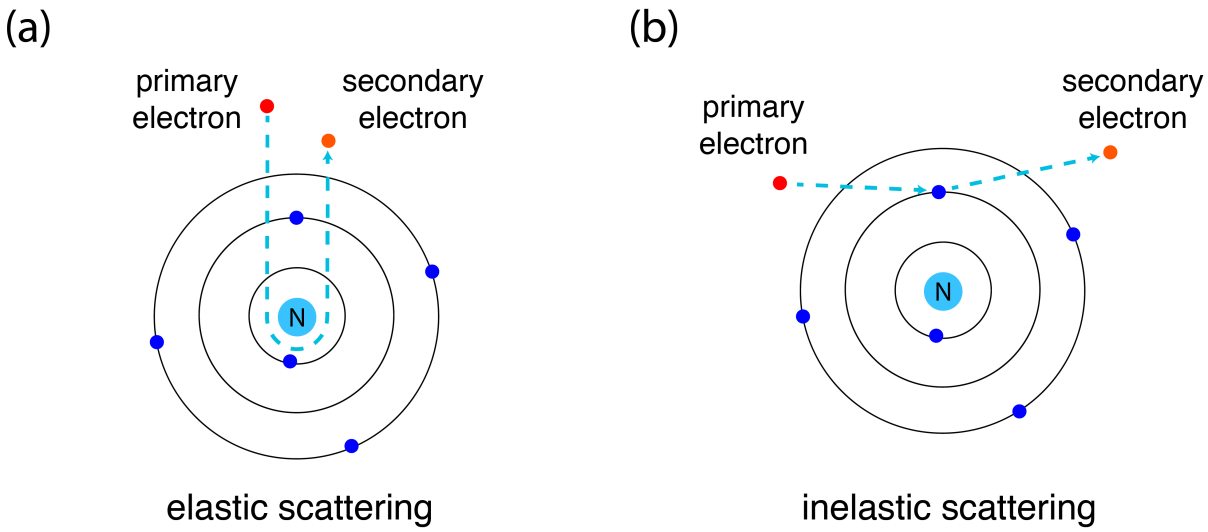

Figure 2.1: **Comparison of elastic scattering and inelastic scattering.** In elastic scattering, the primary collisions occur predominantly with the atomic nucleus, while in inelastic scattering, the primary collisions occur mainly with electrons. Since elastic collisions primarily involve interactions with the nucleus, the elastic cross sections remain unaffected by photoexcited carriers. Conversely, in inelastic scattering, where collisions occur with electrons, the inelastic cross sections are influenced by the presence of photoexcited carriers. Given that the inelastic scattering process relies on the ELF, it becomes essential to acquire the ELF under photoexcitation conditions.

After the travel path length is determined, another random number r_2 is used to determine whether the collision is elastic or inelastic by comparing it to the ratio of the cross sections

$$p_{\text{el}}(E) = \frac{\sigma_{\text{el}}(E)}{\sigma_{\text{el}}(E) + \sigma_{\text{in}}(E)} = \frac{1}{\lambda_{\text{el}}(E)}\Big(\frac{1}{\lambda_{\text{el}}(E)} + \frac{1}{\lambda_{\text{in}}(E)}\Big)^{-1}. \tag{2.4}$$

The collision is elastic when the random number is smaller than p_{el}, and inelastic otherwise. Once the type of scattering is decided, other random numbers are assigned to determine the change in the polar angle θ, the azimuthal angle ϕ, and the energy loss if

the scattering is inelastic. The change of the polar angle after both elastic and inelastic scatterings is determined by the corresponding differential cross sections. For elastic scatterings, the energy of the electron is conserved while its traveling direction is changed. The change in the polar angle θ after the scattering is determined by comparing the integrated differential cross section with a random number r_3:

$$\int_0^{\theta} \frac{d\sigma_{\text{el}}}{d\Omega} \sin\theta' \, d\theta' = r_3 \int_0^{\pi} \frac{d\sigma_{\text{el}}}{d\Omega} \sin\theta' \, d\theta', \tag{2.5}$$

where $d\Omega = \sin\theta \, d\theta$ is the differential solid angle. Here, although r_3 is uniformly distributed between 0 and 1, the θ values generated by solving Eqn. 2.5 follows the probability distribution determined by the differential cross section σ_{el}. This is the *inverse transform sampling* method to generate pseudo-random numbers that follow a given probability distribution [78]. The same method is used to determine other random variables such as energy loss in an inelastic scattering event. As for inelastic scatterings, the energy loss ΔE after one inelastic scattering can be determined using another random number r_4:

$$\int_{\Delta E_{\min}}^{\Delta E} \frac{d\lambda_{\text{in}}^{-1}}{d(\hbar\omega)} \, d(\hbar\omega) = r_4 \int_{\Delta E_{\min}}^{\Delta E_{\max}} \frac{d\lambda_{in}^{-1}}{d(\hbar\omega)} \, d(\hbar\omega). \tag{2.6}$$

The polar angle change after an inelastic scattering can be determined in a similar way as in Eqn. 2.5, where the differential inelastic scattering cross section should be used. In the actual simulation, the elastic and inelastic cross sections are pre-calculated and tabulated based on Eqn. 2.5 and Eqn. 2.6, and the corresponding scattering cross sections of an electron with a certain kinetic energy are then obtained by interpolating the tabulated values. The change in the azimuthal angle ϕ after both elastic and inelastic scattering events is uniformly distributed between 0 and 2π [72]. Another consequence of each inelastic scattering is the generation of a secondary electron, whose kinetic energy E_s

equals the difference between the energy loss of the primary electron and the band gap energy:

$$E_s = \Delta E - E_G. \tag{2.7}$$

The initial polar angle θ_s and the azimuthal angle ϕ_s of the secondary electron are related to the angle changes of the primary electron through momentum conservation [72]:

$$\sin\theta_s = \cos\theta, \;\; \phi_s = \pi + \phi. \tag{2.8}$$

Once the secondary electron is generated, its subsequent trajectory and scattering events will be tracked in the same way as described above, until it loses all of its kinetic energy or reaches the sample surface.

The status of each primary or secondary electron is checked after each scattering. Once one electron reaches the sample surface, its kinetic energy is compared with the surface energy barrier, the electron affinity χ. If its kinetic energy is higher than the electron affinity χ, the electron has a certain probability to escape the surface and contribute to the SEY. From elementary quantum mechanics, the transmission probability can be determined by the kinetic energy of the electron E, the incident angle α, and the electron affinity χ [79]:

$$T = \frac{4\left(1 - \frac{\chi}{E\cos\alpha}\right)^{1/2}}{\left[1 + \left(1 - \frac{\chi}{E\cos\alpha}\right)^{1/2}\right]^2}. \tag{2.9}$$

The electron is transmitted if a generated random number r_8 is smaller than the transmission rate, where the refraction angle satisfies $\sin\alpha' = \left(\frac{E}{E-\chi}\right)^{1/2}\sin\alpha$, where α' is the final escape angle into the vacuum [79]. Otherwise, the electron is either terminated when its kinetic energy could not overcome the electron affinity or reflected back into the material and continues moving. Since the SPV effect will change the effective surface

energy barrier for the escape of secondary electrons, we will discuss how the change of χ quantitatively affects the SEY in a later section. Finally, the SEY is calculated by repeating the above procedures for a large number of primary electrons. For this work, 10^7 primary electrons were simulated in each case.

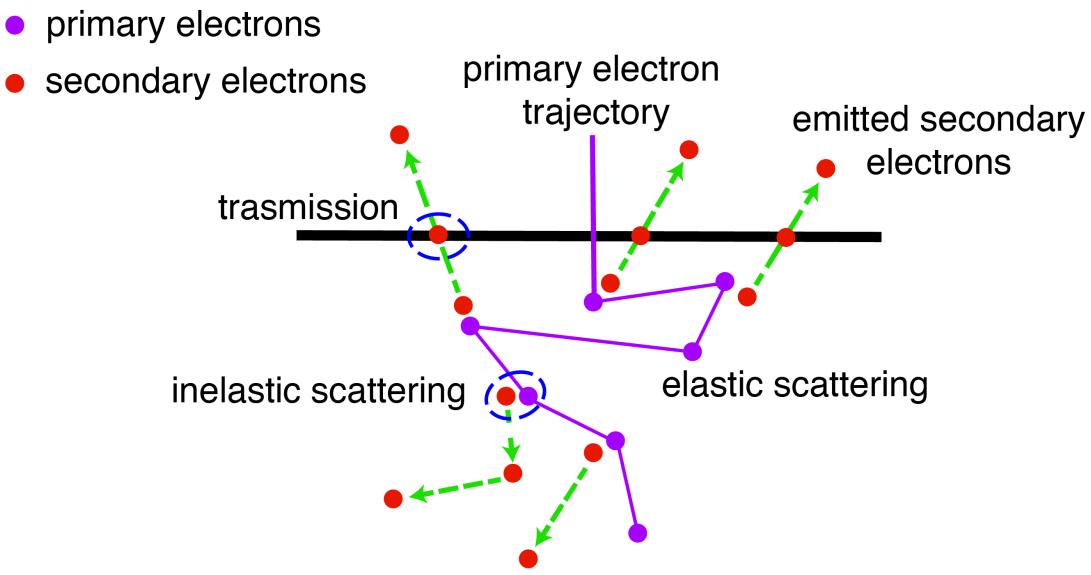

Figure 2.2: **Schematics of electron movements inside the materials.** Upon the incidence of primary electrons into the materials, they undergo two main scattering processes: elastic scattering and inelastic scattering. These processes are characterized by their respective cross sections. As the electrons approach the surface, they possess the potential to transmit through it, leading to the emission of secondary electrons. These emitted secondary electrons can be employed to visualize the carrier dynamics.

2.1.2 Evaluating the Energy Loss Function

Many methods have been developed to calculate ELF. For example, ELF with zero momentum transfer $\mathrm{Im}\left[\frac{1}{\varepsilon(q=0,\omega)}\right]$ can be obtained from optical and electron energy loss spectroscopy (EELS) measurements and parameterized into the sum of a series of Drude-

Lindhard-type terms [72]:

$$\mathrm{Im}\left[\frac{-1}{\varepsilon(q=0,\omega)}\right]=\sum_{i=1}^{N}a_i\frac{\omega_{pi}^2\gamma_i\omega}{\left(\omega^2-\omega_{pi}^2\right)^2+\left(\gamma_i\omega\right)^2}, \tag{2.10}$$

where ω_{pi} is the frequency of the i-th plasmon peak, γ_i is the associated damping coefficient, and the expansion coefficients a_i are used to fit the experimental data. The $q=0$ ELF can then be extrapolated to finite momentum transfer by utilizing the quadratic plasmon dispersion relation:

$$\omega_{pi}(q)=\omega_{pi}(q=0)+\frac{\hbar^2q^2}{2m}, \tag{2.11}$$

where m is the electron mass [80]. Although this Drude-Lindhard (DL) model has been extensively used in Monte Carlo simulations of high energy electrons in solids, for our purpose, we need to compute the ELF from first principles in order to incorporate the photoexcitation effect. Later, we will use the DL model to benchmark our results.

In this work, we adopted time-dependent density functional theory (TDDFT) to evaluate the ELF from first principles [81]. TDDFT has emerged as a tool to evaluate the dielectric properties of crystals, even in excited states [82, 83]. The principles of computing the dielectric function using TDDFT can be found elsewhere [81] and are only briefly summarized here. First, the independent-particle polarizability $\chi^0_{\mathbf{G},\mathbf{G}'}(\mathbf{q},\omega)$ as a matrix in the basis of the plane waves labeled by the reciprocal lattice vectors $\mathbf{G}$ and $\mathbf{G}'$ can be calculated with the eigenvalues and wavefunctions obtained from solving Kohn-Sham equations in a standard DFT calculation citehung2016interpretation. Then, the TDDFT full polarizability $\chi_{\mathbf{G},\mathbf{G}'}(\mathbf{q},\omega)$ can be calculated through the Dyson equation:

$$\chi_{\mathbf{G},\mathbf{G}'}(\mathbf{q},\omega)=\chi^0_{\mathbf{G},\mathbf{G}'}(\mathbf{q},\omega)+\chi^0_{\mathbf{G},\mathbf{G}'}(\mathbf{q},\omega)[v(\mathbf{q})+f_{xc}(\mathbf{q},\omega)]\chi_{\mathbf{G},\mathbf{G}'}(\mathbf{q},\omega), \tag{2.12}$$

where $v(\mathbf{q})$ is the Coulomb potential and $f_{xc}(\mathbf{q},\omega)$ is the energy-dependent exchange-correlation kernel. In this work, we utilized a bootstrap exchange-correlation kernel [84] that includes effects beyond the random phase approximation. Next, the microscopic dielectric function $\varepsilon_{\mathbf{G},\mathbf{G}'}(\mathbf{q},\omega)$ is connected to the polarizability within the linear response theory [73]:

$$\varepsilon^{-1}_{\mathbf{G},\mathbf{G}'}(\mathbf{q},\omega) = \delta_{\mathbf{G},\mathbf{G}'} + v(\mathbf{q})\chi_{\mathbf{G},\mathbf{G}'}(\mathbf{q},\omega). \tag{2.13}$$

In systems where the local-field effect can be neglected, the macroscopic dielectric function $\epsilon(\mathbf{q},\omega)$ can be simply computed by:

$$\varepsilon(\mathbf{q},\omega) = [\varepsilon^{-1}_{\mathbf{G}=\mathbf{0},\mathbf{G}'=\mathbf{0}}(\mathbf{q},\omega)]^{-1}, \tag{2.14}$$

from which the ELF can be obtained. Due to the heavy computational cost to calculate the full $\mathbf{q}$- and ω-dependent ELF, we instead calculated the ELF with $q = 0$ and extrapolated it to finite q values using the plasmon dispersion relation (Eqn. 2.11), following the optical-data model by Ashley [80]:

$$\mathrm{Im}\left\{-\frac{1}{\varepsilon(\mathbf{q},\omega)}\right\} = \int_0^\infty \mathrm{d}\omega' \left(\frac{\omega'}{\omega}\right) \times \mathrm{Im}\left\{-\frac{1}{\varepsilon\,(0,\omega')}\right\} \delta\left(\omega - \omega' - \frac{\hbar}{2m}\mathrm{q}^2\right). \tag{2.15}$$

We used the ELK code [85] for the TDDFT calculations in this work. Specifically, we used a local spin-density approximation to the exchange-correlation functional for the ground-state DFT and the bootstrap kernel f_{xc} for the TDDFT [84]. A k-point sampling mesh of $15 \times 15 \times 15$ was used with a plane-wave cut-off energy of 200 eV. These parameters were tested to ensure the convergence of the results.

Our calculated zero-momentum ELF of silicon assuming an electron temperature of 300 K is shown in Figure. 2.3(a), in comparison to experimental data and the DL model.

The experimental data is from the Handbook compiled by Palik [86], and the DL model parameters are from Sun *et al.* [87]. From Figure. 2.3(a), the TDDFT calculation reproduces the low-energy-loss part of the ELF (below 10 eV) well while the position and the width of the bulk plasmon peak near 20 eV are slightly off from the experimental data measured by electron energy loss spectroscopy (EELS). This is most likely due to the fact that the electron temperature could be much higher than 300 K during the EELS measurement. The electron temperature effect will be discussed in detail in Sec. 3.2.1. Nevertheless, using the ELF calculated from TDDFT, we were able to obtain SEY from the Monte Carlo simulation in good agreement with experiments [Figure. 2.3(e)]. In addition, high-energy-loss channels associated with core electron ionizations (near 100 eV and 2000 eV in silicon [87]) are not considered in this work since the core electrons are not influenced by photoexcitation in the visible range. In Figure. 2.3(b), we further test the ELF by checking the oscillator-strength sum rule (the "f-sum" rule) [88] based on the Kramers-Kronig relation:

$$Z_{\text{eff}} = \frac{2}{\pi \Omega_p^2} \int_0^\infty \omega \text{Im}\left[\frac{-1}{\varepsilon(\mathbf{q},\omega)}\right] d\omega, \tag{2.16}$$

where $\Omega_p = \sqrt{4\pi n_a}$ with n_a being the atomic number density of the material, and Z_{eff} is the effective number of charge per atom. From Figure. 2.3(b), the f-sum rule integration up to 100 eV of our calculated TDDFT approaches 4, the number of valence electrons per silicon atom, as expected. In Figure 2.3(c), we show the momentum- and energy-loss-dependent ELF after extrapolating the $q = 0$ ELF using Eqn. 2.15. Figure 2.3(d) shows the cumulative inelastic scattering cross section as a function of energy loss after scattering, demonstrating the major contribution of the bulk plasmon peak near 17 eV. Figure 2.3(e) compares the SEY generated using the Monte Carlo simulation with the ELF calculated from TDDFT to the experimental data compiled by Joy [89] as a function

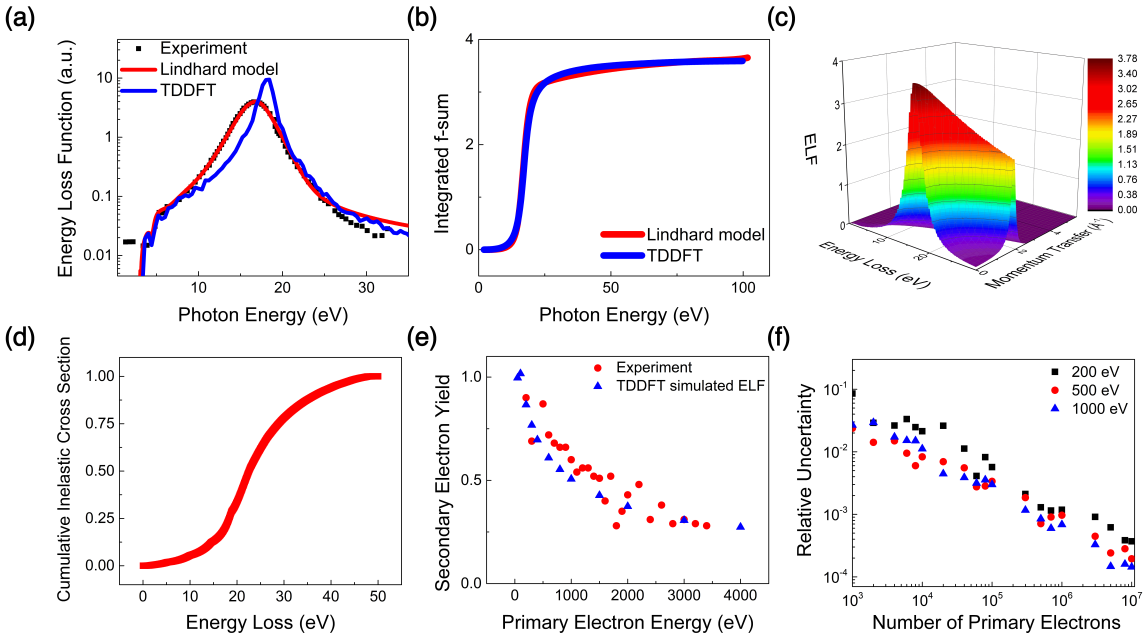

Figure 2.3: **Benchmarking the Monte Carlo Simulation.** (a) Comparing the ELF calculated using TDDFT to the experimental data and the Drude-Lindhard model. Experimental data is from Palik[86].(b) Checking the f-sum rule for the ELF. (c) The momentum- and energy-loss-dependent ELF after extrapolating the $q = 0$ ELF calculated with TDDFT. (d) The cumulative inelastic scattering cross section calculated from the TDDFT ELF. (e) Comparing the SEY calculated using the TDDFT ELF to the experimental data. The experimental data is from Joy[89]. (f) Scaling of the relative uncertainty of the Monte Carlo simulation as a function of the number of PEs simulated.

of the incident PE energy. Reasonable agreement is achieved, considering the sizable scatter of the experimental data. Particularly, the peak SEY around 200-eV PE energy is reproduced. In Figure. 2.3(f), we further tested the statistical uncertainty of the SEY in the Monte Carlo simulation as a function of the number of independent PEs simulated. The statistical uncertainty is critical for our work since we anticipate that the change in SEY induced by photoexcitation to be quite small. As shown in Figure. 2.3(f), the relative statistical uncertainty in the SEY is reduced to below 0.1% when 10^7 PEs are simulated at different PE energies, defining the resolution of our Monte Carlo study.

2.2 Transient Grating Spectroscopy

2.2.1 Experimental Setup and Working Principles

In the TG setup, illustrated schematically in Figure. 1.2, an optical diffraction grating ("phase mask") separates the pump and probe beams into ±1 diffraction orders, and a two-lens confocal imaging system is employed to recombine the pulses at the sample at a controlled crossing angle θ. The two crossed pump beams with the crossing angle θ create an interference pattern with a period of $L = \lambda/[2\sin(\theta/2)]$, where λ is the wavelength of the pump light. The decay of the intensity of the transient gratings is monitored by diffraction of a probe laser beam, and the grating period will determine the transport distance of both heat and photocarriers, which, in our setup, was varied between 2 and 10 μm.

The pump pulses of 515 nm and 260 fs pulse width (Clark-MXR IMPULSE) have a fluence of 120 nJ/cm^2 with a diameter of 99 μm and a repetition rate of 250 kHz. The continuous wave (CW) 532 nm probe beam has a power of 421 mW/cm^2 with a diameter of 83 μm. The time resolution of this TG implementation is limited by the bandwidths of the photodetector and the oscilloscope and estimated to be a few nanoseconds.

2.2.2 Heterodyne Detection

The TG setup employs optical heterodyne detection [50, 90]. One arm of the probe beam is attenuated with a neutral density filter to serve as a local oscillator (the reference beam). The diffracted signal is coherently superposed with the reference beam, and then they are directed into a fast photodiode (Hamamatsu C5658). The signal is subsequently read out using an oscilloscope (Tektronix TDS784A). The heterodyne de-

tection can increase the signal-to-noise (S/N) ratio and simplify the analysis and the interpretation of the measurements [50, 91].

To boost the S/N ratio of the TG experiments, an attenuated beam at the probe wavelength (the "local oscillator" or the reference beam) is used to interfere with the diffracted probe beam. The relative phase between the diffracted probe beam and the reference beam can be controlled by a transparent phase-delay plate. The implementation and the data analysis are detailed in refs [50, 91]. Briefly, by controlling the relative phase between the probe and the reference, either "amplitude grating" or "phase grating" can be selected using the heterodyne detection scheme. Amplitude grating refers to the change of the real part of the reflectivity in the reflection geometry or the transmissivity in the transmission geometry, which can be caused by either temperature change or photocarrier generation. Phase grating refers to the change of the imaginary part of the reflectivity or transmissivity, which can also be induced by temperature change of photocarrier generation. In addition, phase grating also has a contribution from the surface displacement of the sample due to thermal expansion, which has the complementary error function dependence.

By controlling the phase of the reference oscillator in the heterodyne scheme, either amplitude grating (when the oscillator phase is set to 0 or π) or phase grating (when the oscillator phase is set to $\pm\pi/2$) can be selected (See refs [50, 91]). We used phase grating measurement for this work since it is less sensitive to the absolute phase of the oscillator. This means our TG signal includes three contributions: 1) the surface displacement due to thermal expansion ($D \propto \mathrm{erfc}(q\sqrt{\alpha t})$, as in Eq. (1) of the main text); 2) the changes of the imaginary part of the transmissivity (which is proportional to the absorption coefficient) due to temperature change, and 3) the change of the imaginary part of the transmissivity due to photocarrier generation. It is well established that contribution 2) is

only significant in metals when compared to the other two contributions (refs [50, 52, 91]). In semiconductors, since the thermal energy associated with the temperature change (typically a few K) is much smaller than the band gap (which controls the absorption coefficient), the thermal reflectance (or transmittance) signal is much lower than that caused by photocarrier generation, which happens on the scale of the pump photon energy. This is how we separated different contributions to the TG signal in our data analysis detailed in the main text.

2.2.3 Sample Preparation

P3HT/PCBM samples with different PCBM concentrations are prepared by spin-casting solutions of P3HT:PCBM dissolved in 1,2−dichlorobenzene onto cleaned glass substrates inside an inert atmosphere glovebox. The solution is approximately 4 wt.% added solids. A spin-speed of approximately 800 rpm produce samples with thicknesses ranging from 50 nm to 250 nm (determined after all measurements using an Ambios XP-100 profilometer). After spin-casting, samples are annealed in the glovebox at 150 °C for 15 minutes, followed by encapsulation with another clean glass slide with epoxy around the edges, with a gap between the sample surface and the encapsulation slide. Encapsulation of the samples ensure no contamination by water or oxygen during the TG measurements.

2.3 Steady-State Measurement Systems

A commercial 9 T Dynacool Physical Property Measurement System (PPMS, Quantum Design) is applied for conducting the steady-state measurements. Moreover, the Thermal Transport option (TTO) is used for measuring the thermal conductivity κ, Seebeck coefficient S, and electrical resistivity ρ. The temperature range for our experiments

span from 2 K to 300 K, and we apply a magnetic field of up to 9 T. Single measurement mode is applied to obtain the steady-state measurements. Figure 2.4(a) illustrates the four-probe measurements employed in TTO, where a heat flow or current is applied to one end of the sample, and exits at the heat sink. The thermometer shoes record the temperature and voltage of the hot and cold sides. Specifically, the thermometer shoe assemblies are equipped with a thermistor Cernox 1050 thermometer and a voltage lead that is soldered to the shoe itself, where the voltage wires enable the electrical voltage detection. Similarily, the heater shoe assembly consists of a resistive heater chip where the resistance is 2000 Ω, along with an electrical current source lead (I^+) that is also soldered to the shoe.

The TTO is a valuable tool for measuring the thermoelectric Seebeck effect, and it enables simultaneous measurements of temperature and voltage variations in response to a heat pulse applied to one end of the sample. The Seebeck coefficient, which involves monitoring the electrical voltage drop accompanying a temperature change across specific materials, is obtained by:

$$S = -\frac{\Delta V}{\Delta T} \tag{2.17}$$

Furthermore, the TTO system enables the evaluation of thermal conductivity κ through the formula:

$$\kappa = \frac{L}{A}\frac{P_{ht} - P_{rad} - P_{shoes}}{\Delta T} \tag{2.18}$$

where L and A represent the length and cross-section of the samples, respectively. The terms P_{ht}, P_{rad}, and P_{shoes} correspond to the input power, radiant loss, and parasitic heat loss from the thermal shoes, respectively. The radiation heat loss is described by:

$$P_{rad} = \sigma_T (D/2)\epsilon(T_{hot}^4 - T_{cold}^4) \tag{2.19}$$

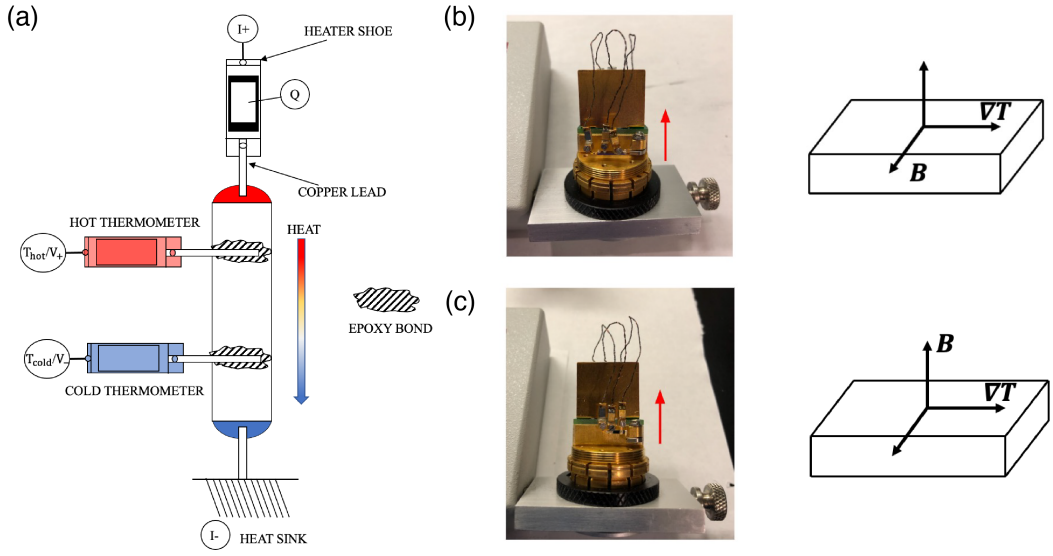

Figure 2.4: **Four probe measurement techniques.** (a) Schematics of the measurement device. In (b) and (c), the samples are positioned within the TTO pucks. The arrow direction in (b) and (c) indicates the orientation of the magnetic field. Specifically, the magnetic field is parallel to the sample in (b) and perpendicular to the sample in (c). The heat and current flow direction is from the left to right.

where σ_T is the Stefan-Boltzmann Constant, D and ϵ are the surface area and infrared emissivity of the sample respectively, and the radiation heat loss term becomes very small below 200 K for most of the materials. The shoe conductance ($\kappa_{shoes} = \frac{P_{shoes}}{\Delta T}$) is approximated by a polynomial with the form:

$$\kappa_{shoes} = d(aT + bT^2 + cT^3) \tag{2.20}$$

where a, b, c and d are empirically calibrated constants, and the thermoshoes are calibrated using the Nickel samples. Additionally, the TTO system incorporates the standard four-probe resistivity provided by the PPMS AC Transport Measurement System (ACT) option (Model P600) to measure the electrical resistivity (ρ).

Silver epoxy is utilized to establish electrical connections between the sample and the four copper wires, followed by curing for 30 min at approximately 400 K on a hot plate.

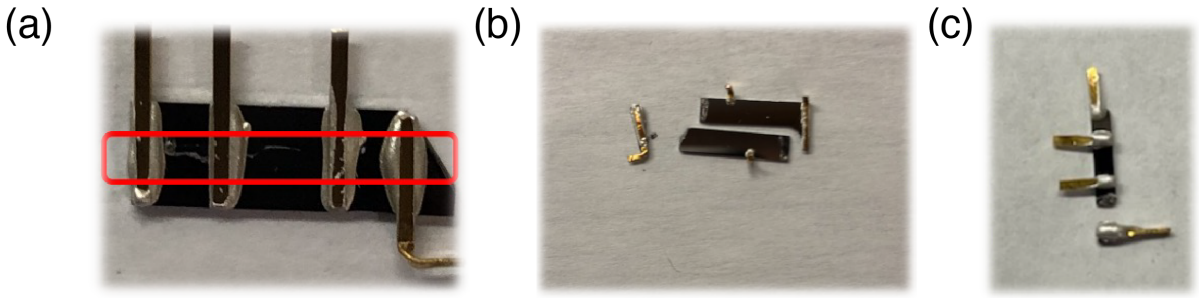

Figure 2.5: **Cd_3As_2 samples with silver epoxy contacts.** The contact area decrease from (a) to (c), and the minimum contact area is limited by the size of the Cu lead in (c).

It is essential to note that achieving reliable contact can be challenging. For the Cd_3As_2 samples, the mismatch of thermal expansion coefficients between Cd_3As_2 and the silver epoxy results in sample cracks at cryogenic temperatures. Figure 2.5 shows examples of Cd_3As_2 samples with cracks. We observed that reducing the contact area decreases the likelihood of sample cracking. However, the minimum contact area is limited by the size of the lead, as shown in Figure 2.5(c). Furthermore, reducing the sample's contact area also decreased parasitic heat loss, which becomes significant in low thermal conductance samples, for example, the disentangled ultra-high molecular weight polyethylene (UHMWPE) films [92]. This aspect will be further discussed in the subsequent section. The encountered issues with sample cracking have motivated the development of new characterization techniques.

Upon establishing the contact, the samples are mounted to the TTO puck, as depicted in Figure 2.5b,c. Within the cryogenic chamber, the magnetic field is oriented upwards. The arrangement of the shoes from left to right comprises the heater, hot thermometer shoe, and cold thermometer shoe, indicating the direction of heat and current flow from left to right. In general, two distinct configurations are employed: one with the magnetic field parallel to the sample surface (Figure 2.5b) and the other with the field perpendicular to the sample (Figure 2.5c). Nevertheless, achieving precise control over the angle between

the sample and the magnetic field poses challenges. The persisting misalignment issues in this setup give rise to substantial geometric errors. These misalignments exert notable impacts on the transport properties, particularly in topological systems owing to their high electron mobility [58, 93], thereby complicating the interpretation of the sample's behavior.

Analogous to the transverse Hall effect, there exists a transverse thermoelectric effect known as the Nernst effect. The Nernst coefficient, denoted as N_{xy}, characterizes the generation of a transverse electric field, E_{xy}, when a heat flux Q_{xx} is applied to a material subjected to a perpendicular magnetic field, B_z. Specifically, in response to the heat flux, electrons and holes diffuse from the hot end to the cold end, and, akin to the Hall effect, experience deflection due to the Lorentz force, resulting in their accumulation on opposite sides of the sample. In the context of two-carrier systems, the Nernst effect characterizes the collective influence exerted by both carriers, resulting in notable effects within such systems. The establishment of an equilibrium state is achieved through the creation of the electric field E_{xy}, which can be quantified by measuring the Nernst voltage, V_{xy}. The Nernst coefficient is mathematically defined as:

$$N_{xy} = \frac{1}{B_z}\frac{E_{xy}}{\Delta T_{xx}/dx} = \frac{1}{B_z}\frac{V_{xy}}{\Delta T_{xx}}\frac{X}{Y} \tag{2.21}$$

where X and Y represent the length along the x-direction and y-direction, respectively. However, the limited capability of the four probe TTO setup restricts its application to only longitudinal measurements, preventing the possibility of conducting transverse thermoelectric Nernst measurements.

2.4 Customized Steady-State Measurement

In order to address the aforementioned challenges, we develop and build a customized steady-state measurement system. This customized setup facilitates the execution of transverse thermoelectric measurements. Through the manipulation of the heat sink stage geometry, we are able to precisely control the angle between the magnetic field and the samples. Moreover, we have implemented strategies to minimize the contact area, thereby establishing point contacts, and have devised distinct bonding materials tailored to the specific characteristics of different kinds of the samples.

2.4.1 Measurement Principle

The selection of an appropriate temperature sensor is important for conducting accurate thermal measurements. It is essential that the temperature sensor possesses a low thermal conductance to minimize heat loss. Additionally, it should be suitable for small sample sizes while meanwhile offering accuracy within the desired measurement range. To meet these requirements, we utilize a self-fabricated 25 μm Type T thermocouple in our experiment. This thermocouple has low thermal conductance with its thin wires, and it effectively addresses the issue of heat loss. Furthermore, its small size facilitates the reduction of contact area and form the point contacts, mitigating the risk of aforementioned Cd_3As_2 sample cracking. However, it is worth noting that thermocouples experience reduced sensitivity below 60 K. To address this limitation, we employ a Cernox thermistor from Lakeshore for temperature calibration at low temperatures. Moreover, the T-type thermocouple, consisting of Cu and Constantan wires, not only fulfills our temperature sensing needs but also serves for voltage measurements due to the inclusion of a Cu wire component.

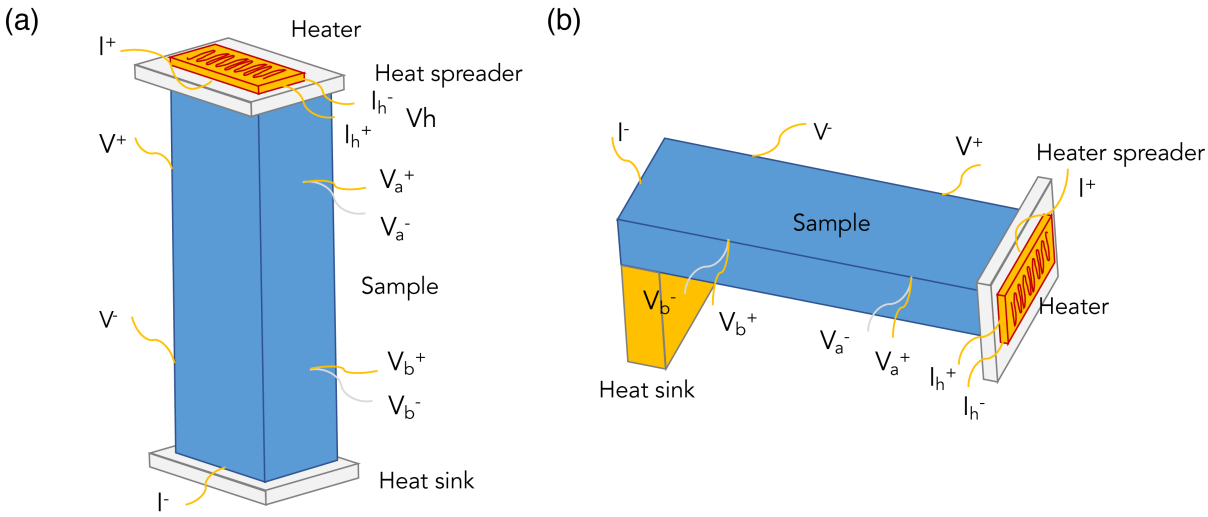

Figure 2.6: **Schematics of customized steady-state measurement systems.** (a) and (b) are measurement devices for bulk samples and thin film samples, respectively. The T type thermocouples are made from Cu (V_a^+ and V_b^+) and Constantan (V_a^- and V_b^-).

Figure 2.6 depicts the schematics of our customized steady-state measurement systems, designed for two typical sample types: bulk samples and thin film samples measurement devices, as shown in Figure 2.6(a) and Figure 2.6(b), respectively. This system facilitates simultaneous electrical and thermal measurements. The top of the sample is equipped with a 120-Ω strain gauge heater, with adjustable heating power to achieve a temperature rise of $1 \sim 3$ % in thermal measurements. A Cu heat spreader is connected to ensure a uniform heat distribution over the surface. Between the heater and heat spreader, a 25 μm Cu wire serves as the current-in (I^+) wire for electrical measurements. Additionally, for both the hot and cold ends, a 25 μm Cu wire and a thermocouple are placed on the left and right sides, respectively. In the case of the bulk sample in Figure 2.6(a), a current-out (I^-) wire is sandwiched between the sample and heat sink for conducting electrical measurements, while for the thin sample in Figure 2.6(b), a current-out wire is positioned at the end of the sample. Ultimately, the samples are placed on sapphire heat sinks.

For electrical measurements, a current flow is applied to both the current-in and current-out wires. The 25 μm Cu wires, along with the Cu wires from the T type thermocouples at both the hot and cold ends, serve as voltage detectors. The longitudinal voltage difference can be read from either the left side or the right side as $\Delta V_{xx} = V^+ - V^- = V_a^+ - V_b^+$. Using the longitudinal voltage difference, we can determine the longitudinal resistivity as follows:

$$\rho_{xx} = \frac{Wt}{L}\frac{\Delta V_{xx}}{I_{xx}} \tag{2.22}$$

where L, W, and t represent the length, width, and thickness of the sample, respectively. Additionally, this setup allows for conducting transverse Hall measurements. The transverse Hall voltage can be read through either V^+ and V_a^+, or V^- and V_b^+. The Hall coefficient is defined as the transverse voltage increase with a longitudinal current flow under a perpendicular magnetic field. If we use the hot side to obtain the Hall voltage, the Hall coefficient can be calculated as follows:

$$RH_{xy} = \frac{1}{B_z}\frac{E_{xy}}{j_{xx}} = \frac{1}{B_z}\frac{V_{xy}/W}{I_{xx}/t} = \frac{1}{B_z}\frac{(V^+ - V_a^+)/t}{I_{xx}} \tag{2.23}$$

where the Hall resistivity is given by:

$$R_{xy} = \frac{E_{xy}}{j_{xx}} = \frac{V_{xy}/W}{I_{xx}/t} = \frac{(V^+ - V_a^+)/t}{I_{xx}} \tag{2.24}$$

The thermal and thermoelectric properties can be determined using similar methods. To measure the thermal conductivity, a current is applied to the heater, and the power flowing into the system is given by $Q_{in} = I_h V_h$. The local temperatures at the hot and cold ends are recorded by two thermocouples, denoted as T_h and T_c, which yield the longitudinal temperature gradient as $\Delta T_{xx} = T_h - T_c$. With the known input heat power,

we can calculate the thermal conductivity as follows:

$$\kappa_{xx} = \frac{L}{Wt}\frac{Q_{in}}{\Delta T_{xx}} \tag{2.25}$$

Similarly, utilizing the longitudinal voltage and temperature gradient, we can obtain the Seebeck coefficient:

$$S_{xx} = -\frac{\Delta V_{xx}}{\Delta T_{xx}} \tag{2.26}$$

Furthermore, the Nernst coefficient can be expressed as:

$$N_{xy} = \frac{1}{B_z}\frac{E_{xy}}{\Delta T_{xx}/dx} = \frac{1}{B_z}\frac{L}{W}\frac{V_{xy}}{\Delta T_{xx}} = \frac{1}{B_z}\frac{L}{W}\frac{V^+ - V_a^+}{\Delta T_{xx}} \tag{2.27}$$

In conclusion, the customized steady-state measurement system is capable of conducting both electrical and thermal measurements, offering a significant advantage over the TTO system as it allows us to perform transverse thermoelectric measurements.

2.4.2 System Development

The customized measurement system utilizes the PPMS cryogenic chamber as its foundation and integrates external devices to facilitate our experiments. A Keithley 6221 current source provides the required power supply, while voltage measurements are conducted using Keithley 2182A nanovoltmeters. For thermal and thermoelectric measurements, the local temperature is determined by reading the voltage between the two ends of thermocouples via the Keithley 2182A nanovoltmeters, which offers a remarkable voltage resolution as low as 1 nV.

Generally speaking, the measurements involve multi-channel voltage detections, encompassing both electrical and thermoelectric measurements. For electrical measurements,

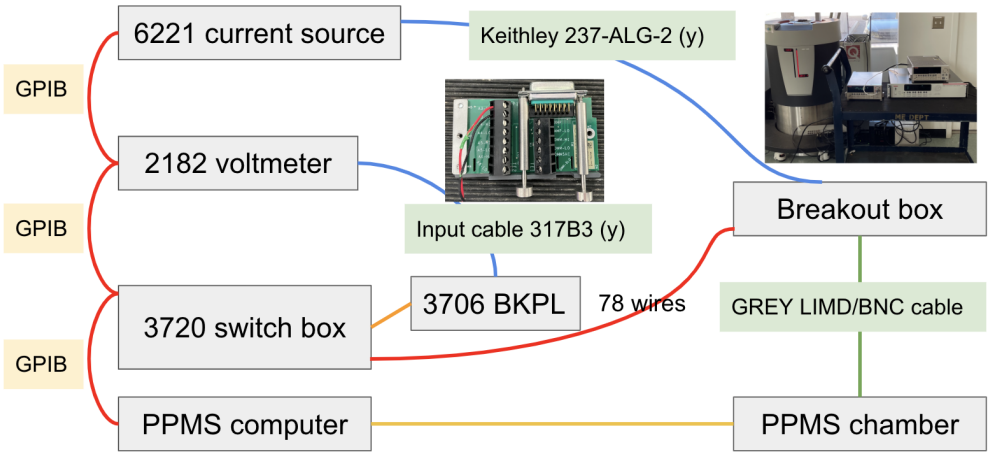

Figure 2.7: **Layout of customized steady-state measurement systems.** The connection of the external devices and PPMS chamber is presented here. he upper-right image shows the experimental setup at UCSB.

two voltage gradients are necessary—one along the x-direction and the other along the y-direction. As for the thermoelectric measurements, except for longitudinal Seebeck voltage and transverse Nernst voltage, two additional voltage readings from the thermocouples are required. To facilitate the multi-channel measurements, a Keithley 3706A switch box equipped with a 3720 plug-in card is utilized. This switch box enables us to switch between different measurement channels during our measurements, allowing us to employ a single nanovoltmeter to measure multiple voltages. The input connector from the nanovoltmeter is connected to the switch box back panel using Keithley 3706-BKPL. The rear plane of 3720 plug-in card offers 78 pins, with 60 of them available for use, corresponding to 30 channels. These 60 pins are connected with the PPMS breakout box, which, in turn, connects to the PPMS chamber through LIMD/BNC cables. In summary, this configuration enables us to switch between different voltage measurement channels within our experimental setup.

The current source, nanovoltmeter, and switch box are connected to the PPMS control

computer via GPIB for seamless communication. To efficiently manage experimental control and data acquisition, a customized LabVIEW control code is utilized. The switch time between different channels is set at 2 sec. During thermoelectric measurements, the heater remains open for 5 to 10 min to establish the desired temperature gradient. For the Cd_3As_2 samples, the magnetic field was swept from -9 T to 9 T with a sweeping rate of 5 mT/s.

2.4.3 Sample Preparation

The 25 μm copper and constantan wires are securely spot welded using a 4 V voltage. As illustrated in Figure 2.8, the top ends of both wires should contact with each other. Detailed sample preparation steps are depicted in Figure 2.9, and Cd_3As_2 sample preparation for both electrical and thermal measurements is used as an example here. Firstly, a sample stage is carefully cut from sapphire, ensuring its dimensions are smaller than 1 cm. Subsequently, the Cu contact pins are attached to the sample stage using silver epoxy, with a heating time of approximately 30 minutes. A sapphire heat sink can be cut into different shapes, where silver epoxy is also utilized to establish a secure connection between the heat sink and the sample stage. The sample will be placed on top of the heat sink, while the sample stage is positioned on the puck, with the magnetic field always pointing up. By modifying the shape and angle between the heat sink and sample stage, we have the flexibility to adjust the angles between the sample and magnetic field.

The subsequent procedure involves preparing the heater, as depicted in Figure 2.9b. 25 μm Cu wires or thermocouples are soldered to the heater's lead using rosin-based Sn/Pb/Ag (62/36/2) solder material at a temperature of 280 °C. It is important to mention that the surrounding plastic parts of the heater can be trimmed for smaller

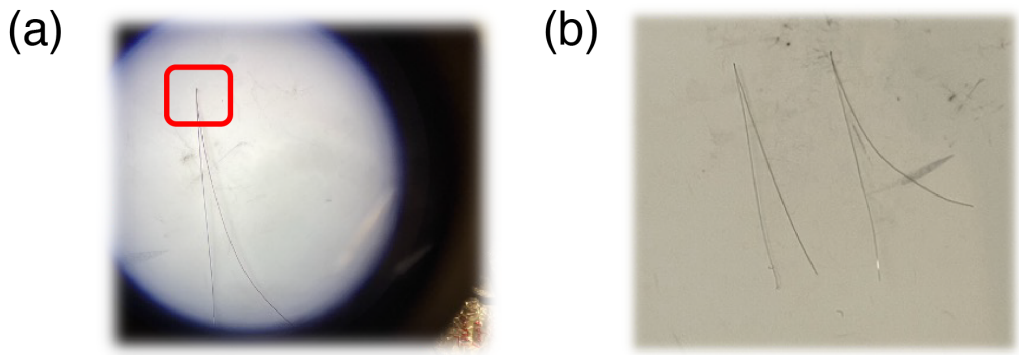

Figure 2.8: **Thermocouples are fabricated by spot welding.**

samples. Next, the current-in wire is placed between the sample and Cu plate. Once the sample stage and heater are ready, we attach the Cu wires and thermocouples to the samples using silver epoxy to form good electrical contacts, as illustrated in Figure 2.9c. This step forms point contacts, resulting in much smaller contact areas compared to the TTO samples. For the current-out wire, we apply a line of silver epoxy to ensure a uniform electric field during measurements. Subsequently, in Figure 2.9d, the heater is affixed to the sample using silver epoxy. The final step involves soldering all the wires to the sample stage. For each pin, a 25 μm Cu or constantan wire is soldered to another Cu wire with insulation layers. These Cu wires are then soldered to the ACT puck to avoid the short circuit. Notably, the ACT puck has 12 pads, providing the maximum number of soldering points.

To establish electrical contacts, we primarily utilize silver epoxy due to its high electrical and thermal conductance properties. However, in specific scenarios, we have explored alternative bonding materials. For instance, for mounting contacts to polymer samples, cryogenic GE varnish (GE7031, Lakeshore) proves effective. The GE varnish ensures good thermal contact while maintaining electrical insulation. The curing process for the varnish occurs at room temperature over a period of 24 hours. The GE varnish can be

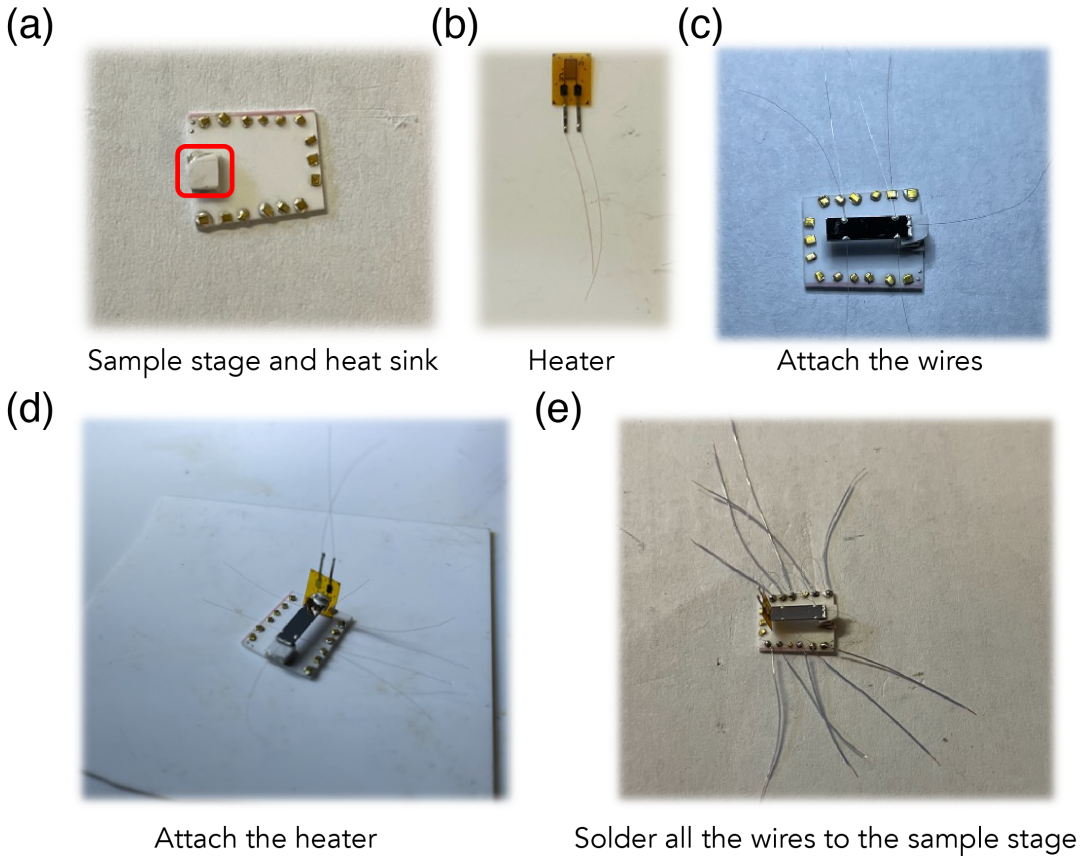

Figure 2.9: **Sample preparation procedures.** (a) Make the sample stage and heat sink. (b) Prepare the heater with the solder. (c) Attach the Cu wires and thermocouples to the samples. (d) Attach the heater to the samples. (e) Solder all the wires to the sample stage.

easily washed off using toluene, and it lacks robust mechanical strength. Additionally, we employ Loctite Stycast for contact formation. The Stycast is mixed with Henkel Loctite catalyst in a mass ratio of 100:3.6. After a curing time of 7 hours, the non-removable Stycast becomes fixed and exhibits excellent mechanical strength.

In addition to the Cd_3As_2 samples, we also apply our measurement systems to conduct thermal and thermoelectric measurements on various other samples. Among these, Figure 2.10a depicts the kagome lattice CoSn, which exhibits a bar-shaped structure. Dealing with this sample is challenging due to its very small size, measuring only around

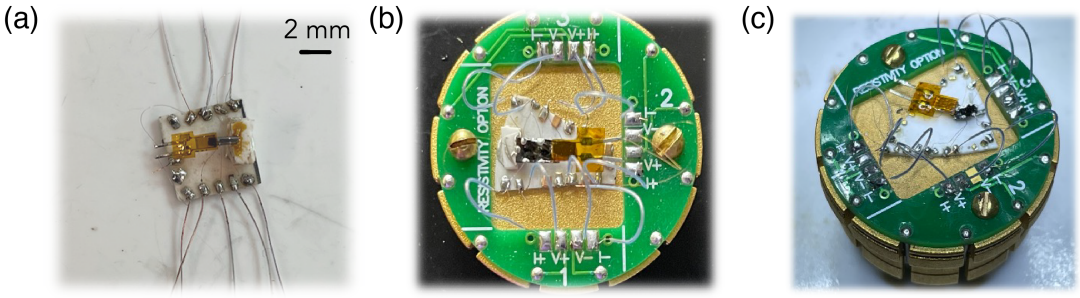

Figure 2.10: **Inorganic samples on the customized measurement devices.** (a) CoSn sample (b) CsV_3Sb_5 sample (c) Sn-doped CsV_3Sb_5 sample.

2 mm. Figure 2.10b and Figure 2.10c display the superconducting CsV_3Sb_5 samples with a thickness of less than 100 μm. These experiments demonstrate the capability of our technique in measuring thermal and thermoelectric properties under cryogenic temperatures and high magnetic fields.

2.4.4 Angle-Dependent Measurement

A picture of the experimental setup using a rotation sample stage is provided in the Figure 1.3. Horizontal rotator from Quantum Design is applied and it enables the sample stage to be rotated over a full 360° under the magnetic field. The motor controlling the rotator operates at an impressive resolution of 0.0011° per step. The rotator puck shares similarities with the ACT puck, boasting 12 pads. However, the rotator thermometer is wired to contact pads 3 through 6, thus leaving us with 8 available pads for conducting measurements.

As for Cd_3As_2 samples, at a rotation angle of 0 degree, the heat flow or current flow is applied along the sample, while the magnetic field is perpendicular to the sample as shown in Figure 1.3a. Angle-dependent measurements is taken at 15-degree intervals between 0 and 180 degrees. The magnetic field was swept from -9 T to 9 T, and measurements

included Shubnikov-de Haas (SdH) oscillations, as well as thermoelectric oscillations (i.e. oscillations in Seebeck and Nernst coefficients at higher magnetic fields).

The raw data is fitted using polynomial equations to establish a baseline, which are subsequently subtracted to isolate the oscillations. Following the subtraction, Fast Fourier Transform (FFT) analysis are performed to extract the oscillation frequencies. The FFT range selected for analysis us from 2 T to 8.5 T, as lower field values lead to no discernible oscillations and high noise is observed near 9 T. For the 25-nm Cd_3As_2 sample, a comparative analysis is conducted on both Seebeck and Nernst oscillation signals to ensure the presence of the same oscillation frequencies in both measurements.

2.4.5 Steady-State Measurements for Polymers

So far, our discussion remains on the measurements for inorganic samples. Moreover, we have successfully modified this system to accommodate the measurement of drawn polyethylene (PE) films, as described in the work by Kim *et al.* [92]. The experimental measurements are conducted using the TTO setup. However, we encounter challenges as the silver epoxy fails to adhere to the PE surface, and the polymer sample cannot withstand high temperatures due to its low melting point. To address these issues, we employ GE varnish to mount the lead. Figure 2.11b illustrates the PE samples with the GE varnish contacts.

Furthermore, as the drawn ratio of the PE samples is increased, a notable reduction in their thickness is observed, which is around 10 μm. Consequently, the mechanical bond between the PE samples and the GE varnish weakens considerably. When attempting to mount the samples onto the measurement shoes, the leads attached by GE varnish exhibit a tendency to peel off from the samples. To address this issue, we use the Stycast to make

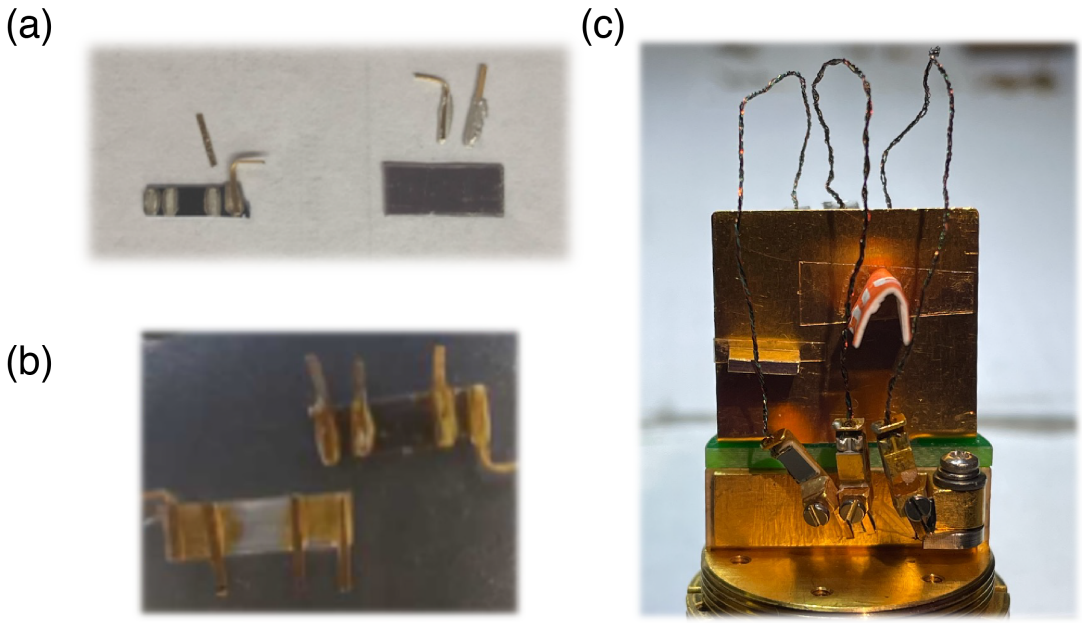

Figure 2.11: **PE samples with different contacts.** (a) Silver epoxy is applied, forming contacts with silicon on the left side and with PE on the right side. The leads are taken off from both samples. As a comparison, silver epoxy doesn't adhere effectively to the PE surface. (b) The PE samples with GE varnish contacts. (c) The PE samples mounted in the TTO puck with the Stycast contacts. The contacts are mechanically stronger than the GE varnish.

the contacts. Specifically, a systematic method is developed to sandwich the samples securely between layers of Stycast. Through the implementation of this approach, the problem of sample peeling is successfully resolved, as evidenced in the results depicted in Figure 2.11c.

In addition to the mechanical bonding strength, the reduction in sample thickness also leads to a decrease in its thermal conductance. The reduction of sample's thermal conductance results in significant parasitic heat loss from the lead, which, in turn, tends to overestimate the thermal conductivity values. Consequently, the use of TTO options for our measurements becomes impractical under these circumstances. To solve these challenges, we have developed and implemented our customized steady-state measurement system specifically tailored for polymer characterization. Unlike the TTO leads,

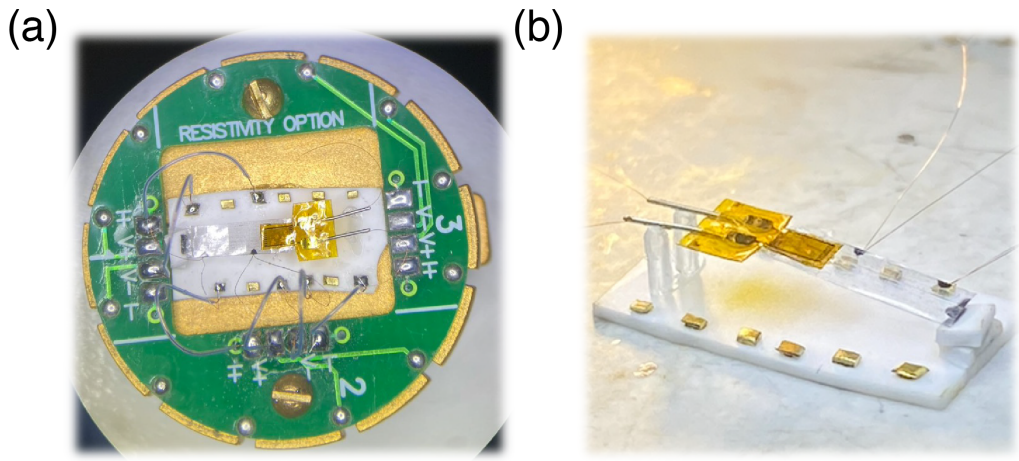

Figure 2.12: **PE samples integrated with customized steady-state measurement systems.** The heater is placed on the polymer stands (a) top-view (b) side-view.

the thermocouples utilized in our system are remarkably thin, providing high thermal resistance and effectively mitigating parasitic heat loss. This improvement allows for more accurate and reliable measurements of the thermal conductivity of polymers.

Figure 2.12 illustrates the PE samples integrated with our customized steady-state measurement systems. Notably, in contrast to inorganic samples, polymer specimens possess a lightweight and soft nature. Therefore, the conventional approach of attaching the heater directly to one end of the polymer sample causes instability, leading to its downward displacement on the heat stage. To resolve this issue, we have introduced a polymer stand (Natural PP) to provide support for the heater, as depicted in Figure 2.12b. The implementation of this stand offers enhanced stability and enables successful stretching of the sample in a straight configuration, thereby minimizing measurement errors associated with thermal conductivity. Furthermore, the polymer stand exhibits a notably low thermal conductance of 0.11 W/m-K, effectively reducing heat loss from the heater side during the measurements.

Chapter 3

Impact of photoexcitation on secondary electron emission: a Monte Carlo study

3.1 Introduction

As explained above, SUEM contrast images reflect the change in the number of emitted SEs (SE yield, or SEY) from each location on the sample surface as a result of photoexcitation[17], as illustrated in Figure 1.1b. Thus, the key to understanding SUEM contrast mechanisms is to examine how the SE generation, transport, and emission processes are affected by photoexcitation. Currently, several SUEM contrast mechanisms have been proposed, which can be categorized into bulk effects and surface effects [17], as summarized in Figure3.1. The bulk effects are illustrated in Figure 3.1a. When electrons and holes are generated by photoexcitation in the bulk, the photo-excited electrons

possess a higher energy and have a higher probability of escaping as SEs after interacting with the PEs. This mechanism indicates that the photo-illuminated area should show a higher SEY and, thus, a "bright" contrast in the SUEM images. This mechanism, although not quantitatively examined so far, has been used to interpret the early SUEM results [18, 19].

In addition, the photogenerated bulk carriers can also collide with SEs during their transport to the surface and prevent them from escaping the material surface, leading to a reduction of the SEY and a "dark" SUEM contrast. This mechanism was used to explain the dark SUEM contrasts observed on GaAs surfaces [94]. Furthermore, the photoexcitation can also change the sample surface voltage and cause the surface electronic energy band to bend, known as the surface photovoltage effect (SPV) [95]. This effect is graphically illustrated in Figure 3.1b. On semiconductor surfaces, defects and dangling bonds can pin the surface Fermi level and lead to the bending of electronic bands near the surface that is associated with a surface electronic field. This surface field can facilitate or hinder the transmission of SEs across the sample surface, depending on the band bending direction. This effect is well known to cause different SEM image intensities from n-type and p-type surfaces [95]. Photoexcited charge carriers can compensate for the surface bending (the SPV effect), and thus modify the SE escape probability and the SEY. Figure 1.2b shows the scenario in n-type silicon, where the surface bands bend upward near the surface under the dark condition, creating a surface negative polarity that hinders the SE escape. In this case, SPV compensates for the surface band bending and the associated negative polarity and lowers the surface barrier for SEs to escape, leading to a higher SEY and a bright SUEM contrast. Li *et al.* experimentally verified the impact of the SPV effect by observing a brighter (darker) SEM contrast in n-type (p-type) silicon under illumination compared to the dark state [25]. The SPV effect at an internal in-

terface was also recently studied using SUEM [21]. Despite these previous efforts, there is no quantitative understanding of the relative contribution of these mechanisms to the SUEM contrast. This lack of understanding poses an obstacle to obtaining quantitative information from SUEM images. Therefore, it is necessary to develop a computational approach to clarify the contributions from various contrast mechanisms.

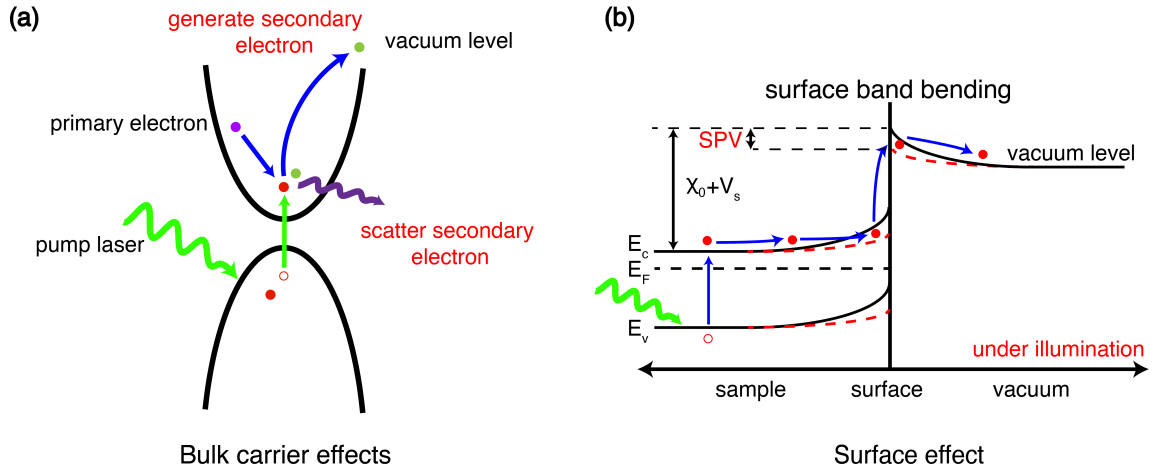

Figure 3.1: **Proposed SUEM Contrast Mechanisms.** (a) Schematic illustrating the SUEM contrast mechanism due to the generation of photocarriers in the sample bulk. The presence of photocarriers with higher energy can both increase the generate rate of secondary electrons and scatter the secondary electrons during their transport. (b) Schematic illustrating the surface photovoltage effect in n-type silicon. The black lines depict the energy band diagram in the dark condition, where χ_0 is the electron affinity and V_s is the surface band bending due to Fermi level pinning. The red dashed lines depict the energy band diagram under photo-illumination. The photocarriers compensate for the surface band bending and reduces the effective potential barrier for SEs to escape. SPV: surface photovoltage. E_c: conduction band bottom. E_v: valence band top. E_F: Fermi level.

In this work, we implemented a Monte Carlo simulation assisted with time-dependent density functional theory (TDDFT) to quantitatively study the SUEM image contrast under photoexcitation with both bulk photocarrier effects and the surface SPV effect in the model system silicon and with PE energy from 50 eV to 1 keV. In particular, we used TDDFT to compute the effect of photoexcitation on the electron energy loss function (ELF) in silicon, and then used the ELF as input to a Monte Carlo simulation

to evaluate the impact of photoexcitation on SEY. Our study laid the foundation for the future development of SUEM as a quantitative imaging tool.

3.2 Results and Discussion

3.2.1 Bulk Effect

As discussed above, photoexcitation can generate excess electrons and holes in the sample that can impact the SEY. As proposed in previous SUEM papers [18, 17], excess electrons (holes) increase (decrease) the local average electron energy, thus increasing (decreasing) the generation rate of SEs locally. In addition, excess electrons and holes inside the sample can scatter with the SEs inelastically during their transport inside the sample [94], thus reducing the number of SEs that can escape the sample surface. In principle, both effects are encoded in the ELF, which governs the SE generation and inelastic scattering processes. Furthermore, we focus on the bulk plasmon peak near 17 eV in silicon that is associated with its valence electrons that can be directly excited by the incident visible photons. In this section, we analyze how the ELF is affected by the presence of excess electrons and/or holes using TDDFT.

We simulated the effect of excess charge by adding extra electrons or holes in the TDDFT calculation. Considering practical optical excitation conditions [96], we simulated the excess carrier concentration up to 10^{21} cm^{-3} that is below the damage threshold of silicon. The added electrons and holes occupy the bottom of the conduction band and the top of the valence band, respectively. In the electron case, the added electrons occupy the six equivalent electron pockets along the $\Gamma - X$ direction in the Brillouin zone. In the hole case, the added holes occupy the hole pocket at Γ point. The calculated ELFs

with different excess electron concentrations are shown in Figure 3.2a.

A small shift of the plasmon peak position is observed. The plasmon frequency ω_p is proportional to $\sqrt{n_e}$, where n_e is the density of valence electrons. In silicon, n_e can be calculated to be 5×10^{22} cm^{-3}. Therefore, a change in the valence electron density Δn_e due to the presence of excess electrons and holes can lead to a change in the plasma frequency on the order of $\frac{\Delta n_e}{2n_e}$. Thus, we expect a blue (red) shift of the plasmon peak by roughly 1% when the excess electron (hole) concentration is 10^{21} cm^{-3}. This change in the ELF is small, mainly due to the fact that the concentration of excess charge that can be photoexcited is much lower in comparison to the valence electron concentration. In typical SUEM measurements with a pump photon energy of 2.4 eV, photoexcitation mainly generates excess electrons and holes near the band gap of the material, which will affect the inelastic scattering events on the energy scale of the band gap (1.1 eV in silicon). Since these scattering events occur at a much lower energy scale than the electron affinity (4.05 eV in silicon) that SEs need to overcome to escape, they are not expected to alter the SEY collected in SUEM experiments.

Although the change in the bulk plasmon peak due to photoexcitation is small (on the order of 0.1 eV and lower, depending on the photocarrier concentration), this small change can, in principle, be amplified due to the large number of inelastic scattering events experienced by each PE. Therefore, we still proceeded with Monte Carlo simulation and quantitatively evaluated the effect of the bulk photogenerated carriers on the SEY. In Figure 3.2b, we show the SEY from the Monte Carlo simulation with different excess electron or hole concentrations up to 10^{21} cm^{-3} for the PE energy range below 1 keV. With the uncertainty level of $\sim$0.1% achieved by simulating 10^7 PEs, the changes in SEY caused by the photocarriers are comparable to the uncertainty level. Furthermore, considering the fact that electrons and holes coexist after photoexcitation and their excess

concentrations cancel each other, we conclude here that the existence of photogenerated bulk carriers does not lead to sufficient changes in the SEY that can be detected within SUEM. This conclusion is consistent with a qualitative argument order-of-magnitude analysis provided by Zhang *et al.* [97], and we provided the numerical proof here.

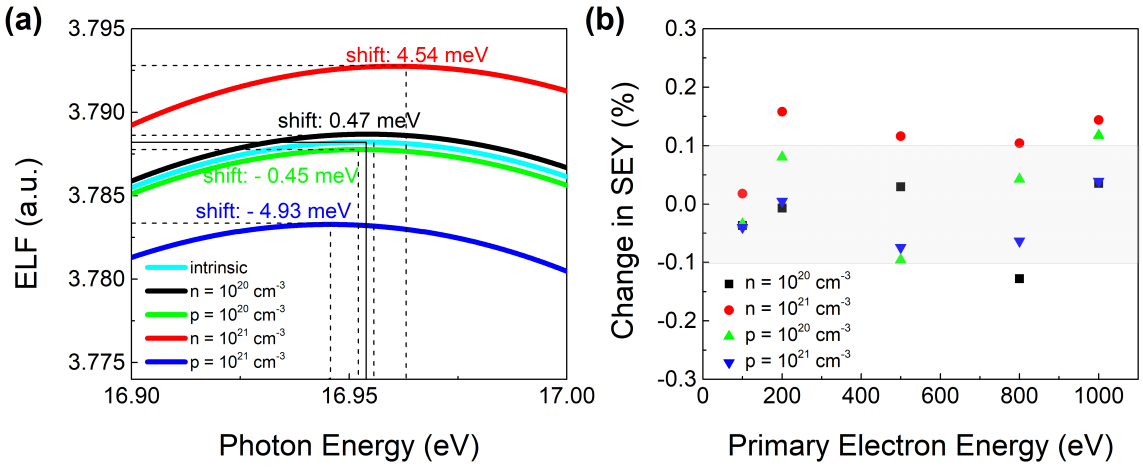

Figure 3.2: **Impact of the Bulk Photocarriers on the Secondary Electron Yield.** (a) The ELF in the presence of excess electrons or holes calculated by TDDFT. The shift of the bulk plasmon peak is labeled in the figure. (b) The changes in the SEY from the Monte Carlo simulation taking into account the changes in the ELF. The gray zone labels the relative uncertainty in the Monte Carlo simulation with 10^7 primary electrons simulated.

The analysis in this section so far has assumed that the photogenerated bulk carriers are in thermal equilibrium with the lattice. In practice, however, immediately after the excitation by a short optical pulse, the photogenerated electrons and holes can possess a high effective temperature depending on the frequency of the optical pulse used:

$$k_B T = h\nu - E_G, \tag{3.1}$$

where T is the effective charge carrier temperature, k_B is the Boltzmann constant and ν is the frequency of the optical pulse. With an optical pulse in the visible range, the effective temperature of the photogenerated "hot" electrons and holes can be as high as

tens of thousands of Kelvin [98]. Since the initial high temperature will lead to significant broadening of the electron distribution in the bulk on the order of a few eV, we expect this hot photocarrier effect can significantly alter ELF and influence the SEY. In fact, the hot carrier transport effect has been observed in SUEM experiments in a wide range of materials [19, 27, 99, 100].

Here, we simulated the hot carrier effect by adjusting the smearing width of the equilibrium electron distribution function in the TDDFT calculation of the ELF. As a first-order approximation, we set the smearing width of the equilibrium electron distribution function to be k_BT. We emphasize here that this approach is an approximation since we do not take into account the quasi-Fermi levels developed due to photoexcitation. This simplification leads to the consequence that the photocarrier concentration and the electron temperature are correlated in our simulation, while in real experiments these two parameters can be controlled independently. However, our simulation should be able to provide an order-of-magnitude estimation of the hot carrier effect on the SEY.

In Figure 3.3a, we compare the ELF calculated with an effective electron temperature at 300 K, 5000 K, and 10000 K, respectively. As expected, a higher effective electron temperature broadens the bulk plasmon peak in the ELF while suppressing its peak value, as required by the f-sum rule, since the total number of valence charge remains the same at different electron temperatures (in fact, the ELF calculated with an electron temperature of 10000 K reproduces the position and the width of the bulk plasmon peak measured experimentally by EELS, as shown in Figure 3.3b, suggesting the electrons could be in a highly nonequilibrium state during the EELS measurement). This indicates that a higher effective electron temperature will lead to excitation of SEs with a broader energy distribution near the bulk plasmon peak. In the process, more high-energy SEs can be created that can give rise to an increased SEY.

To quantitatively evaluate this effect, we conducted Monte Carlo simulation with the ELFs calculated at different electron temperatures. The result is shown in Figure 3.3b. Within the range of PE energies simulated in this work (100 to 1000 eV), the change in SEY due to a high effective electron temperature is quite significant. The largest increase in SEY is about 23% at 5000 K for a PE energy of 200 eV. Interestingly, SEY does not increase with temperature monotonically, since the SEY is higher at 5000 K than that at 10000 K. This can be understood since the broadening of the ELF with increasing temperature is also accompanied by a shift of the bulk plasmon peak towards lower energy, creating an opposite impact on SEY. This result suggests that the hot carrier effect right after photoexcitation can generate a strong contrast in SUEM experiments, while the presence of excess electrons and holes in bulk of the sample after they thermally equilibrate with the environment has a negligible effect on the SUEM contrast.

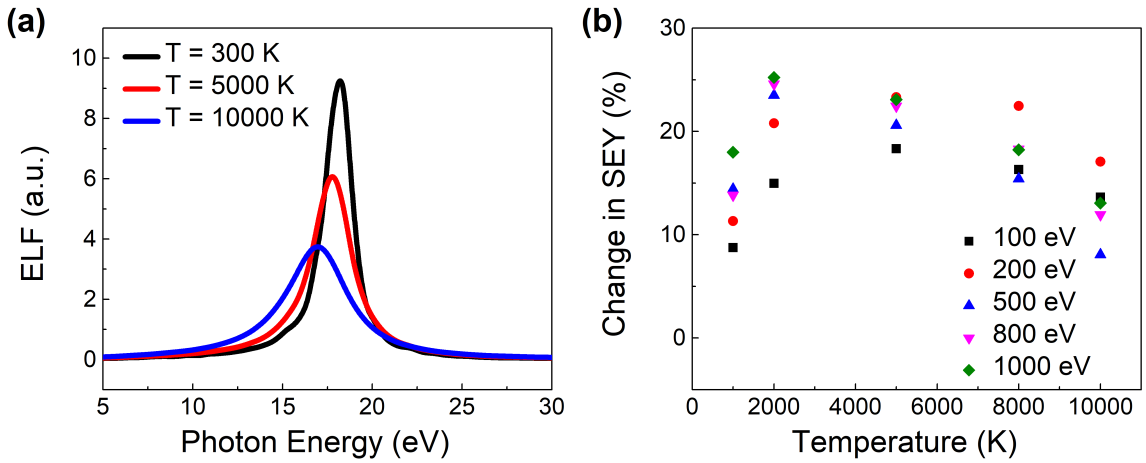

Figure 3.3: **Impact of Hot Photocarrier Effect on the Secondary Electron Yield.** (a) The ELF calculated by TDDFT with different effective electron temperatures. (b) The change in SEY due to different effective electron temperatures (compared to that at 300 K) from the Monte Carlo simulation as a function of the PE energy.

3.2.2 Surface effect

Besides the bulk carrier effects, photoexcitation can also induce the SPV effect, which modifies the surface transmission barrier for the SE escape that impacts the SEY. As explained in the Introduction section, the SPV was originated from the surface band bending in semiconductors due to the Fermi level pinning by surface defect states [101], which can be compensated by the photoexcited charge carriers [25]. In effect, the SPV changes the effective electron affinity χ in Eqn. 2.9, and thus, can be simulated by modifying the χ parameter in the Monte Carlo simulation. Zhang *et al.* [97] conducted a similar simulation of spherical nanoparticles. Our simulation results of a flat silicon surface are shown in Figure 3.4. In n-type silicon, the SPV effect leads to a reduction of the effective SE escape barrier, and thus, an increased SEY. The opposite effect occurs in p-type silicon. In both cases, we simulated an SPV voltage up to 250 meV, as has been measured experimentally in silicon [25]. For a given PE energy, the change in the SEY scales monotonically with the the SPV voltage in both n-type and p-type silicon. The change in SEY increases with increasing PE energy initially and seems to saturate around 1 keV PE energy. The change in SEY due to SPV is on the order of a few percent in our simulation, in agreement with the previous report by Zhang *et al.* [97]. This result indicates that once the photoexcited hot carriers cool down, the SPV effect plays a major role in determining the SUEM contrast, rather than the distribution of the bulk photocarriers. On the other hand, the SPV effect typically occurs on a slower time scale (hundreds of picoseconds) [25] depending on the surface charge capacity and the electrical conductance of the material. Therefore, the SUEM contrast on shorter timescales after photoexcitation should be dominated by the hot photocarrier effect based on our simulation result.

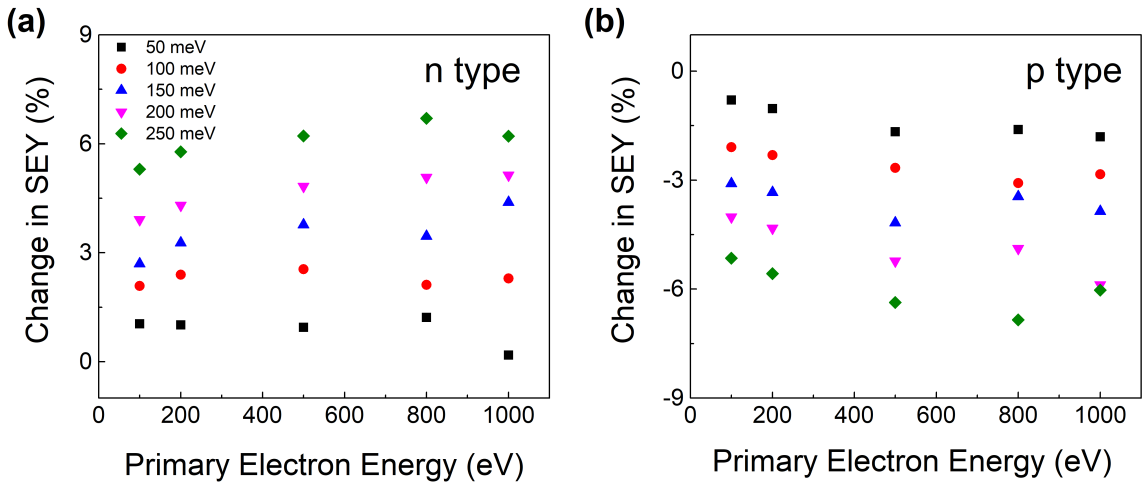

Figure 3.4: **Impact of the Surface Photovoltage Effect on the Secondary Electron Yield.** The change in the SEY as the effective surface potential χ is changed by different amounts, up to 250 meV, in (a) n-type silicon and (b) p-type silicon, as a function of the PE energy.

3.3 Conclusions

In summary, we quantitatively examined the impact of photoexcitation on the SEY by combining Monte Carlo simulation with an ELF calculated from TDDFT. The effect of both photoexcited carriers in the bulk and the altered surface potential is evaluated. We found that the hot carrier effect immediately after photoexcitation can have a strong impact on the SEY, while the mere presence of bulk photocarriers after they cool down leads to a negligible change in SEY. In addition, the SPV effect induced by the photocarriers near the sample surface adds another contrast mechanism to SUEM images. Due to the limit in computational resources, we only focused our study on low energy PEs below 1 keV and on silicon as a model system, so we caution against direct quantitative comparison to SUEM experiments with high PE energies (typically 30 keV) and in other materials. However, we believe the qualitative observations from this study still provide important physical insights into understanding the SUEM contrast, and we will follow up with simulations of higher PE energies and other materials in our future work.

Chapter 4

Transient grating spectroscopy of photocarrier dynamics in semiconducting polymer thin films

4.1 Introduction

In this work, we apply the TG technique to measure the grating decays in the model system regioregular poly(3-hexylthiophene) (P3HT) and its blend with the electron acceptor [6,6]-phenyl-C61- butyric acid methyl ester (PCBM). Charge transport in this system has been extensively studied [32, 31, 33, 102, 34], and a limited amount of work has been directed toward understanding the thermal properties [38, 42, 39]. In our study, we examined neat P3HT films and associated blends containing PCBM with a weight ratio of 1.8 % and 50 %, hereafter, 1.8 % and 50 % blend, respectively. By varying the excitation grating period, we were able to resolve both the excited state and heat relaxation pro-

cesses with the application of an appropriate model containing the two processes. It was found that the carrier dynamics are determined by multiple recombination mechanisms, while heat transfer was dominated by the response of the substrate. Our study suggests the TG technique can be a potentially versatile platform to characterize both photocarrier dynamics and thermal transport properties of semiconducting polymers.

Grating periods from ~ 3 um to ~ 9 um were adopted in our experiment, and the measured real-time decay data of the transient gratings with two periods (L ~ 8.81 um and 3.75 um) are shown in Fig. 2. The availability of a wide range of grating periods, which set the transport length scale, is one unique advantage of the TG technique: the grating-period-dependent decay rate provides information to the diffusion coefficients, while the grating-period-independent decay rate yields local dissipation or carrier recombination [103].

The TG technique monitors the decay of the magnitude of the transient gratings in time by measuring the intensity of the diffracted probe beam. The "magnitude" of the transient gratings is the change of the local optical refractive index caused by the pump excitation. Both photocarrier generation and temperature rise can lead to the change of the optical refractive index. Thus, in principle, the TG technique is sensitive to both the heat diffusion process and the photocarrier dynamics. In inorganic materials, these two processes typically happen over distinct time scales: the photocarrier dynamics typically occur within one nanosecond [104, 96], while the heat diffusion occurs in tens to hundreds of nanoseconds given micrometer-scale grating periods [54]. Therefore, this timescale separation usually prohibits simultaneous evaluation of the two processes in one measurement. In contrast, in semiconducting polymers, the photocarrier dynamics can persist for a much longer time, up to microsecond time scales, as revealed by TRMC measurements [31], which indicates that the TG signal will be potentially influenced

by both photocarrier dynamics and the heat diffusion process within the nanosecond to microsecond time window, and both processes need to be considered when interpreting the TG results.

4.2 Results and Discussions

4.2.1 Heat diffusion

The heat diffusion process is governed by the heat equation with a 1D-periodic initial temperature distribution. Generally, TG spectroscopy is used to detect thermal transport properties of suspended films [104, 105] or thick films on substrates [50, 54]. In our samples consisting of absorbing thin films on transparent substrates, the heat diffusion processes in both the thin film and the substrate contribute to the TG signal. In our case, the contributions cannot be precisely distinguished due to the similar thermal diffusivities of the thin film and the substate (~ 0.3 mm^2/s for both glass and typical polymers [106]). For the smallest grating period we used, the thermal penetration depth $d = L/\pi$ [52] was about 1 μm, indicating that the thermal transport properties can be effectively extracted for thicker polymer films with micrometer-scale thickness. Alternatively, pushing the grating period down to the diffraction limit using large aperture optics [51] or using short-wavelength ultraviolet light [107] can also enable significant thermal contribution from the top film. In our current study, the absorbing thin films act as surface heating sources of a semi-infinite medium and the contribution of the time-dependent decay of the surface temperature grating to the TG signal has the following form [50, 52]:

$$I(t) = D\text{erfc}(q\sqrt{\alpha_{th}t}) \tag{4.1}$$

where $\mathrm{erfc}(x) = \frac{1}{\sqrt{2\pi}} \int_x^\infty e^{-t^2}\, dt$ is the complementary error function, $q = 2\pi/L$ is the grating wave vector, $\alpha_{th} = 0.34 mm^2/s$ is the effective thermal diffusivity of the glass substrate, and D is a fitting parameter related to the initial temperature rise. As shown in Figure 4.1, there are significant deviations between the best fits using Eq. 4.1 and the experimental results indicating that the heat diffusion process alone cannot adequately explain the experimental results. The contribution from photocarrier dynamics must be taken into account.

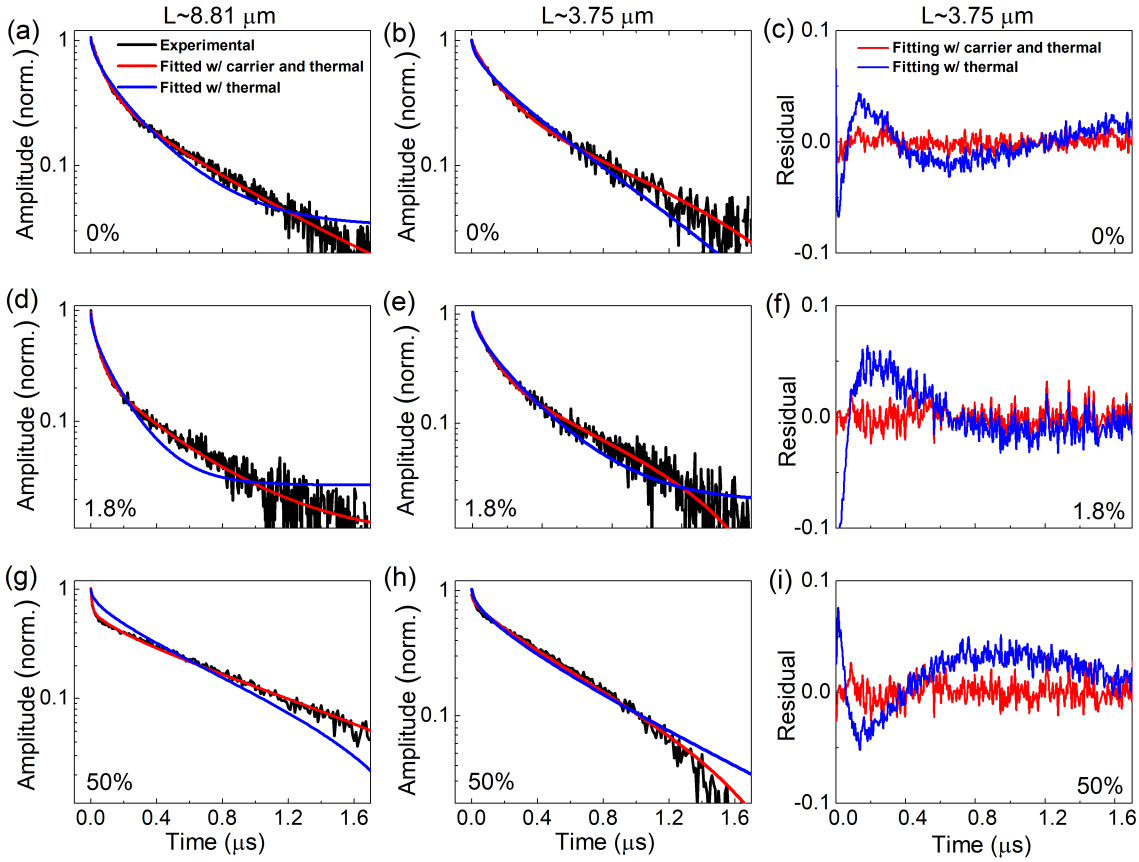

Figure 4.1: **The measured decay curves of the transient grating magnitudes and fitting curves.** (a)–(c) Neat P3HT, (d)–(f) 1.8% blend, and (g)–(i) 50% blend. Red solid lines represent fittings performed with combined carrier and thermal contributions, while the blue ones are with thermal contribution only. The left and middle panels are for the grating period of 8.81 and 3.75 μm, respectively, while the right panels are for the residuals of corresponding fittings for 3.75 μm grating data.

4.2.2 Carrier dynamics

In P3HT and its fullerene blends, it is well established that the photocarriers initially exist in the form of excitons, which quickly decay within a few nanoseconds in neat films and even faster in blends where the donor–acceptor interfaces strongly facilitate exciton dissociation into free charge carriers. These free charge carriers can persist much longer, up to microseconds, and in fact, their transport and recombination dynamics directly impact the performance of organic optoelectronic and photovoltaic devices [45, 108]. Even in neat P3HT without electron acceptors, it is reported that a significant amount of free charge carriers (up to 30 % of the total generated species) can be directly photoexcited [31, 109, 110]. The concentration of free charge carriers is expected to be much higher in the blends due to efficient exciton dissociation. Given the measurement window of our TG setup ($\sim$ ns to $\sim$ μs), the contribution to our TG signal is most likely from the dynamics of the photogenerated free charge carriers.

Considering first-order and second-order recombination processes [31, 33, 111] and carrier diffusion, the spatial-temporal evolution of the free charge carrier concentration $n(x,t)$ obeys the governing equation

$$\frac{\partial n}{\partial t} = \alpha_{pc}\frac{\partial^2 n}{\partial x^2} - \frac{n}{\tau} - Bn^2 \tag{4.2}$$

where α_{pc} is the diffusivity of the photogenerated free carriers, τ is the time constant for first-order recombination processes, and B is the second-order recombination coefficient. The general solution to Eq. 4.2 is

$$n = \frac{C}{\exp(At) - CB/A} \tag{4.3}$$

where $A = \alpha_{pc}q^2 + 1/\tau$ and C is a fitting parameter related to the initial photogenerated free charge carrier density. When the second-order recombination process is negligible, the solution simplifies to an exponential decay $n = C\exp(-At)$ due to first-order recombination and carrier diffusion. The recombination and carrier diffusion processes can be distinguished due to their different dependences on the grating wavevector q, which can be conveniently varied in the experiment by changing the grating period [103].

Taking into account the contributions from thermal transport and carrier dynamics, we combined Eqs. 4.1 and 4.3 to fit the experimental results, as shown in Figure 4.1. The fitting residuals are shown in Figure 4.1c, f, and i, clearly indicating the significant improvement of the fits when both thermal and carrier contributions are included. For neat P3HT and 1.8% blend samples, we find that the experimental results can be well fitted with only thermal transport and first-order recombination processes, while the experimental results for the 50% blend samples can only be fitted if the second-order recombination process is also included. This result reflects that the concentration of free charge carriers in neat P3HT and the 1.8% blend is low due to the low density of donor/acceptor interfaces to generate free charge carriers, so that first-order recombination processes, such as trap-assisted recombination, dominate.

We further verified the absence of higher-order recombination processes in these samples by varying the optical power of the pump and the probe beams as shown in Figure 4.2, where the decay rate A was found to be independent of the optical power (and thus the free charge carrier concentration). In contrast, in the 50% blend samples, which are employed for OPV fabrication, the interpenetration networks of the blend are known to be optimized and the interfacial area is maximized, resulting in optimal exciton dissociation at donor/acceptor interfaces [112, 113]. Therefore, the free carrier concentration in the 50% blend samples is much higher and the second-order bimolecular recombination among

free charge carriers becomes appreciable.

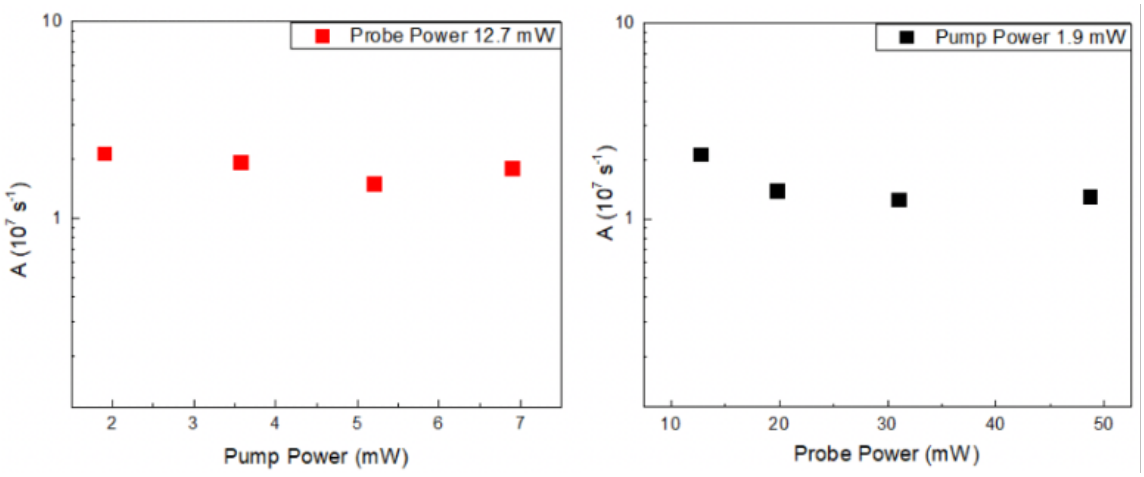

Figure 4.2: **The dependence of the first-order decay rate of the neat P3HT sample on the optical powers of the pump and the probe beam.** The decay rate in neat P3HT is independent of the optical powers, confirming the first-order nature of the free carrier recombination process.

The first-order decay rate A and the second-order recombination coefficient B extracted from our measurements as a function of the grating period are shown in Figure 4.3. It is observed that there is no apparent dependence of the first-order decay rate A on the grating period. This indicates that the carrier diffusivity is below the detection limit of the TG technique with micrometer-scale grating periods. A higher resolution of the diffusion coefficients can potentially be obtained with smaller grating periods [51, 107]. Given the number of fitting parameters (three for neat P3HT and 1.8% blends and four for 50% blends), the fitting sensitivity and uncertainty of these fitting parameters are critical. We analyzed the fitting uncertainty of each parameter by varying the parameter from the best fitted value until the accumulated deviation of the fitted curve from the experimental curve reaches 10%. The fitting uncertainty of the first-order decay rate A obtained this way is on the order of 5% in neat P3HT and 1.8% blends and roughly 10% in 50% blend [not shown in Figure 4.3a for clarity]. The fitting uncertainty of the second-order recombination coefficient B is roughly 10% for the 50% blend. The first-

order decay rates A are 1.4×10^7 s^{-1}, 2.4×10^7 s^{-1}, and 1.3×10^8 s^{-1} for neat P3HT, 1.8% blend, and 50% blend, respectively. The increase in the first-order rate upon increasing PCBM loading is consistent with the blend morphological change, with more free charge carriers generated close to heterojunctions for trapping. Using time-resolved microwave conductivity (TRMC) spectroscopy, Ferguson *et al.* reported [32] a first-order decay rate of 4.9×10^7 s^{-1} that was attributed to trapping of mobile holes in P3HT that was independent of the PCBM concentration.

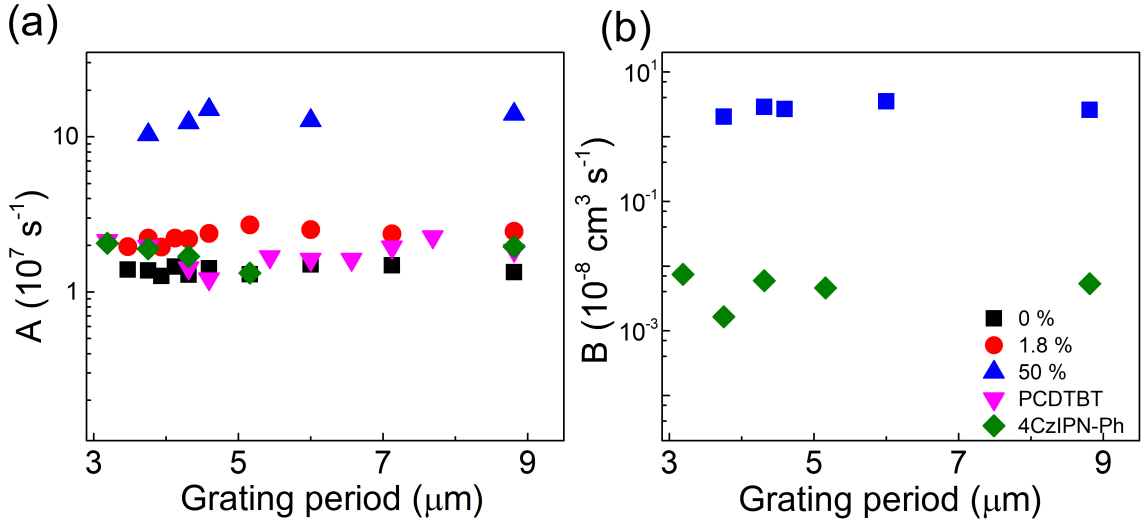

Figure 4.3: **The fitted carrier decay rates as a function of grating periods and blend weight ratios.** (a) first-order rates for neat P3HT, 1.8% and 50% P3HT:PCBM blends, neat PCDTBT, and 4CzIPN-Ph; (b) second-order rate for the 50% P3HT:PCBM blend and 4CzIPN-Ph. The fitting uncertainty of A is $\sim$ 5% for neat P3HT and 1.8% blend and $\sim$ 10% for 50% blend. The average fitting uncertainty of B is $\sim$ 10% for the 50% blend and $\sim$ 18% for 4CzIPN-Ph.

4.2.3 Other organic semiconducting materials

To generalize the applicability of the TG spectroscopy to other organic semiconducting materials, we also studied a neat film of poly[N-9"-hepta-decanyl-2,7-carbazole-alt-5,5-(4',7'-di-2-thienyl-2',1',3'-benzothiadiazole)] (PCDTBT), another typical donor material used in OPVs [114], and a film of 2,4,5,6-tetrakis(3,6-diphenylcarbazol-9-yl) isophthaloni-

trile (4CzIPN-Ph), a molecular fluorescent material used in organic light emitting devices [115]. The TG decay curves are presented in Figure 4.4 and are analyzed with the same process. The first-order decay rates A as a function of the grating period are given in Fig. 3(a). The first-order decay rate is 1.2×10^7 s^{-1} for PCDTBT and 1.7×10^7 s^{-1} for 4CzIPN-Ph, which are comparable with neat P3HT.

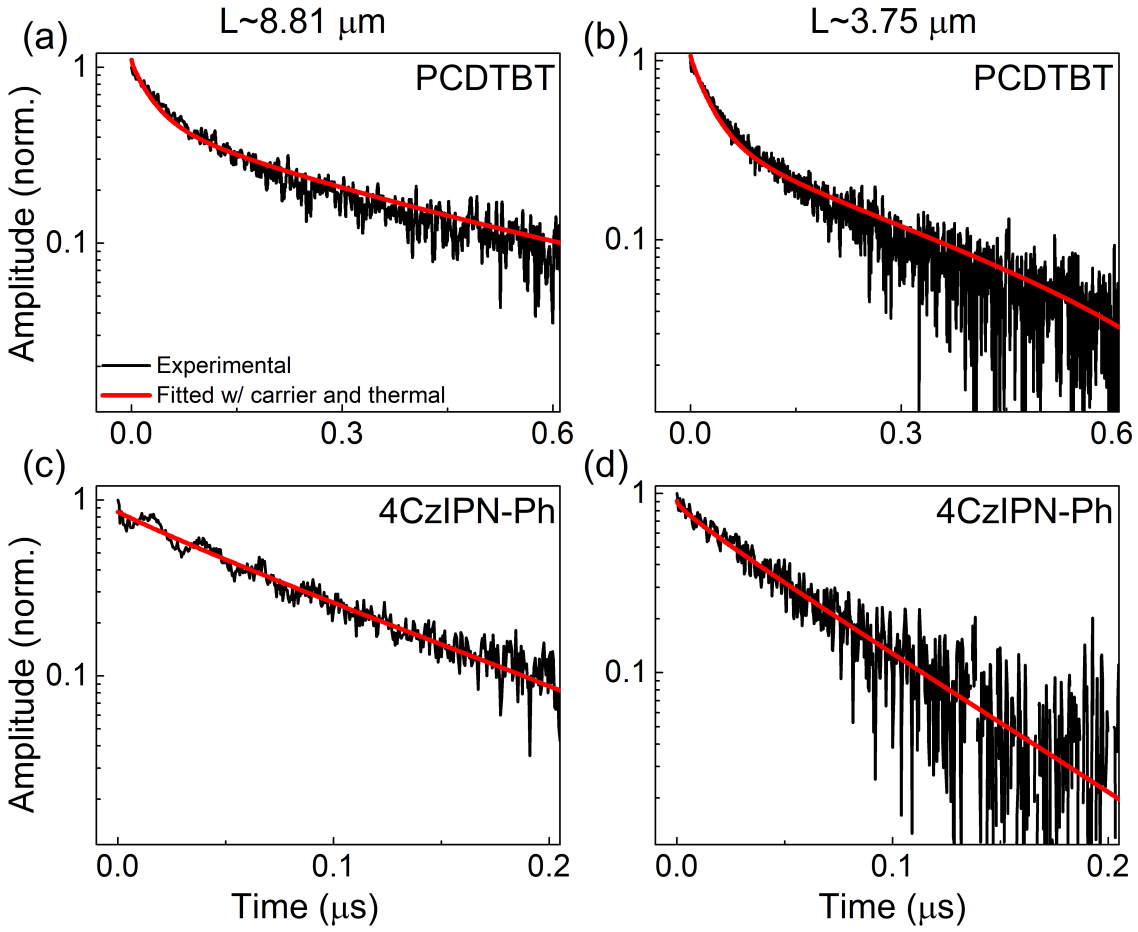

Figure 4.4: **The grating decays and fittings for PCDTBT and 4CzIPN-Ph.** The black curves are the two grating periods, 8.81 μm and 4.59 μm, respectively. The red lines are the fittings considering the carrier and thermal decays simultaneously.

The second-order recombination rate coefficient in the 50% P3HT:PCBM blends, as shown in Figure 4.3b, is 2.7×10^8 cm^3/s. There are several possible mechanisms for the observed second-order recombination process. The high concentration of free charge

carriers in the 50% blend can lead to more frequent annihilation processes between free charge carriers, whose recombination coefficients, however, are typically on the order of 10^{-12} cm^3/sin the P3HT:PCBM system due to the significantly suppressed Langevin prefactor, as measured by TRMC and transient absorption (TA) in annealed samples [32, 116, 117]. Other studies based on TRMC and TA [35, 31] have reported annihilation processes between excitons and free carriers with a second-order recombination coefficient on the order of 10^8 cm^3/s, but typically observed within a shorter time window (less than 1 ns) when a significant amount of excitons remain. In the time window of our TG measurement (tens to hundreds of ns), the exciton density is expected to be very low in the 50% blend, and thus the exciton-carrier recombination is unlikely to be responsible for the second-order process we observed. One possibility is the interaction between free charge carriers with the charge transfer states that extensively exist at the donor/ acceptor interfaces before dissociation into free charge carriers [118]. Although there has not been other direct experimental evidence for bimolecular recombination between free charge carriers and charge transfer states, multiscale simulations have indicated the coexistence of bound localized charge transfer states at the donor/acceptor interfaces with a high concentration of delocalized space-separated states[119]. Further studies are needed to confirm this hypothesis and will be part of our future pursuits. We also found an appreciable contribution from bimolecular recombinations in 4CzIPN-Ph, with a rate coefficient of $\sim 5 \times 10^{11}$ cm^3/s cm3/s, most likely due to free charge recombinations.

4.3 Conclusions

In summary, we demonstrated the capability of probing photocarrier dynamics and thermal transport simultaneously in a semiconducting polymer thin-film-on-substrate system.

Although thermal transport is dominated by the substrate, we were able to separate the contribution from the photocarrier dynamics in the organic thin films. Our study indicates that TG spectroscopy is a promising technique to simultaneously characterize charge carrier transport, recombination, and thermal transport in semiconducting polymers and other organic and hybrid optoelectronic materials, provided that thicker samples are used and/or submicrometer grating periods are achieved [51, 107].

Chapter 5

Extraordinary thermoelectric properties of topological surface states in quantum-confined Cd_3As_2 thin films

5.1 Introduction

Cd_3As_2 is an archetypal topological Dirac semimetal that exhibits a three-dimensional linear dispersion relation and topologically protected surface states [120, 121, 122, 123]. The linear dispersion relation and a large Fermi velocity give rise to an electron mobility as high as 20,000 cm^2/V-s at room temperature [59] in thin films grown by molecular beam epitaxy (MBE). In addition, Cd_3As_2 has a lattice thermal conductivity [124, 125, 126] around $0.3 \sim 0.7$ W/m-K at 300 K, which is anomalously low for single crystals. Using

first-principles lattice dynamics calculations, Yue *et al.*[64] uncovered the presence of a cluster of soft optical phonon modes in Cd_3As_2, which significantly enhance the scattering phase space of acoustic phonons leading to a low lattice thermal conductivity. The combination of a high electron mobility and a low thermal conductivity makes it a highly promising candidate for thermoelectric applications. However, as a topological Dirac semimetal, Cd_3As_2 has no bandgap in its bulk form, which is typically detrimental to the Seebeck coefficient. As a result, a moderate Seebeck coefficient ranging from 50 μV/K to 150 μV/K [127, 128, 126, 129, 130] was recorded experimentally in Cd_3As_2 bulk crystals.

To overcome this limitation, a bandgap can be opened in Cd_3As_2 through either crystal symmetry breaking or quantum confinement that can be realized in epitaxially grown thin films or heterostructures [121, 131, 132, 133, 134]. Specifically, it has been shown experimentally that in Cd_3As_2 thin films grown by MBE, a bulk band gap emerges below a certain film thickness due to quantum confinement, where the low temperature electrical transport properties are dominated by mobile carriers restricted to two-dimensional surface states [135]. The quantum confinement opens a bulk energy gap of Cd_3As_2 at the Dirac point and an open bandgap shows the potential for enhancing the Seebeck coefficient. Under the confinement, it has been noted that the presence of mobile carriers was restricted to two-dimensional surface states and there was no parastic conduction from the bulk states at low temperature. Therefore, it is imperative to consider the surface states contributions on the transport properties with confinement. Even though a bulk energy gap emerge, the surface states remains robust and Schumann *et al.* [135] observed quantized Hall effect in 25 nm Cd_3As_2 which was governed by carriers residing in surface states. Furthermore, Goyal *et al.* [136] studied the thickness dependence of quantum Hall effect in Cd_3As_2 thin films and concluded quantum Hall effect was observable in films thinner than 70 nm Cd_3As_2, indicating the significance of topological surface states

in such thin films.

The surface states in topological Dirac semimetal Cd_3As_2 consists of two sets of Fermi arcs [137] [except for the (001) surface where the projection of the bulk Dirac nodes becomes a point] that are capable of producing quantum oscillations and the quantum Hall effect [138, 139], which has been experimentally observed in MBE-grown films with a thickness below 70 nm [135, 136]. These surface states have been theoretically predicted to persist even in thin films with a few nm thickness [137]. Furthermore, the Dirac dispersion of surface states on (112) surfaces in MBE-grown Cd_3As_2 has been verified through gating experiments [140]. However, thermoelectric transport properties of these topological surface states are less explored and the impact of quantum confinement on thermoelectric properties has not been examined experimentally.

In this work, we systematically investigate the thermoelectric transport in high-quality Cd_3As_2 thin films grown by MBE. To resolve the contribution from different conducting channels, we studied samples with varying Cd_3As_2 thicknesses: 950 nm in the bulk limit, 95 nm in the transition regime, and 25 nm with quantum confinement and prominent contributions from the surface states. Surprisingly, we observed anomalously enhanced Seebeck and Nernst coefficients in the 25 nm sample at cryogenic temperatures. Combining extensive magneto-Seebeck and Nernst effect measurements, detailed angle-dependent quantum oscillation characterization, analytical transport models and first-principles density functional theory (DFT) simulations, we attribute the observed thermoelectric properties to the interplay of bulk and surface conducting channels in parallel. Our work provides a comprehensive understanding of thermoelectric transport in confined topological Dirac semimetal thin films and reveals the rich physics in these systems that can be potentially employed to engineer composite materials for thermoelectric applications.

5.2 Results and Discussion

5.2.1 Temperature dependence of resistivity and Seebeck coefficient

The MBE technique was employed to achieve the epitaxial growth of (112)-oriented Cd_3As_2 thin films on (111)-oriented GaAs substrates with a 150-nm (111) GaSb buffer layer [59], which forms a heterostructure with the Cd_3As_2 thin film. More details of the growth method and the measurement technique can be found in the Methods section and the Supporting Information. Figure 5.1a presents a schematic illustration of the sample structures studied in this work. In our experiment, three different thicknesses of Cd_3As_2 were prepared: 950 nm, 95 nm and 25 nm, with the same GaSb buffer layer and substrate conditions. We refer to them as "950-nm sample", "95-nm sample", and "25-nm sample", respectively, in the following discussion.

The measured electrical resistivity of the three samples as a function of temperature is shown in Figure 5.1b. The resistivity of the 950-nm sample exhibits a typical semimetallic behavior, where it increases with temperature. This behavior reflects the bulk Cd_3As_2 property. In contrast, the 95-nm sample shows a more pronounced semiconductor-like behavior with a decreasing resistivity with temperature. Low-field Hall results indicate n-type conduction that originates from the bulk Cd_3As_2 states. Therefore, the semiconductor-like behavior in the 95-nm sample suggests the onset of bulk bandgap opening due to quantum confinement, where the thermal activation of carriers results in a decrease in the resistivity with an increasing temperature [141, 128]. For the 25-nm sample, a modest variation in resistivity is noted with an increasing temperature, suggesting a delicate interplay between the semiconductor-like behavior of the bulk states and, potentially, the metallic surface states [141].

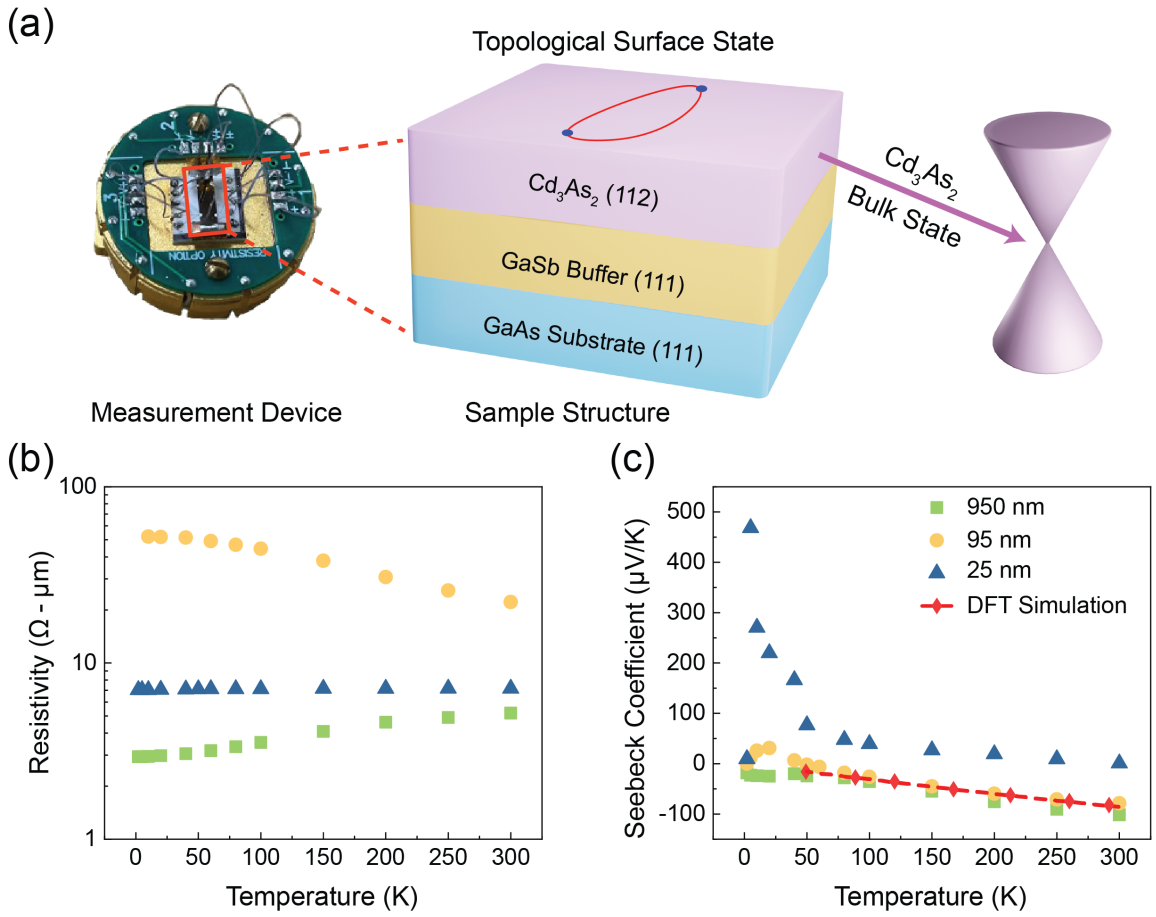

Figure 5.1: **Sample structures and temperature dependence of resistivity and Seebeck coefficient.** (a) Sample structure and potential conducting channels. (112) Cd_3As_2 samples with different thicknesses were epitaxially grown on a 150-nm (111) GaSb buffer layer on (111) GaAs substrates. Three potential conducting channels are illustrated here, including n-type Cd_3As_2 bulk states, p-type topological surface states and a p-type interfacial layer due to charge transfer between Cd_3As_2 and GaSb. (b) Temperature dependence of the measured resistivity of 950 nm, 95 nm and 25 nm Cd_3As_2 samples, respectively. (c) Temperature dependence of the measured Seebeck coefficients in the three samples, as compared to DFT calculation considering only Cd_3As_2 bulk states. Error bars are not shown here for clarify and are less than 10% for data shown here.

In Figure 5.1c, we present the temperature-dependent Seebeck coefficient for the three samples. Specifically, for the 950-nm sample, we observed an increase in the Seebeck coefficient with temperature, where the negative sign suggests the prevalence of n-type carriers [130, 128]. Meanwhile, for the 95-nm sample, the Seebeck coefficient exhibits a

similar temperature dependence above 50 K. In the temperature range above 50 K, the Seebeck coefficient of both samples can be well described by our DFT simulation using the bulk band structure of Cd_3As_2 assuming a Fermi level slightly into the conduction band (details of the DFT simulation are given in Methods). However, around 50 K, a change in the sign of the Seebeck coefficient occurs, suggesting a transition of the dominant carriers from n-type to p-type. At even lower temperatures, we also observed an increase of the positive Seebeck coefficient. Both features cannot be explained by our DFT simulation considering only the Cd_3As_2 bulk states. More interestingly, for the 25-nm sample, a positive Seebeck coefficient was observed in the entire temperature range, and the Seebeck coefficient showed a metallic feature with a negative temperature dependence above 50 K, contrary to the behavior observed in the other two samples. Strikingly, the Seebeck coefficient displayed a sharp increase below 50 K, peaked at 5 K with a value of nearly 500 μV/K. This surprising behavior was in sharp contrast to the other two samples with thicker Cd_3As_2 thin films. Furthermore, the distinct behaviors of the Seebeck coefficient in the three samples suggest the existence of contributions from more than one conducting channels in the thinner samples, thereby requiring further investigations as detailed in subsequent sections.

5.2.2 Angle-dependent quantum oscillations

In order to comprehensively investigate the underlying mechanisms responsible for the distinct thermoelectric behaviors of the three heterostructure samples with different Cd_3As_2 thicknesses, we performed systematic measurements of angle-dependent quantum oscillations in both the electrical resistivity (the Shubnikov-de-Haas, or SdH, oscillation) and the Seebeck coefficient of the three samples at 2 K. Quantum oscillations of electrical transport properties as a function of the magnetic field are manifestations of the Fermi

surface quantization, where the oscillation frequency as a function of the angle of the magnetic field can provide detailed information of the Fermi surface [142]. Figure 5.2a presents the Seebeck voltage oscillation of the three samples when the magnetic field is perpendicular to the sample surface ("0 degree" direction) at 2 K. The Seebeck voltage is plotted against the inverse magnetic field ($1/B$), from which the oscillation frequencies are obtained through a Fourier transform (FT). The three samples exhibit distinct oscillation frequencies, signaling different origins of the observed thermoelectric transport [143, 142, 144]. Specifically, for the 950-nm sample, a single prominent oscillation frequency is detected at approximately 20 T, as indicated by peaks A-B labeled in Figure 5.2a. The 95-nm sample shows two oscillation frequencies: one is around 20 T, also denoted by peaks A-B, while the other is around 55 T, corresponding to peaks C-D in Figure 5.2a. Similarly, the 25-nm sample also displays these two oscillation frequencies.

To further pinpoint the conducting channels corresponding to these quantum oscillation frequencies, we conducted a systematic investigation of the SdH and Seebeck coefficient quantum oscillation frequencies as a function of the angle of the applied magnetic field in all three samples. Figure 5.2b and Figure 5.2d show the results and a comparison of these results with the DFT calculation considering only the bulk Cd_3As_2 states. According to the Onsager relation [145], the oscillation frequencies F are proportional to extremal areas A of the Fermi surface perpendicular to the applied magnetic field, which is given by $F = \frac{\hbar}{2\pi e}A$, where $\hbar$ is the reduced Planck's constant and e is the electron charge.

Figure 5.2b illustrates the variation of the SdH oscillation frequency as a function of the magnetic field angle in 950-nm and 95-nm samples, respectively. The oscillation frequency is observed to undergo slight variations with angle in both samples, with the 950-nm sample exhibiting a concave shape centered around 90° and the 95-nm sample a convex shape. From Figure 5.2 5.2b, our DFT calculation predicts an oscillation frequency

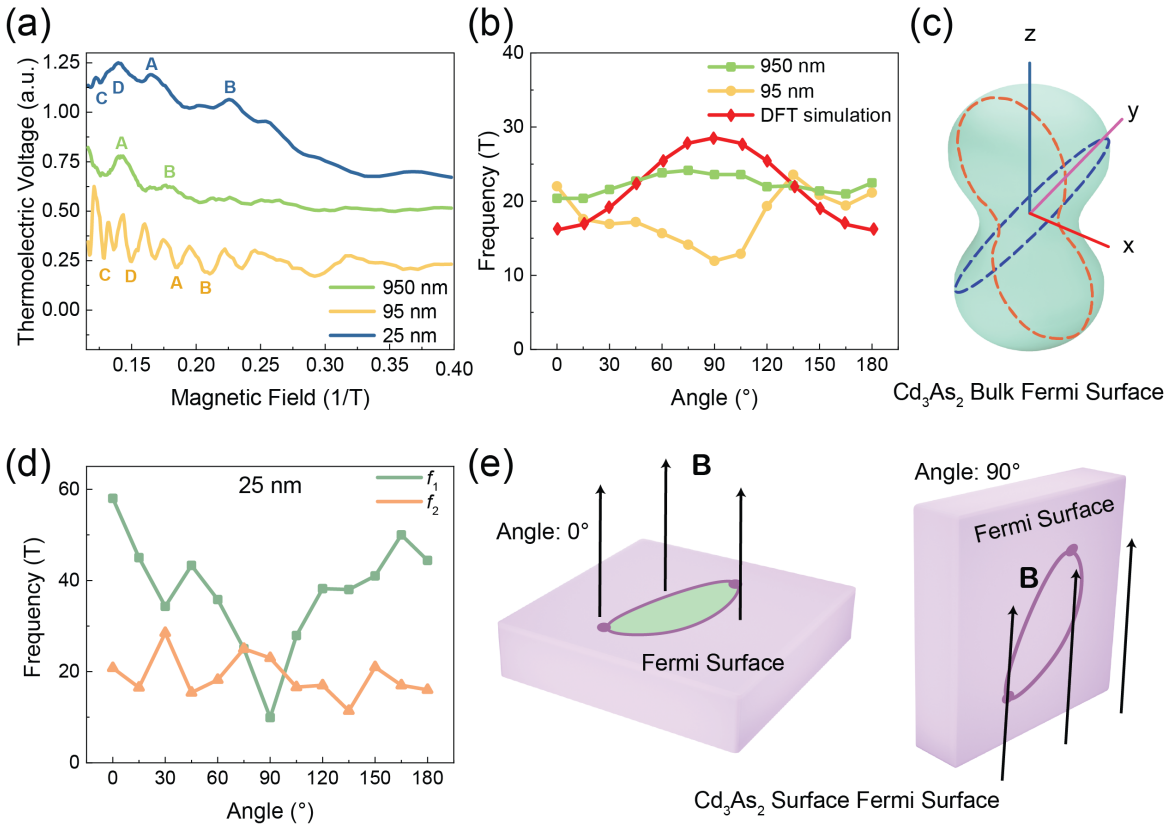

Figure 5.2: **Angle-dependent quantum oscillations.** (a) Measured thermoelectric voltage as a function of the inverse magnetic field for the three samples. Peaks A-B correspond to a 20 T oscillation frequency and peaks C-D, observed only in the 95 nm and 25 nm samples, correspond to a 55 T frequency. (b) Angular dependence of the quantum oscillation frequency in 950 nm and 95 nm samples. The oscillation frequency of these two samples is consistent with the DFT calculation considering Cd_3As_2 bulk states. (c) The Fermi surface of Cd_3As_2 bulk states responsible for the observed quantum oscillation frequency near 20 T. (d) Angular dependence of the quantum oscillation frequency in the 25-nm sample. The oscillation frequency of the 25-nm sample exhibits two distinct frequencies. The lower one near 20 T corresponds to the Cd_3As_2 bulk states. Additionally, there is a high-frequency peak near 55 T at 0 degree, which decreases with an increasing field angle, indicating its origin in the topological surface states. (e) Illustration of the angular dependence of the oscillation frequency corresponding to topological surface states. The Fermi surface of the surface states has the maximum intersection area with the magnetic field and the highest oscillation frequency at zero degree field angle, while a 90-degree field angle parallel to the sample surface leads to a vanishing oscillation frequency.

around 16 T at zero degree field angle, assuming bulk Cd_3As_2 states and a Fermi level $\sim$ 12 meV above the charge neutral point (CNP). The Fermi level position is deduced

from the Hall carrier concentration measurement of the 950-nm sample (see Supporting Information). Additionally, the DFT simulation also reproduces the concave trend shown in Figure 5.2b for the 950-nm sample. Specifically, at the predicted Fermi level position, a Lifshitz transition occurs and the two spherical Fermi surfaces surrounding the two Dirac points along the Γ-Z direction merge to form a peanut-shaped Fermi surface, as depicted in Figure 5.2c. This Fermi surface shape accounts for the concave trend observed in the 950-nm sample. The agreement between the 950-nm sample data and the DFT simulation further suggests that the thermoelectric transport in the 950-nm sample mainly arises from the n-type Cd_3As_2 bulk states.

Similarly, the 95-nm sample shows a SdH frequency at the zero-degree angle in agreement with the DFT calculation, indicating the contribution from the Cd_3As_2 bulk states. However, the angle-dependent trend observed in the 95-nm sample deviates from that in the 950-nm sample, which can be potentially attributed to the onset of the quantum confinement effect that can vary the shape of the Fermi surface as well as the position of the Fermi level. Unfortunately, in the 95-nm sample, the additional high-frequency SdH oscillation at 55 T is weak and we could not map its angle-dependence reliably.

For the 25-nm sample, it turned out difficult to obtain reliable angle-dependent SdH data with multiple oscillation frequencies. Instead, we found that the quantum oscillation observed in the Seebeck coefficient as a function of the magnetic field is much clearer and provides more reliable extraction of the oscillation frequencies. Therefore, we conducted systematic angle-dependent Seebeck oscillation measurements on the 25-nm sample and the results are shown in Figure 5.2d. One of the observed oscillation frequencies near 20 T is consistent with the bulk states of Cd_3As_2, as observed in the other two samples. In addition, the 25-nm sample exhibits another high oscillation frequency around 55 T at 0° field direction, which also appears in the 95-nm sample. The angle-dependent

reduction in this oscillation frequency culminating at 90° field direction implies that this frequency is associated with two-dimensional (2D) surface states, since the Fermi surface associated with the 2D surface states has zero intersection with the magnetic field at 90° field direction, as illustrated in Figure 5.2e. Based on this observation, the behavior of the Seebeck coefficient of the 95-nm sample shown in Figure 5.2c can be understood. Above 50 K, the main contribution to the Seebeck coefficient in the 95-nm sample comes from the bulk Cd_3As_2 states, similarly as the 950-nm sample. Below 50 K, the bulk states in the 95-nm sample start to freeze out due to the onset of quantum confinement, while the contribution from the surface states emerges and is responsible for the sign change of the Seebeck coefficient. This view is also consistent with the p-type character of the surface states observed in previous measurements of Cd_3As_2 thin films [141]. In contrast, the Seebeck coefficient of the 25-nm sample is positive throughout the entire temperature range, suggesting that the bulk Cd_3As_2 states, presumably n-type, play a minor role in thermoelectric transport even up to 300 K. However, the surface-state contribution alone is not expected to give rise to the large Seebeck peak near 5 K in the 25-nm sample. We hypothesize that this large Seebeck peak has contributions from both the surface states and potentially an interfacial conducting layer formed at the Cd_3As_2/GaSb interface. In the following, we provide detailed magnetothermoelectric transport measurements and model analysis to examine this hypothesis.

5.2.3 Magneto-transport measurements and modeling

We conducted magneto-electrical transport measurements to determine the longitudinal and Hall resistivity of the three Cd_3As_2 samples. The obtained results are shown in Figure 5.3. As for 950 nm and 95 nm Cd_3As_2 samples, the electrical measurements were carried out under a magnetic field strength up to 1 T only to exact the low-field transport

properties, while the 25 nm Cd_3As_2 sample was subjected to a magnetic field strength up to 9 T. The determination of carrier type was based on the slope of the low-field Hall resistivity. The low-field Hall resistivity reveals that both the 950 nm and 95 nm samples have dominant n-type carriers, which are consistent with the results obtained from our Seebeck measurements. In the case of the 25 nm Cd_3As_2 sample, the change of the Hall resistivity slope at higher magnetic field indicates the existence of both n-type and p-type carriers. The negative slope at small magnetic field signals that the n-type carriers have a higher mobility, while the positive slope at higher magnetic field suggests the p-type carriers have a higher density. Furthermore, the dissimilar shapes observed in the longitudinal and transverse resistivity emphasize distinct transport characteristics, requiring the adoption of different models for their respective fitting analyses.

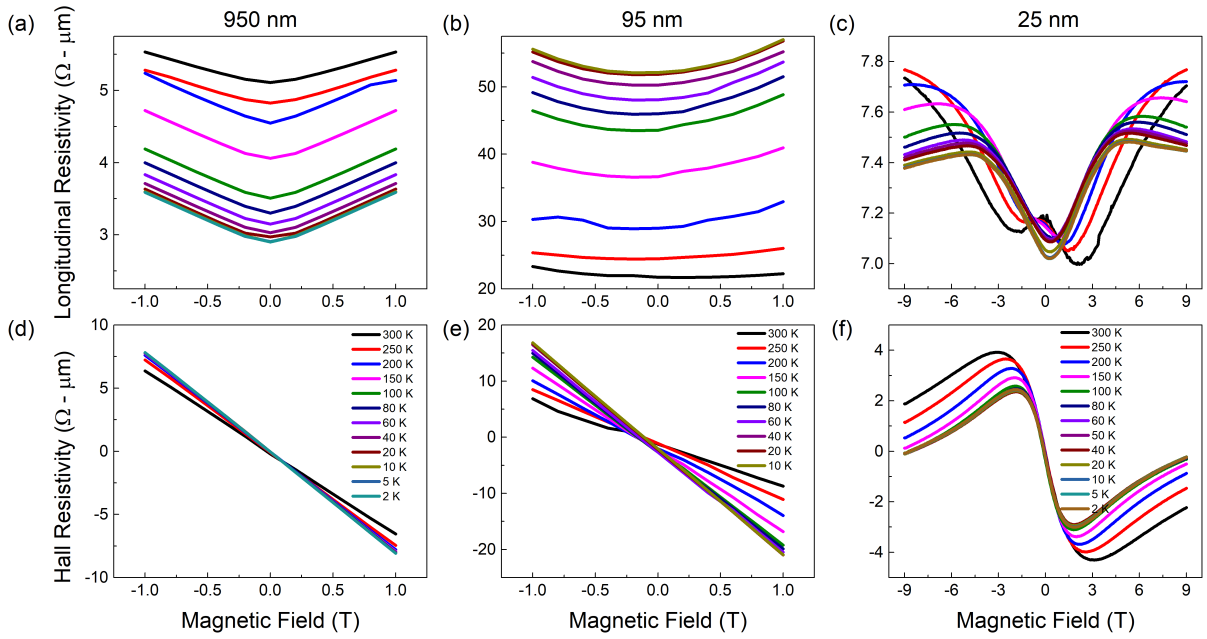

Figure 5.3: **Field dependence of longitudinal resistivity and Hall resistivity measured at different temperatures.** (a-c) The longitudinal resistivity of 950 nm, 95 nm and 25 nm Cd_3As_2, respectively. (d-f) The Hall resistivity of the three samples.

Based on the quantum oscillation analysis, it is established that the dominant carrier in the 950 nm Cd_3As_2 sample corresponds to the n-type bulk states, whereas in the 25 nm Cd_3As_2 sample, two groups of carriers associated with bulk states and topological surface states contribute to the transport properties. This interpretation is also supported by the Hall resistivity measurements shown in Figure 5.4. Specifically, in the 950 nm sample, the Hall resistivity exhibits a linear response with an increasing magnetic field, while in the 25 nm sample, it follows a nonlinear trend, indicating the contributions from two carriers. Consequently, we construct a one-band and a two-band Drude model to describe transport in the 950 nm and the 25 nm samples, respectively. For the 950 nm Cd_3As_2 sample, its resistivity tensor $\rho = \begin{pmatrix} \rho_{xx} & -\rho_{yx} \\ \rho_{yx} & \rho_{yy} \end{pmatrix}$ is described by $\rho_{xx} = \rho_{yy} = 1/(n_e e \mu_e)$ and $\rho_{yx} = B/(n_e e)$ where e is the elementary charge, n_e is the carrier density of the bulk states, and μ_e is the mobility of the bulk states [146]. The fitted carrier concentration and mobility in the 950 nm sample at different temperatures is shown in Figure 5.4.

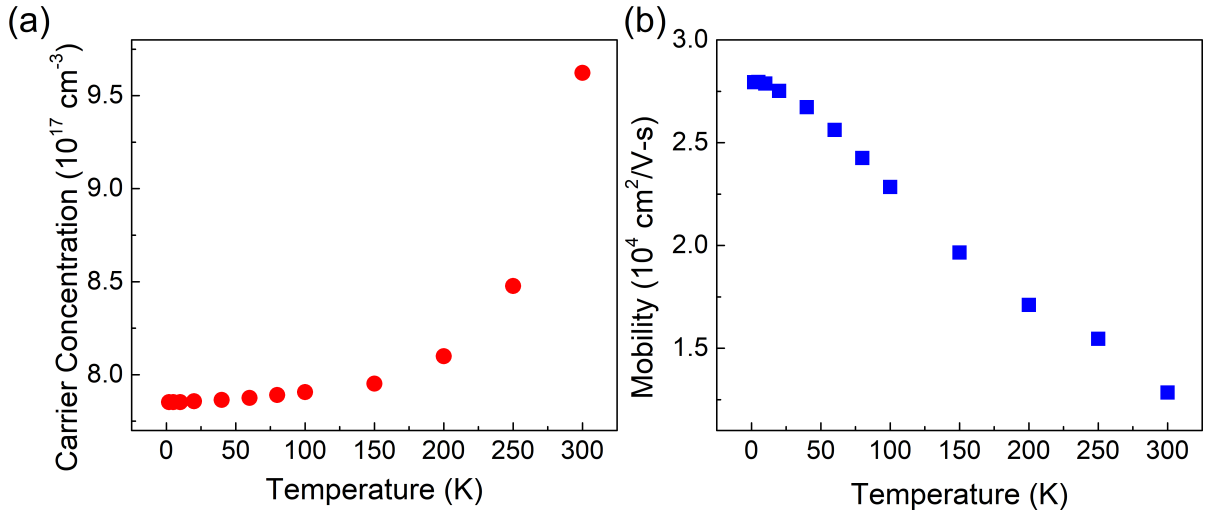

Figure 5.4: **Carrier concentration and mobility in the 950 nm sample extracted from the Hall resistivity measurement.** (a) The fitted carrier concentration in the 950 nm sample at different temperatures. (b) The fitted carrier mobility in the 950 nm sample at different temperatures.

For the 25 nm Cd_3As_2 sample, the resistivity tensor is described by contributions from the surface carriers (labeled by subscript s) and the bulk carrier (labeled by subscript b), whose longitudinal resistivity and Hall coefficient are denoted by $\rho_{s/b}$ and $R_{s/b}$, respectively:

$$\begin{aligned} \rho_{xx} &= \frac{\rho_s\rho_b(\rho_s+\rho_b)+(\rho_s R_b^2+\rho_b R_s^2)B^2}{(\rho_s+\rho_b)^2+(R_s+R_b)^2B^2}, \\ \rho_{yx} &= \frac{(R_s\rho_b^2+R_b\rho_s^2)B+R_sR_b(R_s+R_b)B^3}{(\rho_s+\rho_b)^2+(R_s+R_b)^2B^2}. \end{aligned}$$

The parameters obtained from the transverse resistivity ρ_{yx} for the two carriers often fail to accurately replicate the longitudinal resistivity ρ_{xx} due to the absence of consideration for the magnetic-field dependence of the relaxation time in the model [147]. However, we can impose constraints on our fitting by verifying the consistency of ρ_{xx} at zero magnetic field.

Based on the quantum oscillation analysis, we have established that the thermoelectric transport in the 950-nm sample is dominated by the n-type bulk Cd_3As_2 states, while the additional contribution from the surface states plays a role below 50 K in the 95-nm sample. In the 25-nm sample, the contribution from the surface states is significant even up to 300 K. To further verify and quantify our interpretation, we discuss detailed magnetotransport measurements, including Hall, Seebeck and Nernst coefficients, and the associated transport models in this section. We focus on analyzing the 25-nm sample here. All measurements discussed in this section were done with a magnetic field perpendicular to the sample surface.

Firstly, the magnetoresistance and the Hall resistivity data of the 25 nm sample exhibit a typical two-carrier behavior with contributions from two groups of carriers with opposite charges. In particular, a group of higher-mobility n-type carriers dominates the

small-field Hall resistivity, while a group of higher-density p-type carriers dominate the large-field Hall resistivity. To simultaneously incorporate the magnetoresistance and the Hall resistivity, we used a two-band Drude model to fit the Hall resistivity ρ_{xy} data as a function of temperature and magnetic field, as shown in Figure 5.5a, where we presented results at three representative temperatures. The semiclassical Drude model is valid for low magnetic fields before quantum oscillations appear, so we focused on analyzing the magnetotransport data below 4 T. We used the carrier concentration and the carrier mobility of both groups of carriers as the fitting parameters here. To increase the fitting sensitivity, we used the same group of parameters to simultaneously fit the low-field ($<$ 1 T) data of the longitudinal resistivity. As shown in Figure 5.5a, the two-band Drude model fits the experimental data satisfactorily. The fitted mobilities and concentrations for the electron and hole conduction channels are shown in Figure 5.5b and c. As expected, the Hall data can be explained by a high-mobility, low-density electron channel representing the bulk Cd_3As_2 states and a low-mobility, high-density hole channel that can be attributed to the surface states [141]. The low concentration of the n-type Cd_3As_2 bulk states suggests a strong quantum confinement. The high density of the surface state carriers is in qualitative agreement with the observed high-frequency quantum oscillation as well as previous reports on similar samples [141].

Figure 5.6 shows the magnetic-field-dependent Seebeck coefficient S_{xx} and Nernst coefficient S_{xy} in the 25-nm sample measured at different temperatures in a magnetic field up to 9 T. In the semiclassical regime, the Seebeck coefficient and the Nernst coefficient can be calculated as [148]:

$$S_{xx}(B) = A\left(\frac{\sigma_{xx}^2}{\sigma_{xx}^2+\sigma_{xy}^2}D + \frac{\sigma_{xy}^2}{\sigma_{xx}^2+\sigma_{xy}^2}D_H\right), \tag{5.1}$$

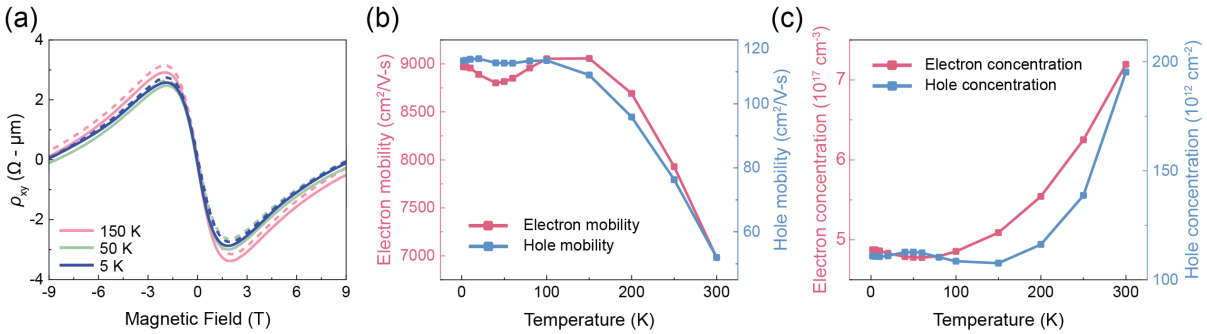

Figure 5.5: **Magnetic-field-dependent Hall measurements of the 25-nm sample.** (a) Measured Hall resistivity (solid lines) of the 25-nm sample fitted by a two-band Drude model (dashed lines) at three representative temperatures. (b) Fitted mobilities of the electron and hole conducting channels, indicating a highly mobile n-type channel and a low-mobility p-type channel. (c) Fitted carrier concentrations of the n-type bulk states and the p-type surface states.

$$S_{xy}(B) = A\frac{\sigma_{xx}\sigma_{xy}}{\sigma_{xx}^2 + \sigma_{xy}^2}(D_H - D), \tag{5.2}$$

where $A = \frac{\pi^2 k_B^2 T}{3e}$, and σ_{xx} and σ_{xy} are longitudinal and Hall conductivity, respectively. Additional parameters D and D_H are from the Mott relations: $D = \frac{\partial \ln \sigma_{xx}}{\partial \zeta}$, $D_H = \frac{\partial \ln \sigma_{xy}}{\partial \zeta}$, where ζ is the Fermi level. As shown in Figure 5.6a, the measured Seebeck coefficient follows the semiclassical increase and saturation trend with the magnetic field in a semimetal [130]. In Figure 5.6b, we used the two-band semiclassical model (Eqn. 5.1) with parameters extracted from the Hall resistivity fitting (Figure 5.5) to fit the low-field ($< 1\,\mathrm{T}$) Seebeck data [148]. For consistency, we also used the experimental σ_{xx} and σ_{xy} data and the fitting parameters D and D_H to fit the low-field Seebeck data, where similar values of D and D_H are obtained (see Supplementary Note X in the SI). The fitted values of D and D_H are provided in Figure 5.6c. The extracted D and D_H values steeply rise as the temperature decreases, reaching $> 1000\,\mathrm{eV}^{-1}$, suggesting unusually sharp changes of σ_{xx} as a function of the Fermi level. At cryogenic temperatures where the electronic scattering rates are largely independent of the Fermi level, the sharp changes of σ_{xx} most likely stem from the large effective mass and, thus, large density of states of the p-type

carriers residing in the surface states. This interpretation is consistent with the Hall resistivity data and in agreement with previous Landau level spectroscopy analysis of similar samples [140].

The unusual thermoelectric properties of the topological surface states are further manifested in the Nernst coefficient of the 25 nm sample, as shown in Figure 5.6d-f, where we provide the measured Nernst coefficient up to 9 T and the semiclassical (Eqn. 5.2) prediction for the low-field Nernst data with parameters extracted from fitting the low-field Seebeck data. The low-field Nernst coefficient above 40 K can be reasonably explained using the semiclassical model (Figure 5.6e). Below 40 K, as shown in Figure 5.6f, however, there is significant discrepancy between the experimental values and the model predictions, suggesting the failure of the semiclassical model. For comparison, the Nernst coefficient measured in our 950 nm sample at cryogenic temperatures is in good agreement with previous measurements of bulk Cd_3As_2 crystals [130], where the anomalous Nernst effect (ANE) contribution due to the Berry curvature of bulk Cd_3As_2 states is considered. The Nernst coefficient in the 95 nm sample is slightly increased from that in the 950 nm sample, while the Nernst coefficient in the 25 nm sample is about one order of magnitude higher than that in the 950 nm sample. This experimental trend signals a significantly enhanced ANE associated with the topological surface states in the 25 nm sample. Due to the still scarce understanding of the Fermi arc surface states in Cd_3As_2 thin films [137], it is difficult to quantitatively verify the large ANE associated with them from a modeling point of view. One potential explanation is that the surface states are gapped in the 25 nm sample due to hybridization of the top and bottom surfaces and/or strain [137], which can lead to a large Berry curvature [149, 150] that contributes to an enhanced ANE. Our result exemplifies the complexity of thermoelectric transport in the quantum-confined thin films of topological semimetals and suggests a new route to

achieving large thermoelectric responses at cryogenic temperatures via topological surface states.

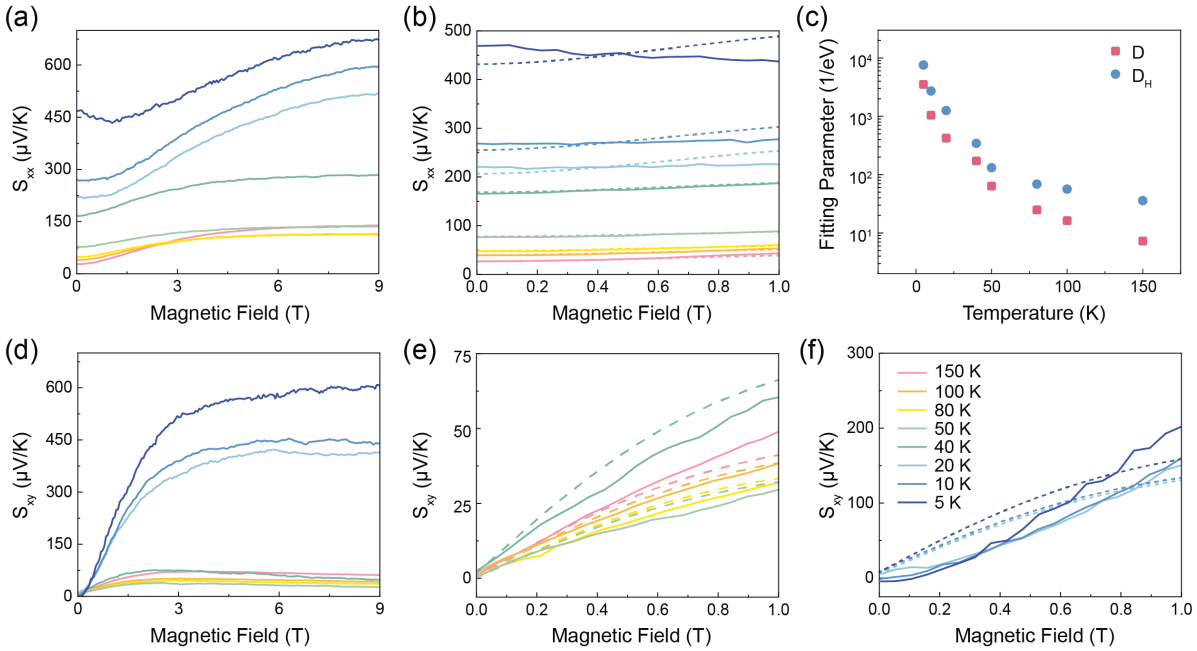

Figure 5.6: **Magnetic-field-dependent Seebeck and Nernst measurements of the 25-nm sample.** (a) Measured Seebeck coefficient of the 25-nm sample at different temperatures with a magnetic field up to 9 T. (b) Low-field Seebeck data (solid lines) fitted by a two-band semiclassical model (dashed lines). (c) The fitted Mott relation parameters D and D_H as a function of temperature. (d) Measured Nernst coefficient of the 25-nm sample at different temperatures with a magnetic field up to 9 T. (e) Low-field Nernst data (solid lines) fitted by a two-band semiclassical model (dashed lines) above 40 K, where reasonable agreement between experiment and model is observed. (e) Measured Nernst coefficient (solid lines) of the 25-nm sample fitted by a two-band model (dashed lines) below 20 K, where large deviation between experiment and model potentially due to an enhanced anomalous Nernst contribution from the topological surface states is observed.

In passing, we briefly discuss the possible contribution to the measured thermoelectric response from the GaSb buffer layer, which is a semiconductor and can potentially possess a high Seebeck coefficient. Measurements of a bare GaSb buffer layer are provided in the SI, where it is shown that GaSb becomes insulating below 50 K. In principle, however, the band alignment between GaSb and Cd_3As_2 at the interface can lead to charge transfer and "doping" of GaSb, increasing its conductivity. However, in extensive previous studies

of this system down to very thin Cd_3As_2 layers, there is no experimental evidence that the GaSb buffer layer affects transport measurements in any way, especially at cryogenic temperatures [135, 140, 141, 151]. Moreover, the charge carriers in GaSb do not carry any nontrivial Berry curvature and, thus, are not expected to lead to any contribution to the observed ANE. On the basis of these observations, we attribute the observed unusual thermoelectric properties to the topological surface states, rather than the GaSb buffer layer.

5.3 DFT Calculations

This section was conducted together with Yubi Chen. We employed the Vienna ab initio simulation package VASP [152, 153] version 6.3.1. for DFT-based first principles calculations. The projector augmented wave (PAW) [154] potentials were utilized. The valence electrons for Cd included $5s^2 3d^{10}$, while for As they were $4s^2 3p^3$ electrons. The Perdew-Burke-Ernzerhof (PBE) [155] exchange correlation functional was adopted, including the spin-orbit coupling. The cutoff energy for the plane-wave expansion was 400 eV. The lattice structure was optimized with a Hellmann-Feynman force tolerance of 0.001 eV/Å. The Monkhorst-Pack $6 \times 6 \times 6$ k-mesh to sample the whole Brillouin zone was critical to obtain the correct Fermi level. This k mesh has a k-point ($\frac{1}{12}$, $\frac{1}{12}$, -$\frac{1}{12}$) close to the Dirac point located at ($\frac{1}{12.5}$, $\frac{1}{12.5}$, -$\frac{1}{12.5}$) in the 80-atom primitive-cell reciprocal lattice basis or at (0, 0, $\pm$0.0386 $Å^{-1}$)=(0,0, $\pm\frac{1}{6.25}\frac{2\pi}{c}$) in the conventional-cell reciprocal lattice, close to the previous reports [156, 157, 120, 158]. The symmetry of Cd_3As_2 is $I4_1/acd$ and fully exploited to minimize the computational expense. The relaxed lattice constants of the conventional cell are a=b=12.850Å, c=25.905Å. The calculated electronic structure is shown in the Figure 5.7 using the 80-atom primitive cell.

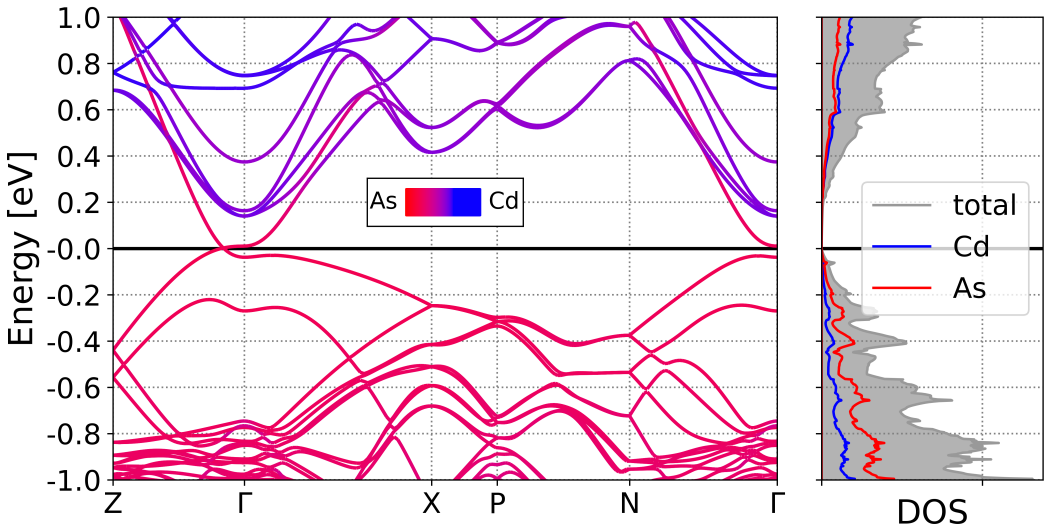

Figure 5.7: **Cd_3As_2 electron band structure and density of states (DOS)**. The variations in color indicate the atomic character of the electron states, as represented on the associated color bar. The energy reference is the Dirac crossing point.

In addition, we compared the experimental angle-dependent quantum oscillation frequencies with DFT calculations. With the Fourier interpolated Fermi surfaces on a $\Gamma - 65 \times 65 \times 83$ **k**-point gird, we used the SKEAF package [159] to divide the Fermi surfaces into slices perpendicular to the external magnetic field and obtain the slices with local maximum or minimum areas, from which the quantum oscillation frequencies can be calculated using the Onsager relation. To evaluate the transport properties, we apply the BoltzTraP2 [160, 161] software, which allows for the calculation of transport properties by solving the linearized Boltzmann equation under the constant relaxation time approximation. Of the various physical observables considered, the Hall carrier concentration in Figure 5.8a and the Seebeck coefficient (shown in Figure 5.1c in the Main Text, Figure 5.8b, and Figure 5.9) are independent from the choice of the relaxation time, and they are estimated with respect to the Fermi level position at different temperatures. The Cd_3As_2 energy surfaces are obtained from a non-self-consistent calcu-

lation on a Γ-12 × 12 × 12 **k**-point grid and subsequently Fourier interpolated [161] onto a dense Γ-65 × 65 × 83 **k**-point grid. The dense **k**-point grid is also necessary to ensure the convergence of the Seebeck and Hall concentration calculation.

The experimental Hall measurement of the 950 nm sample resulted in a Hall concentration of approximately 7.9×10^{17} cm^{-3} at low temperatures in Figure 5.4a, which corresponds to a Fermi level near 18 meV above the charge neutrality point from our DFT simulation in Figure 5.8a. In Figure 5.8a, the experimental Seebeck coefficient of the 950 nm sample is around $-50\mu V/K$, close to the Seebeck coefficients at the 18 meV Fermi level pinned by the Hall measurement. Our findings demonstrate that the predominant thermoelectric transport in the 950 nm sample stems from the bulk states, as confirmed by the consistency of our DFT calculations with the experimental results.

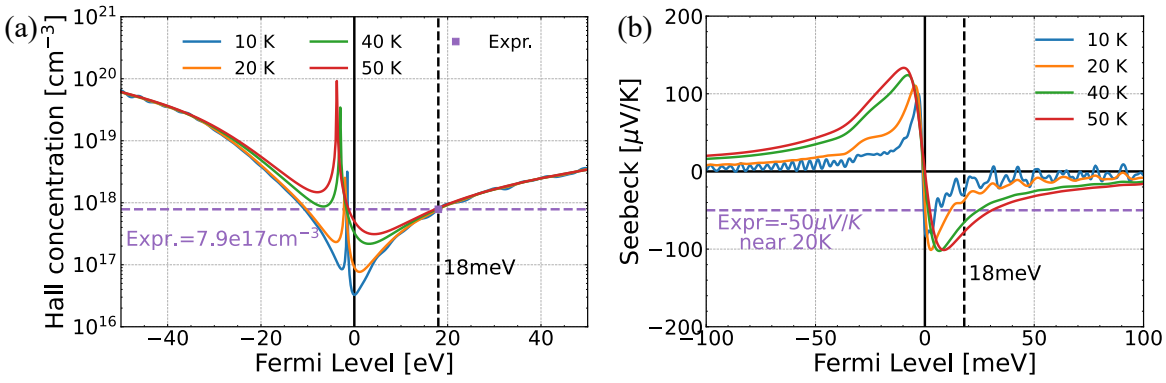

Figure 5.8: The calculated (a) Hall concentration and (b) Seebeck coefficients in bulk Cd_3As_2 as a function of Fermi level under low temperatures (10 K, 20 K, 40 K, and 50 K). The purple dashed line indicates the experimental values at low T. The Hall concentration and Seebeck coefficient can be nearly matched with the same Fermi level at 18 meV.

For the thermoelectric transport simulation, the Mott formula [146] is used to numerically evaluate the Seebeck coefficient in Figure 5.8b and Figure 5.9. In Figure 5.9b, the low temperature experimental Seebeck coefficient almost shares the same Fermi level as Hall concentration in Figure 5.8. As for the high temperature Seebeck coefficient (above 50 K),

the trend is well captured by n-type doping concentration 8×10^{18} cm^{-3}. We estimated the experimental Seebeck coefficient of the 950 nm sample with many different n-type carrier concentrations. The numerical determination of the Fermi level at various temperatures and carrier concentrations is achieved through the utilization of the charge neutrality equation, which then enables the corresponding Seebeck coefficient to be extracted with respect to the obtained Fermi level.

The resulting Seebeck data in Figure 5.9 with n-type 8×10^{18} cm^{-3} carrier concentration at higher temperatures is found to exhibit the best agreement with the 950 nm experimental results, although the carrier concentration in the 950 nm sample extracted from the Hall resistivity measurement is around 7.9×10^{17} cm^{-3}. This discrepancy can be attributed to the limited accuracy of the rigid band approximation where the DFT electronic structure is assumed to stay invariant for finite temperatures. Besides, for a complex material like Cd_3As_2 with a 80-atom unit cell, the computational cost limits the exploration for finite-temperature simulations, and more accurate exchange correlation functionals. As a result, the low temperature Seebeck coefficients are well captured by the almost undoped 1×10^{16} cm^{-3}, and the high temperature Seebeck coefficients can be well approximated by the 8×10^{18} cm^{-3} n-type doping concentration.

5.4 Conclusions

In summary, we systematically studied the thermoelectric transport properties of epitaxially grown Cd_3As_2 thin films with different thicknesses. Through detailed quantum oscillation analysis and magnetotransport measurement complemented by DFT simulation and a two-band Drude transport model, we identified contributions from both bulk states and topological surface states. In particular, we revealed unusually large Seebeck

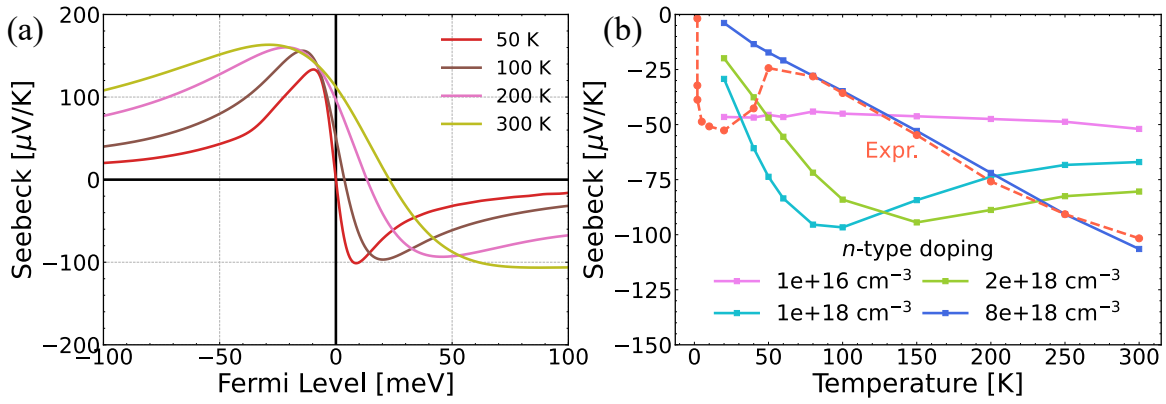

Figure 5.9: (a) The calculated Seebeck coefficient across Fermi level at higher temperatures (50 K, 100 K, 200 K, 300 K). (b) The calculated Seebeck coefficient of bulk Cd_3As_2 with different n-type carrier concentrations and temperatures.

and Nernst effect associated with the topological surface states. Our results showcase the complexity of thermoelectric transport in topological semimetal thin films and signal new opportunities to achieve remarkable thermoelectric performances in these emerging material systems.

Chapter 6

Summary and Outlook

In this thesis, we investigated the characterization of nanoscale carrier transport within silicon, organic P3HT and PCBM heterojunctions, and topological Dirac semimetal thin films. Through a combination of computational and experimental methodologies, we interpreted the observed microscopic transport phenomena inside these materials promising for renewable energy applications.

The investigation into photogenerated charge carrier transport within SUEM has been instrumental in various applications including photovoltaics and optoelectronics. Through a meticulous integration of Monte Carlo simulations and TDDFT, this work has unveiled the image mechanisms of SUEM. In detail, the impact of photoexcitation on secondary electron emissions of silicon is studied, particularly in two effects: bulk carrier effects and surface effects. We observed that the prompt hot carrier effect subsequent to photoexcitation exerts a substantial influence on the SEY, whereas the mere presence of cooled-down bulk photocarriers brings about a marginal alteration in SEY. Chapter 3 has examined the prevalence of the hot carrier effect immediately following photoex-

citation, with the surface effect gaining prominence as thermal equilibrium is reached. Nonetheless, a quantitative exploration of time-resolved SEY subsequent to photoexcitation has been absent. Investigating carrier dynamics in real time holds the potential to enhance our grasp of SUEM image contrasts and foster a deeper comprehension of its applications. This avenue presents a promising trajectory for future research endeavors.

In Chapter 4, we introduced TG techniques to simultaneously investigate photocarrier dynamics and thermal transport within the P3HT/PCBM system. While thermal transport is primarily dictated by the substrate, our research effectively untangled the influence stemming from photocarrier dynamics in the organic thin films. This inquiry highlights the potential of TG spectroscopy as a promising approach for the concurrent assessment of charge carrier transport, recombination phenomena, and thermal properties in semiconducting polymers and other organic or hybrid optoelectronic materials. Notably, in our current investigation, the P3HT thin film functions as an absorption layer; however, the exploration of thicker polymer thin films could serve as a productive avenue for future studies. Demonstration of simultaneous measurement of thermal and photocarrier transport properties in the same organic semiconductor thin film remains a challenge and can be a promising future direction for transient grating spectroscopy.

In Chapter 5, our investigation meticulously explored the thermoelectric transport characteristics within epitaxially grown Cd_3As_2/GaSb heterostructures, varying the thickness of Cd_3As_2 layer. By employing a comprehensive approach involving quantum oscillation analysis, magnetotransport measurements, and augmented by DFT simulations and a two-band Drude transport model, we successfully delineated distinct transport channels contributing to the thermoelectric transport. This study unveiled a dual-contributory mechanism, originating from both bulk states and the distinctive topological surface states. Remarkably, our findings disclosed an exceptional enhancement of Seebeck and

Nernst effects uniquely associated with these topological surface states. Furthermore, the distinctive Berry curvature inherent to such topological materials, coupled with the configurations of our measurement setups, serves as a catalyst for further investigation into anomalous effects. This prompts us to consider the potential exploration of phenomena like transverse thermal Hall measurements, opening avenues for the future exploration and refinement of these measurement techniques.

Bibliography

[1] G. M. Wilson, M. Al-Jassim, W. K. Metzger, S. W. Glunz, P. Verlinden, G. Xiong, L. M. Mansfield, B. J. Stanbery, K. Zhu, Y. Yan, and et al., *The 2020 photovoltaic technologies roadmap*, *Journal of Physics D: Applied Physics* **53** (2020) 493001.

[2] J. Y. Kim, J.-W. Lee, H. S. Jung, H. Shin, and N.-G. Park, *High-efficiency perovskite solar cells*, *Chemical Reviews* **120** (2020), no. 15 7867–7918.

[3] Z. Guo, Y. Wan, M. Yang, J. Snaider, K. Zhu, and L. Huang, *Long-range hot-carrier transport in hybrid perovskites visualized by ultrafast microscopy*, *Science* **356** (2017), no. 6333 59–62.

[4] D. König, K. Casalenuovo, Y. Takeda, G. Conibeer, J. Guillemoles, R. Patterson, L. Huang, and M. Green, *Hot carrier solar cells: Principles, materials and design*, *Physica E: Low-dimensional Systems and Nanostructures* **42** (2010), no. 10 2862–2866.

[5] S. Tanuma, C. J. Powell, and D. R. Penn, *Calculations of electorn inelastic mean free paths. ii. data for 27 elements over the 50–2000 ev range*, *Surface and Interface Analysis* **17** (1991), no. 13 911–926.

[6] D. Fujita, M. Schleberger, and S. Tougaard, *Extraction of depth distributions of electron-excited auger electrons in fe, ni and si using inelastic peak shape analysis*, *Surface science* **357** (1996) 180–185.

[7] J. Shi, Y. Li, Y. Li, D. Li, Y. Luo, H. Wu, and Q. Meng, *From ultrafast to ultraslow: charge-carrier dynamics of perovskite solar cells*, *Joule* **2** (2018), no. 5 879–901.

[8] F. Doany and D. Grischkowsky, *Measurement of ultrafast hot-carrier relaxation in silicon by thin-film-enhanced, time-resolved reflectivity*, *Applied Physics Letters* **52** (1988), no. 1 36–38.

[9] M. Maiuri, M. Garavelli, and G. Cerullo, *Ultrafast spectroscopy: State of the art and open challenges*, *Journal of the American Chemical Society* **142** (2019), no. 1 3–15.

[10] G. Mourou and S. Williamson, *Picosecond electron diffraction*, *Applied Physics Letters* **41** (1982), no. 1 44–45.

[11] B. J. Siwick, J. R. Dwyer, R. E. Jordan, and R. J. D. Miller, *An atomic-level view of melting using femtosecond electron diffraction*, *Science* **302** (2003) 1382–1385.

[12] W. E. King, G. H. Campbell, A. Frank, B. Reed, J. F. Schmerge, B. J. Siwick, B. C. Stuart, and P. M. Weber, *Ultrafast electron microscopy in materials science, biology, and chemistry*, *Journal of Applied Physics* **97** (2005) 111101.

[13] A. H. Zewail, *Four-dimensional electron microscopy*, *Science* **328** (2010), no. 5975 187–193.

[14] A. Sood, X. Shen, Y. Shi, S. Kumar, S. J. Park, M. Zajac, Y. Sun, L.-Q. Chen, S. Ramanathan, X. Wang, *et. al.*, *Universal phase dynamics in VO_2 switches revealed by ultrafast operando diffraction*, *Science* **373** (2021), no. 6552 352–355.

[15] D.-S. Yang, O. F. Mohammed, and A. H. Zewail, *Scanning ultrafast electron microscopy*, *Proceedings of the National Academy of Sciences* **107** (2010) 14993–14998.

[16] O. F. Mohammed, D.-S. Yang, S. K. Pal, and A. H. Zewail, *4D scanning ultrafast electron microscopy: visualization of materials surface dynamics*, *Journal of the American Chemical Society* **133** (2011), no. 20 7708–7711.

[17] B. Liao and E. Najafi, *Scanning ultrafast electron microscopy: A novel technique to probe photocarrier dynamics with high spatial and temporal resolutions*, *Materials Today Physics* **2** (2017) 46–53.

[18] E. Najafi, T. D. Scarborough, J. Tang, and A. Zewail, *Four-dimensional imaging of carrier interface dynamics in pn junctions*, *Science* **347** (2015), no. 6218 164–167.

[19] B. Liao, E. Najafi, H. Li, A. J. Minnich, and A. H. Zewail, *Photo-excited hot carrier dynamics in hydrogenated amorphous silicon imaged by 4D electron microscopy*, *Nature Nanotechnology* **12** (2017), no. 9 871–876.

[20] B. Liao, H. Zhao, E. Najafi, X. Yan, H. Tian, J. Tice, A. J. Minnich, H. Wang, and A. H. Zewail, *Spatial-temporal imaging of anisotropic photocarrier dynamics in black phosphorus*, *Nano Letters* **17** (2017), no. 6 3675–3680.

[21] S. Ellis, N. Bartelt, F. Léonard, K. Celio, E. Fuller, D. Hughart, D. Garland, M. Marinella, J. Michael, D. Chandler, *et. al.*, *Scanning ultrafast electron microscopy reveals photovoltage dynamics at a deeply buried p-Si/SiO_2 interface*, *Physical Review B* **104** (2021), no. 16 L161303.

[22] E. Najafi, B. Liao, T. Scarborough, and A. Zewail, *Imaging surface acoustic wave dynamics in semiconducting polymers by scanning ultrafast electron microscopy*, *Ultramicroscopy* **184** (2018) 46–50.

[23] T. Kim, S. Oh, U. Choudhry, C. D. Meinhart, M. L. Chabinyc, and B. Liao, *Transient strain-induced electronic structure modulation in a semiconducting polymer imaged by scanning ultrafast electron microscopy*, *Nano Letters* **21** (2021), no. 21 9146–9152.

[24] B. S. Shaheen, A. M. El-Zohry, J. Zhao, J. Yin, M. N. Hedhili, O. M. Bakr, and O. F. Mohammed, *Real-space mapping of surface-oxygen defect states in photovoltaic materials using low-voltage scanning ultrafast electron microscopy*, *ACS Applied Materials & Interfaces* **12** (2020), no. 6 7760–7767.

[25] Y. Li, U. Choudhry, J. Ranasinghe, A. Ackerman, and B. Liao, *Probing surface photovoltage effect using photoassisted secondary electron emission*, *The Journal of Physical Chemistry A* **124** (2020) 5246–5252.

[26] B. Liao and E. Najafi, *Scanning ultrafast electron microscopy: A novel technique to probe photocarrier dynamics with high spatial and temporal resolutions*, *Materials Today Physics* **2** (2017) 46–53.

[27] E. Najafi, V. Ivanov, A. Zewail, and M. Bernardi, *Super-diffusion of excited carriers in semiconductors*, *Nature Communications* **8** (2017) 15177.

[28] B. Liao, Y. Li, and U. Choudhry, *Probing the surface photovoltage effect by imaging photo-assisted secondary electron emission*, *Microscopy and Microanalysis* **26** (2020) 1156–1156.

[29] M. Peplow, *The plastics revolution: how chemists are pushing polymers to new limits*, *Nature* **536** (2016), no. 7616.

[30] G. Yu, J. Gao, J. C. Hummelen, F. Wudl, and A. J. Heeger, *Polymer photovoltaic cells: enhanced efficiencies via a network of internal donor-acceptor heterojunctions*, *Science* **270** (1995), no. 5243 1789–1791.

[31] A. Ferguson, N. Kopidakis, S. Shaheen, and G. Rumbles, *Quenching of excitons by holes in poly(3-hexylthiophene) films*, *J. Phys. Chem. C* **112** (2008), no. 26 59865–59871.

[32] A. Ferguson, N. Kopidakis, S. Shaheen, and G. Rumbles, *Dark carriers, trapping, and activation control of carrier recombination in neat p3ht and p3ht:pcbm blends*, *J. Phys. Chem. C* **115** (2011), no. 46 23134–23148.

[33] S. Cowan, A. Roy, and A. Heeger, *Recombination in polymer-fullerene bulk heterojunction solar cells*, *Phys. Rev. B* **82** (2010), no. 24 245207.

[34] O. Mikhnenko, M. Kuik, J. Lin, N. d. Kaap, T. Nguyen, and P. Blom, *Trap-limited exciton diffusion in organic semiconductors*, *Adv. Mater.* **26** (2014), no. 12 1912–1917.

[35] J. Hodgkiss, S. Albert-Seifried, A. Rao, A. Barker, A. Campbell, R. Marsh, and R. Friend, *Exciton-charge annihilation in organic semiconductor films*, *Adv. Funct. Mater.* **22** (2012), no. 8 1567–1577.

[36] I. Hwang, D. Moses, and A. Heeger, *Photoinduced carrier generation in p3ht/pcbm bulk heterojunction materials*, *J. Phys. Chem. C* **112** (2008), no. 11 4350–4354.

[37] V. Mihailetchi, J. Wildeman, and P. Blom, *Space-charge limited photocurrent*, *Phys. Rev. Lett.* **94** (2005), no. 12 126602.

[38] X. Feng and X. Wang, *Thermophysical properties of free-standing micrometer-thick poly(3-hexylthiophene) films*, *Thin Solid Films* **519** (2011), no. 16 5700–5705.

[39] Y. Xu, X. Wang, J. Zhou, B. Song, Z. Jiang, E. Lee, S. Huberman, K. Gleason, and G. Chen, *Molecular engineered conjugated polymer with high thermal conductivity*, *Sci. Adv.* **4** (2018), no. 3 eaar3031.

[40] M. M. Rojo, J. Martín, S. Grauby, T. Borca-Tasciuc, S. Dilhaire, and M. Martin-Gonzalez, *Correction: Decrease in thermal conductivity in polymeric p3ht nanowires by size-reduction induced by crystal orientation: new approaches towards thermal transport engineering of organic materials*, *Nanoscale* **7** (2015), no. 9 4256–4257.

[41] S. Hiura, N. Okada, J. Wakui, H. Narita, S. Kanehashi, and T. Shimomura, *Thermoelectric properties of poly (3-hexylthiophene) nanofiber mat with a large void fraction*, *Materials* **10** (2017), no. 5 468.

[42] J. Duda, P. Hopkins, Y. Shen, and M. Gupta, *Thermal transport in organic semiconducting polymers*, *Appl. Phys. Lett.* **102** (2013), no. 25 251912.

[43] Z. Guo, D. Lee, Y. Liu, F. Sun, A. Sliwinski, H. Gao, P. C. Burns, L. Huang, and

T. Luo, *Tuning the thermal conductivity of solar cell polymers through side chain engineering*, *Physical Chemistry Chemical Physics* **16** (2014), no. 17 7764–7771.

[44] M. Maldovan, *Sound and heat revolutions in phononics*, *Nature* **503** (2013), no. 7475 209–217.

[45] C. M. Proctor, M. Kuik, and T.-Q. Nguyen, *Charge carrier recombination in organic solar cells*, *Progress in Polymer Science* **38** (2013), no. 12 1941–1960.

[46] M. Jørgensen, K. Norrman, and F. Krebs, *Stability/degradation of polymer solar cells*, *Sol. Energy Mater. Sol. Cells* **92** (2008), no. 7 686–714.

[47] X. Wang, V. Ho, R. Segalman, and D. Cahill, *Thermal conductivity of high-modulus polymer fibers*, *Macromolecules* **46** (2013), no. 12 4937–4943.

[48] A. Weathers, Z. Khan, R. Brooke, D. Evans, M. Pettes, J. Andreasen, X. Crispin, and L. Shi, *Significant electronic thermal transport in the conducting polymer poly(3,4-ethylenedioxythiophene)*, *Adv. Mater.* **27** (2015), no. 12 2101–2106.

[49] Y. Xu, D. Kraemer, B. Song, Z. Jiang, J. Zhou, J. Loomis, J. Wang, M. Li, H. Ghasemi, X. Huang, X. Li, and G. Chen, *Nanostructured polymer films with metal-like thermal conductivity*, *arXiv:1708.06416* (2017).

[50] J. Johnson, A. Maznev, M. Bulsara, E. Fitzgerald, T. Harman, S. Calawa, C. Vineis, G. Turner, and K. Nelson, *Phase-controlled, heterodyne laser-induced transient grating measurements of thermal transport properties in opaque material*, *J. Appl. Phys.* **111** (2012), no. 2 023503.

[51] A. Robbins, S. Drakopoulos, I. Martin-Fabiani, S. Ronca, and A. Minnich, *Ballistic thermal phonons traversing nanocrystalline domains in oriented polyethylene*, *Proc. Natl. Acad. Sci.* **116** (2019), no. 35 17163–17168.

[52] O. Käding, H. Skurk, A. Maznev, and E. Matthias, *Transient thermal gratings at surfaces for thermal characterization of bulk materials and thin films*, *Appl. Phys. A* **61** (1995), no. 3 253–261.

[53] A. Vega-Flick, R. Duncan, J. Eliason, J. Cuffe, J. Johnson, J. Peraud, L. Zeng, Z. Lu, A. Maznev, E. Wang, *et. al.*, *Thermal transport in suspended silicon membranes measured by laser-induced transient gratings*, *AIP Adv.* **6** (2016), no. 12 121903.

[54] A. Vega-Flick, D. Jung, S. Yue, J. Bowers, and B. Liao, *Reduced thermal conductivity of epitaxial gaas on si due to symmetry-breaking biaxial strain*, *Phys. Rev. Mater.* **3** (2019), no. 3 034603.

[55] M. Z. Hasan and C. L. Kane, *Colloquium: topological insulators*, *Reviews of Modern Physics* **82** (2010), no. 4 3045.

[56] B. Lv, T. Qian, and H. Ding, *Experimental perspective on three-dimensional topological semimetals*, *Reviews of Modern Physics* **93** (2021), no. 2 025002.

[57] C. Fu, Y. Sun, and C. Felser, *Topological thermoelectrics*, *APL Materials* **8** (2020), no. 4 040913.

[58] D. Vu, W. Zhang, C. Şahin, M. E. Flatté, N. Trivedi, and J. P. Heremans, *Thermal chiral anomaly in the magnetic-field-induced ideal Weyl phase of $Bi_{1-x}Sb_x$*, *Nat. Mater.* **20** (Nov., 2021) 1525–1531.

[59] T. Schumann, M. Goyal, H. Kim, and S. Stemmer, *Molecular beam epitaxy of Cd_3As_2 on a III-V substrate*, *APL Materials* **4** (Dec., 2016) 126110.

[60] L.-C. Chen, P.-Q. Chen, W.-J. Li, Q. Zhang, V. V. Struzhkin, A. F. Goncharov, Z. Ren, and X.-J. Chen, *Enhancement of thermoelectric performance across the topological phase transition in dense lead selenide*, *Nature Materials* **18** (2019), no. 12 1321–1326.

[61] B. Skinner and L. Fu, *Large, nonsaturating thermopower in a quantizing magnetic field*, *Science Advances* **4** (2018), no. 5 eaat2621.

[62] F. Han, N. Andrejevic, T. Nguyen, V. Kozii, Q. T. Nguyen, T. Hogan, Z. Ding, R. Pablo-Pedro, S. Parjan, B. Skinner, *et. al.*, *Quantized thermoelectric Hall effect induces giant power factor in a topological semimetal*, *Nature Communications* **11** (2020), no. 1 6167.

[63] W. Zhang, P. Wang, B. Skinner, R. Bi, V. Kozii, C.-W. Cho, R. Zhong, J. Schneeloch, D. Yu, G. Gu, *et. al.*, *Observation of a thermoelectric Hall plateau in the extreme quantum limit*, *Nature Communications* **11** (2020), no. 1 1046.

[64] S. Yue, H. T. Chorsi, M. Goyal, T. Schumann, R. Yang, T. Xu, B. Deng, S. Stemmer, J. A. Schuller, and B. Liao, *Soft phonons and ultralow lattice thermal conductivity in the Dirac semimetal Cd_3As_2*, *Phys. Rev. Research* **1** (Nov., 2019) 033101.

[65] S. Yue, B. Deng, Y. Liu, Y. Quan, R. Yang, and B. Liao, *Phonon softening near topological phase transitions*, *Physical Review B* **102** (2020), no. 23 235428.

[66] T. Nguyen, F. Han, N. Andrejevic, R. Pablo-Pedro, A. Apte, Y. Tsurimaki, Z. Ding, K. Zhang, A. Alatas, E. E. Alp, *et. al.*, *Topological singularity induced*

chiral Kohn anomaly in a Weyl semimetal, *Physical Review Letters* **124** (2020), no. 23 236401.

[67] D. C. Joy, *Monte Carlo modeling for electron microscopy and microanalysis*. Oxford University Press, 1995.

[68] P. Hovington, D. Drouin, and R. Gauvin, *CASINO: A new Monte Carlo code in C language for electron beam interaction — part I: Description of the program*, *Scanning* **19** (1997) 1–14.

[69] J.-C. Kuhr and H.-J. Fitting, *Monte Carlo simulation of electron emission from solids*, *Journal of Electron Spectroscopy and Related Phenomena* **105** (1999) 257–273.

[70] T. D. Ly, D. G. Howitt, M. K. Farrens, and A. B. Harker, *Monte Carlo calculations for specimens with microstructures*, *Scanning* **17** (1995) 220–226.

[71] Z. J. Ding and H. M. Li, *Application of Monte Carlo simulation to SEM image contrast of complex structures*, *Surface and Interface Analysis* **37** (2005) 912–918.

[72] Z.-J. Ding and R. Shimizu, *A Monte Carlo modeling of electron interaction with solids including cascade secondary electron production*, *Scanning* **18** (1996) 92–113.

[73] M. Azzolini, T. Morresi, G. Garberoglio, L. Calliari, N. M. Pugno, S. Taioli, and M. Dapor, *Monte Carlo simulations of measured electron energy-loss spectra of diamond and graphite: Role of dielectric-response models*, *Carbon* **118** (2017) 299–309.

[74] A. Jablonski, F. Salvat, and C. J. Powell, *Comparison of electron elastic-scattering cross sections calculated from two commonly used atomic potentials*, *Journal of physical and chemical reference data* **33** (2004), no. 2 409–451.

[75] Z. Czyżewski, D. O. MacCallum, A. Romig, and D. C. Joy, *Calculations of mott scattering cross section*, *Journal of Applied Physics* **68** (1990), no. 7 3066–3072.

[76] D. Pines, *Elementary excitations in solids: lectures on phonons, electrons, and plasmons*. W.A. Benjamin, 1964.

[77] D. Pines and P. Nozières, *The Theory of Quantum Liquids: Normal Fermi Liquids*. Benjamin, 1966.

[78] L. Devroye, *Nonuniform random variate generation*, *Handbooks in Operations Research and Management Science* **13** (2006) 83–121.

[79] T. S. Rao-Sahib and D. B. Wittry, *X-ray continuum from thick elemental targets for 10–50-keV electrons*, *Journal of Applied Physics* **45** (1974) 5060–5068.

[80] J. Ashley, *Energy loss rate and inelastic mean free path of low-energy electrons and positrons in condensed matter*, *Journal of Electron Spectroscopy and Related Phenomena* **50** (1990) 323–334.

[81] C. Ullrich, *Time-dependent density-functional theory: concepts and applications*. Oxford University Press, 2012.

[82] H.-C. Weissker, J. Serrano, S. Huotari, F. Bruneval, F. Sottile, G. Monaco, M. Krisch, V. Olevano, and L. Reining, *Signatures of short-range many-body effects in the dielectric function of silicon for finite momentum transfer*, *Physical Review Letters* **97** (2006), no. 23 237602.

[83] S. Sato, Y. Shinohara, T. Otobe, and K. Yabana, *Dielectric response of laser-excited silicon at finite electron temperature*, *Physical Review B* **90** (2014), no. 17 174303.

[84] S. Sharma, J. K. Dewhurst, A. Sanna, and E. K. U. Gross, *Bootstrap approximation for the exchange-correlation kernel of time-dependent density-functional theory*, *Physical Review Letters* **107** (2011) 186401.

[85] "The Elk Code." http://elk.sourceforge.net/.

[86] E. D. Palik, *Handbook of optical constants of solids*, vol. 3. Academic press, 1998.

[87] Y. Sun, H. Xu, B. Da, S.-f. Mao, and Z.-j. Ding, *Calculations of energy-loss function for 26 materials*, *Chinese Journal of Chemical Physics* **29** (2016) 663–670.

[88] S. Tanuma, C. J. Powell, and D. R. Penn, *Use of sum rules on the energy-loss function for the evaluation of experimental optical data*, *Journal of Electron Spectroscopy and Related Phenomena* **62** (1993), no. 1-2 95–109.

[89] D. C. Joy, *A database on electron-solid interactions*, *Scanning* **17** (1995), no. 5 270–275.

[90] G. Goodno, G. Dadusc, and R. Miller, *Ultrafast heterodyne-detected transient-grating spectroscopy using diffractive optics*, *J. Opt. Soc. Am. B* **15** (1998), no. 6 1791–1794.

[91] C. Dennett and M. Short, *Thermal diffusivity determination using heterodyne*

phase-insensitive transient grating spectroscopy, *J. Appl. Phys.* **123** (2018), no. 21 215109.

[92] T. Kim, S. X. Drakopoulos, S. Ronca, and A. J. Minnich, *Origin of high thermal conductivity in disentangled ultra-high molecular weight polyethylene films: ballistic phonons within enlarged crystals*, *Nature Communications* **13** (2022), no. 1 2452.

[93] D. R. Baker and J. P. Heremans, *Linear geometrical magnetoresistance effect: Influence of geometry and material composition*, *Physical Review B* **59** (1999), no. 21 13927.

[94] J. Cho, T. Y. Hwang, and A. H. Zewail, *Visualization of carrier dynamics in p(n)-type GaAs by scanning ultrafast electron microscopy*, *Proceedings of the National Academy of Sciences* **111** (2014), no. 6 2094–2099.

[95] D. D. Perovic, M. R. Castell, A. Howie, C. Lavoie, T. Tiedje, and J. S. W. Cole, *Field-emission sem imaging of compositional and doping layer semiconductor superlattices*, *Ultramicroscopy* **58** (1995) 104–113.

[96] T. Sjodin, H. Petek, and H.-L. Dai, *Ultrafast carrier dynamics in silicon: A two-color transient reflection grating study on a (111) surface*, *Physical Review Letters* **81** (1998), no. 25 5664.

[97] Z. Zhang, J. Martis, X. Xu, H.-K. Li, C. Xie, B. Takasuka, J. Lee, A. K. Roy, and A. Majumdar, *Photoabsorption imaging at nanometer scales using secondary electron analysis*, *Nano Letters* **21** (2021), no. 5 1935–1942.

[98] S. J. Gitomer, R. D. Jones, F. Begay, A. W. Ehler, J. F. Kephart, and R. Kristal, *Fast ions and hot electrons in the laser–plasma interaction*, *The Physics of Fluids* **29** (1986) 2679–2688.

[99] A. M. El-Zohry, B. S. Shaheen, V. M. Burlakov, J. Yin, M. N. Hedhili, S. Shikin, B. Ooi, O. M. Bakr, and O. F. Mohammed, *Extraordinary carrier diffusion on CdTe surfaces uncovered by 4D electron microscopy*, *Chem* **5** (2019), no. 3 706–718.

[100] U. Choudhry, F. Pan, X. He, B. Shaheen, T. Kim, R. Gnabasik, G. A. Gamage, H. Sun, A. Ackerman, D.-S. Yang, *et. al.*, *Persistent hot carrier diffusion in boron arsenide single crystals imaged by ultrafast electron microscopy*, *Matter* **6** (2023) 206–216.

[101] Z. Zhang and J. T. Yates, *Band bending in semiconductors: Chemical and physical consequences at surfaces and interfaces*, *Chemical Reviews* **112** (2012) 5520–5551.

[102] H. Wang, H. Wang, B. Gao, L. Wang, Z. Yang, X. Du, Q. Chen, J. Song, and H. Sun, *Exciton diffusion and charge transfer dynamics in nano phase-separated p3ht/pcbm blend films*, *Nanoscale* **3** (2011), no. 5 2280–2285.

[103] F. Mahmood, Z. Alpichshev, Y.-H. Lee, J. Kong, and N. Gedik, *Observation of exciton–exciton interaction mediated valley depolarization in monolayer mose2*, *Nano Lett.* **18** (2018), no. 1 223–228.

[104] T. Kim, D. Ding, J.-H. Yim, Y.-D. Jho, and A. Minnich, *Elastic and thermal properties of free-standing molybdenum disulfide membranes measured using ultrafast transient grating spectroscopy*, *APL Mater.* **5** (2017), no. 8 086105.

[105] J. Johnson, A. Maznev, J. Cuffe, J. Eliason, A. Minnich, T. Kehoe, C. Torres, G. Chen, and K. Nelson, *Direct measurement of room-temperature nondiffusive thermal transport over micron distances in a silicon membrane*, *Phys. Rev. Lett.* **110** (2013), no. 2 025901.

[106] X. Xie, D. Li, T.-H. Tsai, J. Liu, P. Braun, and D. Cahill, *Thermal conductivity, heat capacity, and elastic constants of water-soluble polymers and polymer blends*, *Macromolecules* **49** (2016), no. 3 972–978.

[107] F. Bencivenga, R. Mincigrucci, F. Capotondi, L. Foglia, D. Naumenko, A. Maznev, E. Pedersoli, A. Simoncig, F. Caporaletti, V. Chiloyan, *et. al.*, *Nanoscale transient gratings excited and probed by extreme ultraviolet femtosecond pulses*, *Sci. Adv.* **5** (2019), no. 7 eaaw5805.

[108] J. Vollbrecht, V. Brus, S.-J. Ko, J. Lee, A. Karki, D. Cao, K. Cho, G. Bazan, and T.-Q. Nguyen, *Quantifying the nongeminate recombination dynamics in nonfullerene bulk heterojunction organic solar cells*, *Adv. Energy Mater.* **9** (2019), no. 32 1901438.

[109] J. Piris, T. Dykstra, A. Bakulin, P. Loosdrecht, W. Knulst, M. Trinh, J. Schins, and L. Siebbeles, *Photogeneration and ultrafast dynamics of excitons and charges in p3ht/pcbm blends*, *J. Phys. Chem. C* **113** (2009), no. 32 14500–14506.

[110] C.-X. Sheng, M. Tong, S. Singh, and Z. Vardeny, *Experimental determination of the charge/neutral branching ratio g in the photoexcitation of p-conjugated polymers by broadband ultrafast spectroscopy*, *Phys. Rev. B* **75** (2007), no. 8 085206.

[111] V. Brus, C. Proctor, N. Ran, and T.-Q. Nguyen, *Capacitance spectroscopy for quantifying recombination losses in nonfullerene small-molecule bulk heterojunction solar cells*, *Adv. Energy Mater.* **6** (2016), no. 11 1502250.

[112] C.-K. Lee, C.-W. Pao, and C.-W. Chu, *Multiscale molecular simulations of the nanoscale morphologies of p3ht:pcbm blends for bulk heterojunction organic photovoltaic cells*, *Energy Environ. Sci.* **4** (2011), no. 10 4124–4132.

[113] Y. Liang, Z. Xu, J. Xia, S.-T. Tsai, Y. Wu, G. Li, C. Ray, and L. Yu, *For the bright future—bulk heterojunction polymer solar cells with power conversion efficiency of 7.4E135–E138.*

[114] S. Park, A. Roy, S. Beaupré, S. Cho, N. Coates, J. Moon, D. Moses, M. Leclerc, K. Lee, and A. Heeger, Bulk heterojunction solar cells with internal quantum efficiency approaching 100(2009), no. 5 297–302.

[115] B. Yurash, H. Nakanotani, Y. Olivier, D. Beljonne, C. Adachi, and T.-Q. Nguyen, Photoluminescence quenching probes spin conversion and exciton dynamics in thermally activated delayed fluorescence materials, Adv. Mater. **31** *(2019), no. 21 1804490.*

[116] D. Murthy, A. Melianas, Z. Tang, G. Juška, K. Arlauskas, F. Zhang, L. Siebbeles, O. Inganäs, and T. Savenije, Origin of reduced bimolecular recombination in blends of conjugated polymers and fullerenes, Adv. Funct. Mater. **23** *(2013), no. 34 4262–4268.*

[117] T. Clarke, F. Jamieson, and J. Durrant, Transient absorption studies of bimolecular recombination dynamics in polythiophene/fullerene blend films, J. Phys. Chem. C **113** *(2009), no. 49 20934–20941.*

[118] V. Coropceanu, X.-K. Chen, T. Wang, Z. Zheng, and J.-L. Brédas, Charge-transfer electronic states in organic solar cells, Nat. Rev. Mater. **4** *(2019), no. 11 689–707.*

[119] G. D'Avino, L. Muccioli, Y. Olivier, and D. Beljonne, Charge separation and recombination at polymer–fullerene heterojunctions: Delocalization and hybridization effects, J. Phys. Chem. Lett. **7** *(2016), no. 3 536–540.*

[120] I. Crassee, R. Sankar, W.-L. Lee, A. Akrap, and M. Orlita, 3D Dirac semimetal Cd_3As_2: A review of material properties, Phys. Rev. Materials **2** *(Dec., 2018) 120302.*

[121] Z. Wang, H. Weng, Q. Wu, X. Dai, and Z. Fang, Three-dimensional Dirac semimetal and quantum transport in Cd_3As_2, Phys. Rev. B **88** *(Sept., 2013) 125427.*

[122] B.-J. Yang and N. Nagaosa, Classification of stable three-dimensional Dirac

semimetals with nontrivial topology, Nature Communications **5** *(Sept., 2014) 4898.*

[123] H. T. Chorsi, S. Yue, P. P. Iyer, M. Goyal, T. Schumann, S. Stemmer, B. Liao, and J. A. Schuller, Widely tunable optical and thermal properties of Dirac semimetal Cd_3As_2, Advanced Optical Materials **8** *(2020), no. 8 1901192.*

[124] D. P. Spitzer, G. A. Castellion, and G. Haacke, Anomalous thermal conductivity of Cd_3As_2 and the Cd_3As_2-Zn_3As_2 alloys, Journal of Applied Physics **37** *(Sept., 1966) 3795–3801.*

[125] D. Armitage and H. J. Goldsmid, The thermal conductivity of cadmium arsenide, Journal of Physics C: Solid State Physics **2** *(Nov., 1969) 2138–2145.*

[126] H. Wang, X. Luo, W. Chen, N. Wang, B. Lei, F. Meng, C. Shang, L. Ma, T. Wu, X. Dai, Z. Wang, and X. Chen, Magnetic-field enhanced high-thermoelectric performance in topological Dirac semimetal Cd_3As_2 crystal, Science Bulletin **63** *(Apr., 2018) 411–418.*

[127] A. Pariari, N. Khan, R. Singha, B. Satpati, and P. Mandal, Tuning the scattering mechanism in the three-dimensional Dirac semimetal Cd_3As_2, Phys. Rev. B **94** *(Oct., 2016) 165139.*

[128] Z. Jia, C. Li, X. Li, J. Shi, Z. Liao, D. Yu, and X. Wu, Thermoelectric signature of the chiral anomaly in Cd_3As_2, Nat Commun **7** *(Oct., 2016) 13013.*

[129] R. Amarnath, K. S. Bhargavi, and S. S. Kubakaddi, Thermoelectric transport properties in 3D Dirac semimetal Cd_3As_2, J. Phys.: Condens. Matter **32** *(May, 2020) 225704.*

[130] T. Liang, J. Lin, Q. Gibson, T. Gao, M. Hirschberger, M. Liu, R. J. Cava, and N. P. Ong, Anomalous Nernst effect in the Dirac semimetal Cd_3As_2, Phys. Rev. Lett. **118** *(Mar., 2017) 136601.*

[131] S. M. Young, S. Zaheer, J. C. Y. Teo, C. L. Kane, E. J. Mele, and A. M. Rappe, Dirac semimetal in three dimensions, Physical Review Letters **108** *(Apr., 2012) 140405.*

[132] H. Pan, M. Wu, Y. Liu, and S. A. Yang, Electric control of topological phase transitions in Dirac semimetal thin films, Scientific Reports **5** *(Sept., 2015) 14639.*

[133] X. Xiao, S. A. Yang, Z. Liu, H. Li, and G. Zhou, Anisotropic quantum

confinement effect and electric control of surface states in dirac semimetal nanostructures, Scientific Reports **5** *(Jan., 2015) 7898.*

[134] A. Narayan, D. Di Sante, S. Picozzi, and S. Sanvito, Topological tuning in three-dimensional Dirac semimetals, Physical Review Letters **113** *(Dec., 2014) 256403.*

[135] T. Schumann, L. Galletti, D. A. Kealhofer, H. Kim, M. Goyal, and S. Stemmer, Observation of the quantum Hall effect in confined films of the three-dimensional Dirac semimetal Cd_3As_2, Phys. Rev. Lett. **120** *(Jan., 2018) 016801.*

[136] M. Goyal, L. Galletti, S. Salmani-Rezaie, T. Schumann, D. A. Kealhofer, and S. Stemmer, Thickness dependence of the quantum Hall effect in films of the three-dimensional Dirac semimetal Cd_3As_2, APL Materials **6** *(Feb., 2018) 026105.*

[137] P. V. Arribi, J.-X. Zhu, T. Schumann, S. Stemmer, A. A. Burkov, and O. Heinonen, Topological surface states in strained Dirac semimetal thin films, Physical Review B **102** *(2020), no. 15 155141.*

[138] A. C. Potter, I. Kimchi, and A. Vishwanath, Quantum oscillations from surface Fermi arcs in Weyl and Dirac semimetals, Nature Communications **5** *(Oct., 2014) 5161.*

[139] C. M. Wang, H.-P. Sun, H.-Z. Lu, and X. C. Xie, 3D quantum Hall effect of fermi arcs in topological semimetals, Physical Review Letters **119** *(Sept., 2017) 136806.*

[140] L. Galletti, T. Schumann, O. F. Shoron, M. Goyal, D. A. Kealhofer, H. Kim, and S. Stemmer, Two-dimensional Dirac fermions in thin films of Cd_3As_2, Physical Review B **97** *(2018), no. 11 115132.*

[141] L. Galletti, T. Schumann, T. E. Mates, and S. Stemmer, Nitrogen surface passivation of the Dirac semimetal Cd_3As_2, Phys. Rev. Materials **2** *(Dec., 2018) 124202.*

[142] L.-P. He and S.-Y. Li, Quantum transport properties of the three-dimensional Dirac semimetal Cd_3As_2 single crystals, Chinese Phys. B **25** *(Nov., 2016) 117105.*

[143] Z. J. Xiang, D. Zhao, Z. Jin, C. Shang, L. K. Ma, G. J. Ye, B. Lei, T. Wu, Z. C. Xia, and X. H. Chen, Angular-dependent phase factor of Shubnikov–de Haas oscillations in the Dirac semimetal Cd_3As_2, Physical Review Letters **115** *(Nov., 2015) 226401.*

[144] M. Goyal, H. Kim, T. Schumann, L. Galletti, A. A. Burkov, and S. Stemmer,

Surface states of strained thin films of the Dirac semimetal Cd_3As_2, Phys. Rev. Materials **3** *(June, 2019) 064204.*

[145] K. Eto, Z. Ren, A. A. Taskin, K. Segawa, and Y. Ando, Angular-dependent oscillations of the magnetoresistance in Bi_2Se_3 due to the three-dimensional bulk Fermi surface, Physical Review B **81** *(May, 2010) 195309.*

[146] N. W. Ashcroft and D. N. Mermin, Solid State Physics. *Cengage Learning, New York, 1976.*

[147] Y. Ando, Topological insulator materials, J. Phys. Soc. Japan **82** *(2013), no. 10 102001.*

[148] T. Liang, Q. Gibson, J. Xiong, M. Hirschberger, S. P. Koduvayur, R. Cava, and N. Ong, Evidence for massive bulk Dirac fermions in $Pb_{1-x}Sn_xSe$ from Nernst and thermopower experiments, Nature Communications **4** *(Nov., 2013) 2696.*

[149] D. Chen, B. He, M. Yao, Y. Pan, H. Lin, W. Schnelle, Y. Sun, J. Gooth, L. Taillefer, and C. Felser, Anomalous thermoelectric effects and quantum oscillations in the kagome metal CsV_3Sb_5, Physical Review B **105** *(2022), no. 20 L201109.*

[150] P. Hosur and X. Qi, Recent developments in transport phenomena in Weyl semimetals, Comptes Rendus Physique **14** *(2013), no. 9-10 857–870.*

[151] A. C. Lygo, B. Guo, A. Rashidi, V. Huang, P. Cuadros-Romero, and S. Stemmer, Two-dimensional topological insulator state in cadmium arsenide thin films, Physical Review Letters **130** *(2023), no. 4 046201.*

[152] G. Kresse and J. Furthmüller, Efficient iterative schemes for ab initio total-energy calculations using a plane-wave basis set, Phys. Rev. B **54** *(1996), no. 16 11169.*

[153] G. Kresse and J. Furthmüller, Efficiency of ab-initio total energy calculations for metals and semiconductors using a plane-wave basis set, Comput. Mater. Sci. **6** *(July, 1996) 15–50.*

[154] P. E. Blöchl, Projector augmented-wave method, Phys. Rev. B **50** *(1994), no. 24 17953–17979.*

[155] J. P. Perdew, K. Burke, and M. Ernzerhof, Generalized gradient approximation made simple, Phys. Rev. Lett. **77** *(1996), no. 18 3865–3868.*

[156] M. N. Ali, Q. Gibson, S. Jeon, B. B. Zhou, A. Yazdani, and R. J. Cava, The

crystal and electronic structures of Cd_3As_2, the three-dimensional electronic analogue of graphene, Inorg. Chem. **53** *(2014), no. 8 4062–4067.*

[157] A. M. Conte, O. Pulci, and F. Bechstedt, Electronic and optical properties of topological semimetal Cd3 As2, Sci. Rep. **7** *(2017) 1–13.*

[158] S. Baidya and D. Vanderbilt, First-principles theory of the Dirac semimetal Cd_3As_2 under Zeeman magnetic field, Phys. Rev. B **102** *(2020), no. 16 1–8, [arXiv:2008.1070].*

[159] P. M. Rourke and S. R. Julian, Numerical extraction of de Haas-van Alphen frequencies from calculated band energies, Comput. Phys. Commun. **183** *(2012), no. 2 324–332, [arXiv:0803.1895].*

[160] G. K. Madsen and D. J. Singh, BoltzTraP. A code for calculating band-structure dependent quantities, Comput. Phys. Commun. **175** *(2006), no. 1 67–71, [0602203].*

[161] G. K. Madsen, J. Carrete, and M. J. Verstraete, BoltzTraP2, a program for interpolating band structures and calculating semi-classical transport coefficients, Comput. Phys. Commun. **231** *(2018) 140–145, [arXiv:1712.0794].*